Ministry of Higher Education and Scientific Research
Hassiba Ben Bouali University Chlef
Faculty of Exact Sciences and Informatics
Department of Chemistry

THESIS

Presented for obtaining a diploma of

DOCTORAT

Field : Chemistry

Specialty: Security, Reliability and Enhancement Of Gas Pipelines

By

BELKACEM AMINE KESSAL

Theme:

Damage to Metallic Materials- Study project on techniques and early detection of SCC in stainless steels Type 304L Control of initiation and propagation of SCC cracks

Supported , before a jury composed of:

Mustapha Douani	Professor	UHB-Chlef	President
Larbi Hemmouche	MCA	EMP	Examiner
Razika Mehdaoui	MCA	University of Blida	Examiner
Ikhlef Laidani	MCA	University of Mascara	Examiner
Mohammed Hadj Meliani	Professor	UHB-Chlef	Examiner
M'hamed Djennad	Professor	University of Mostaganem	Invited
Chahinez FARES	Professor	UHB-Chlef	Supervisor

Thanks

I dedicate this modest work

To

"all those who believe the beauty of their dreams"

First and foremost, I would like to express my gratitude and deep appreciation to my family who have always supported and encouraged me during my schooling and graduation from university studies. It is a pleasant duty for me to dedicate this thesis to my dear parents especially to my mother whom I respect infinitely. May they find here the expression of my deep gratitude for their understanding and patience throughout my academic journey, including the development of my thesis work.

I would like to express my gratitude and my thanks to Miss Fares Chahinez, Professor in the Faculty of Technology at UHB-Chlef, who placed her trust in me by agreeing to supervise my thesis by giving me her time and valuable advice. Her kindness, her scientific rigor as well as her knowledge in the field of Corrosion were of great importance in the success of this thesis.

I address my warmest thanks to Mr. Mohammed Hadj Meliani, Professor at the Faculty of Technology at UHB-Chlef and Director of Theoretical Physics and Materials Physics Laboratory (LPTPM) for accepting the task of appraising my thesis work.

This work was carried out in the laboratory Theoretical Physics and Materials Physics (LPTPM)/Chlef and Scientific and Technical Research Center in Physico-Chemical Analysis (CRAPC)/ Bousmail; Tipaza.

I would like to thank Mr. Mustapha Douani, Professor at the Faculty of Technology at UHB-Chlef who accepted to chair the jury of this thesis. I would like to thank the members of the jury for having examined and commented with great interest on my thesis.

I would like to thank Mr. BeLkhalfa Hakim, Researcher at CRAPC for his help in carrying out Electrochemical and impedancemetry analyzes at the CRAPC Laboratory

I would like to thank Madam Fellouh, Metallurgical Engineer at the Mechanical Testing Laboratory at ENGTP Arzew, as well as all these colleagues from the department, for the excellent welcome they have given me as well as their invaluable help in the supply of smallpox.

pipes and all the technical documentation I needed regarding the welding process used. May they find here the expression of my great gratitude.

I would also like to thank Mr. Chafaa Meziane, welder approved by ENGTP / Z, for his availability and his advice on the welding of stainless steels.

I would like to express my gratitude and thanks to everyone who supported the completion of my thesis.

ملخص :

تقترح هذه الرسالة إنشاء دراسة تجريبية بين البنية الدقيقة والسلوك الكهروكيميائي والميكانيكي للمفاصل الملحومة في الفولاذ الأوستنيتي المقاوم للصدأ AISI304L وكذلك الكشف المبكر عن SCC والتحكم في بدء وانتشار شقوق SCC.

تهدف إلى تحديد معاملات اللحام للفولاذ 304 ل بواسطة القوس الكهربائي (TIG) على تآكل الوصلات الملحومة على وجه الخصوص في HAZ. للقيام بذلك ، تم أخذ عينات ملحومة بمعايير مختلفة أجريت على أساسها اختبارات ميكانيكية وكهروكيميائية لإثبات سلوك هذه المنطقة في بيئة تآكل مماثلة لمياه البحر (30 غ / لتر).

باستخدام تصميم تجريبي يعتمد على طريقة FED ، قمنا بتقدير مساهمة العوامل التجريبية (معلمات اللحام): (عدد التمريرات ومعدل تدفق غاز الأرجون وتيار اللحام) وكذلك البنية الدقيقة من خلال الوصلة الملحومة على سلوك التآكل. تظهر الدراسة المقارنة بين وصلات اللحام بفضل مقاومتها للتآكل مقاومة أفضل للتآكل الناتج عن الإجهاد لـ AISI 304L.

الكلمات المفتاحية: الفولاذ المقاوم للصدأ ، اللحام ، البنية المجهرية ، التآكل ، الاختبار الميكانيكي ، CSC

Résumé :

La présente thèse propose d'établir une étude empirique entre la microstructure et le comportement électrochimique , mécanique des joints soudés en aciers inoxydables austénitique AISI304L ainsi la détection précoce des CSC et le contrôle de l'amorçage et de la propagation des fissures de CSC.

Ce travail s'inscrit dans la continuité des recherches menées dans le domaine de l'amélioration de la résistance des pipelines à la corrosion. Il a pour but d'identifier les paramètres de soudure de l'acier 304l par arc électrique (TIG) sur la corrosion des joints soudés en particulier dans la ZAT. Pour ce faire, on a pris des échantillons soudés avec différents paramètres sur lesquels on a effectué des tests Mécaniques et électrochimiques pour mettre en évidence le comportement de cette zone dans un milieu corrosif assimilé à l'eau de mer (30 g/l).

En utilisant un plan d'expérience basée sur la méthode FED, nous avons estimé la contribution des facteurs expérimentaux (paramètres de soudage):(Nombre de pass, débit de gaz argon et le courant de soudage) ainsi que la microstructure à travers le joint soudé sur le comportement de corrosion. L'étude comparative entre les joints de soudage de par leur résistance à la corrosion montrent une meilleure résistance à la corrosion sous contrainte du AISI 304L .

Mots clés : Acier inoxydable, soudage, microstructure, corrosion, essais mécaniques, CSC.

Abstract :

This thesis proposes to establish an empirical study between the microstructure and the electrochemical and mechanical behavior of welded joints in austenitic stainless steels AISI304L

as well as the early detection of SCCs and the control of the initiation and propagation of SCC cracks.

This work is a continuation of research carried out in the field of improving the resistance of pipelines to corrosion. It aims to identify the welding parameters of 304l steel by electric arc (TIG) on the corrosion of welded joints in particular in the HAZ. To do this, welded samples were taken with different parameters on which mechanical and electrochemical tests were carried out to demonstrate the behavior of this zone in a corrosive environment similar to seawater (30 g / l).

Using an experimental design based on the FED method, we estimated the contribution of the experimental factors (welding parameters) :(Number of passes, argon gas flow rate and the welding current) as well as the microstructure through the welded joint on corrosion behavior. The comparative study between welding joints due to their corrosion resistance shows better resistance to stress corrosion of AISI 304L.

Keywords: Stainless steel, welding, microstructure, corrosion, mechanical testing, CSC.

Symbol list

α	Ferritic phase
γ	Austenitic phase
Ø	External diameter of the pipe
b_a	Tafel slope of the anode branch
b_c	Tafel slope of the cathode branch
δ	High temperature ferritic phase
E_{corr}	Corrosion potential
E_p	Potential of passivity
E_{tp}	Potential of transpassivity
I_{corr}	Corrosion current intensity
i_{corr}	Corrosion current density
MPa	Mega Pascal
R_p	Polarization resistance
C	Welding current
A	Number of pass
B	Gas Argon Flow Rate

Abbreviation list

API	American Petroleum Institute
AISI	American Iron and Steel Institute
ASME	American Society of Mechanical Engineers
ASTM	American Society for Testing and Materials
ENGTP	National Company of Major Petroleum Works
SCC	Stress Corrosion

SS	Stainless Steel
EDS	Electronic Data Systems
GTAW	Gas tungsten arc welding
HV	Hardness Vickers
L	Low carbon grades
BM	Base Metal
SEM	Scanning Electron Microscopy
MO	Optical Microscope
SONATRACH	National Society for Research, Production, Transport, Transformation, and Marketing of Hydrocarbons
HAZ	Heat Affected Zone
FZ	Fusion Zone
EIS	Electrochemical Impedance Spectroscopy
C_{pe}	Equivalent Potential Circuit
XRD	X-ray diffraction
FED	Factorial Experimental Design
GB	Grain Boundary
PT	Penetrant
IGSCC	Intergranular stress corrosion
AD	Anodic Dissolution

List of figures

Chapter 1

Chapter 2

Chapter 3

Chapter 4

List of tables

Chapter 1

Chapter 2

Chapter 3

Chapter 4

TABLE OF CONTENTS

General Introduction

Due to a beneficial combination of properties, Stainless steels, considering their physical, mechanical and metallurgical characteristics, etc.., are used in countless fields: daily, industry, nuclear, petroleum, mechanics, hydraulics, food processing, chemicals, transport, medicine and surgery, etc…, good corrosion resistance [1-3] as well as good mechanical properties over a wide temperature range. They have a high hardening capacity and high ductility. However, some failures were observed, often due to extreme service conditions. Among the causes of these failures, we cite a high local concentration of thermal stresses, unexpected microstructure defects (presence of weakening phases) as well as very aggressive working environments causing perforating corrosion.

Metal construction manufacturers are increasingly interested in the characterization of the various heterogeneities included in structures and linked in part to assembly operations, such as welding. This type of bond is particularly revealed to be a zone of heterogeneity, both from a microstructural and mechanical point of view.

The pipe part of a pipeline is a mechanically welded construction. In these welded zones (or welded joints, precisely in the thermally affected zone), a form of localized corrosion manifests itself, making it more fragile, thus promoting the rupture of the pipeline. Stress corrosion (SCC) [4, 6] is a mode of damage that leads to the brittle fracture of usually ductile materials under the joint action of the environment and mechanical stress. The interaction between these three parameters (material, environment, stress) is responsible for SCC cracking: neither the exposure medium nor the level of stress applied can alone generate the ruin of the component or the specimen.

The objectives of our study are multiple:

– Determine the influence of GTAW [7, 9] welding operating parameters influencing corrosion on the electrochemical behavior of the heat affected zone (HAZ) in a 30 g / l NaCl solution using the potentiodynamic method and optical microscopy.

– Analyse the electrochemical behavior of the different microstructural zones of the welded joint in AISI 304L and quantitatively elucidate the effect of the variants linked to the environment.

– Highlight the role of the microstructure in the electrochemical behavior of single-phase AISI 304L steel.

- Propose an inspection plan for a stainless steel weld, carried out on a pipeline, Exposed to the risk of corrosion in a neutral chloride environment.

- To carry out a state of knowledge and of the means of non-destructive testing at the different stages of degradation with their advantages / disadvantages and limits. We will focus more particularly on NDT [10] techniques capable of detecting damage in their initiation phase and determining the current mechanical characteristics.

-To carry out a state of knowledge relating to the various types of damage and their mechanism of development and exploitable methodologies to determine the residual life according to material (stainless steel type 18/8 "ASME SA240" Type 304 / 304L).

Here are the approaches we have adopted:

- Metallurgical characterization of the studied samples.

- Study of the corrosion mechanism by potentiodynamic tests as well as by electrochemical impedance (EIS) of AISI 304L samples.

- Study of the evolution of the behavior of the passive film during the passivation process of AISI 304L steel.

- Study of the effects of welding process parameters on stress corrosion in the heat affected zone (HAZ).

In order to disseminate all these points in a clear and structured way, we followed the following drafting plan:

The bibliographical study which constitutes the first chapter, explaining some elements of metallurgy which allow us to understand the constitution of the microstructure of a stainless steel and its evolution during welding. Then, we will discuss the phenomenology of stress corrosion of welded stainless steels and the types of stresses that are called the phenomenon. We present the welding process [11-12] for stainless steels and the Ideal Conditions required

for a weld as well as the Classification of the main welding processes. Finally, we study welding parameters and their effects on electrochemical behavior and mechanical properties.

The second chapter, which adopts the experimental techniques protocol, which is detailed from the collection of our samples of the welded joints. In this chapter, we will observe the microstructural [13-15] state of the base metal and we will characterize the microstructural areas affected by welding. The metallurgical characterization in terms of optical microscopy and SEM aims to establish a relationship between the corrosion mechanisms and the microstructure in different areas of a welded joint. Electrochemical characterization includes polarization, electrochemical impedance spectroscopy as well Mechanical characterization includes (XRD), Micro Dura- meter in addition NDT techniques.

In **the Third chapter** which presents The effect of welding parameters on the mechanical properties [16-18]: hardness and residual stress, describes the planning of the experiments according to a full factorial design of 08 experiments and presents the experimental strategy followed to study the electrochemical behavior of the HAZ (The Response).

The Fourth chapter is devoted to the effect of the welding parameters on corrosion, we will report the results of the microstructural characterization, of all the electrochemical tests carried out on the samples of our study as well as the quality of the weld by use. NDT technique: Radiography, ferritscope. The discussion of these results focuses on understanding the evolution of the electrochemical behavior [19-20] of the different microstructural zones of austenitic steel AISI 304L

Finally, a **general conclusion** summarizes the main results of this study; we propose optimal welding parameters for the in-service inspection of welded stainless steel joint resists corrosion.

Chapter 1

Bibliographic Study

This first chapter is a state of the art relating to stainless steels intended for welding and the corrosion phenomenon that they can undergo. The bibliographic study revolves around three axes; the first is an update on the types of stresses and their effects on the corrosion of stainless steels [21-23]. Then, the second axis reviews the welding processes of stainless steels and the process used in our project. In the third axis; we describe the phase transformations that can take place under the effect of welding parameters on corrosion.

I.1.Stainless steels

Stainless steels commonly referred to as stainless steel, play a large role in countless areas: daily life, mechanical industry, food processing, chemicals, transport, medicine, surgery, etc. These are steels, alloys of iron and carbon, to which is essentially added chromium which, above 10.5% in solution (depending on the carbon content) in the matrix, causes the formation of a protective layer of chromium oxide which gives these steels their stainless steel. Other elements are added, in particular nickel which improves the mechanical properties in general and ductility in particular, molybdenum or titanium improve the stability of the alloy for temperatures other than ambient as well as elements with high points melting, such as vanadium and tungsten, generally accompanied by an increase in the chromium content, to obtain resistance to high temperatures in contact with a flame (refractory steels) [24-25].

I.2.Passivation mechanism of stainless steels

Passivation or passivity [26-27] represents a state of metals or alloys in which their corrosion rate is notably slowed down by the presence of a natural or artificial passive film, compared to what it would be in the absence of this film.

In most cases (aluminium, steel, stainless steel, titanium etc.), this passive film appears spontaneously by oxidation, because the oxide formed on the surface is insoluble and constitutes an obstacle which slows down subsequent processes. In an aqueous medium, the formation of this film is linked to an electrochemical potential range as well as to a pH range in which the oxide is stable. Therefore, we focus on the passive film forming in the air before commissioning of the part.

Stainless steels are covered with a very thin protective oxide film on the surface of the metal alloy, giving them good corrosion resistance. This passive layer is 1 to 3 nanometers thick, it forms and renews itself in the presence of oxygen or water. It is composed of a mixture of iron oxide, chromium oxide and, if molybdenum is present in the block steel, there will be the presence of an oxide of molybdenum.

I.3.The role of alloying element

The additional elements are divided into two families: the alphagenic elements (silicon, aluminum, chromium, molybdenum, tungsten, titanium, niobium), i.e. they promote the formation of a centered cubic crystallographic structure and gammagenic elements (nickel, manganese, nitrogen, carbon, copper, cobalt), that is to say they promote the formation of a cubic crystallographic structure with centered faces. Some elements have more important effects than

others, notably nitrogen and carbon, whose gammagenic effect is about thirty times more powerful than that of nickel.

I.3.1. Alphagenic elements

Chromium (Cr): The minimum content of about 10.5% is necessary to form a stable passive chromium film sufficient to protect the steel against moderate atmospheric corrosion. Corrosion resistance increases with the chromium content. Chromium also increases resistance to oxidation at high temperatures.

Molybdenum (Mo): It is an alpha iron forming element and improves the corrosion resistance of stainless steels in reducing environments. In the presence of halogen ion, it particularly improves resistance to pitting corrosion. In addition, it increases the mechanical resistance when hot.

Silicon (Si): It increases the resistance to corrosion and improves the properties of use at high temperature which gives it good resistance to hot oxidation in the case of nitric acid but decreases the resistance to cracking during welding.

Titanium (Ti): Must be used at a content that exceeds four times the carbon content. It prevents alteration of metallurgical structures during hot work, in particular during welding work.

Niobium (Nb): It is an alphagene element, it combines with carbon in stainless steels and forms carbides to resist intergranular corrosion.

I.3.2.Gammagenic elements

Nitrogen (N): It is an austenite stabilizer when associated with a low content of carbon. Nitrogen enables high yield strengths to be reached without reducing resistance to intergranular corrosion. It has a beneficial influence on the resistance to pitting corrosion. Nitrogen also increases the tensile strength and decreases the ductility of austenitic stainless steels.

Nickel (Ni): Above 6% to 8%, its presence results in a gammagenic effect and the steel becomes austenitic at all temperatures. It thus broadens the domain of existence of Austenite. It favors the implementation by plastic deformation. Improves corrosion resistance, especially stress corrosion resistance, refines grain and improves ductility. Nickel has a favorable influence on hardenability and impact resistance.

Sulfur (S): At contents of around 0.2%, it significantly improves machinability (turning, milling, drilling, etc.) but this comes at the expense of resistance to pitting corrosion.

Manganese: It stabilizes gamma iron and has no recognized influence on corrosion resistance. It makes it more difficult to transform austenite into alpha martensite in CrNi steels and under mechanical stress at low temperatures.

Carbon (C): Strong gammagenic element, helps stabilize austenite during cold deformation. On the other hand, it can cause the formation of intergranular chromium carbides Cr23C6 which reduce the resistance to intergranular corrosion.

I.4.Phase balance diagrams Iron-carbon system

Carbon is the essential non-metallic element in all steels. The Fe-C diagram is well known (Figure I.1) and shows the polymorphism of iron in the solid state. It is a powerful gammagenic element which very strongly favors the solid solution domain of carbon insertion in the austenitic structure of iron. For reasons of corrosion resistance, the carbon content of stainless steels is, in most cases, kept very low.

Figure I.1. Fe-C equilibrium diagram [28]

Most of the carbon is in solution. The maximum solubility of carbon in austenite is of the order of 2% at the temperature of the eutectic bearing while it is less than 0.1% in α ferrite

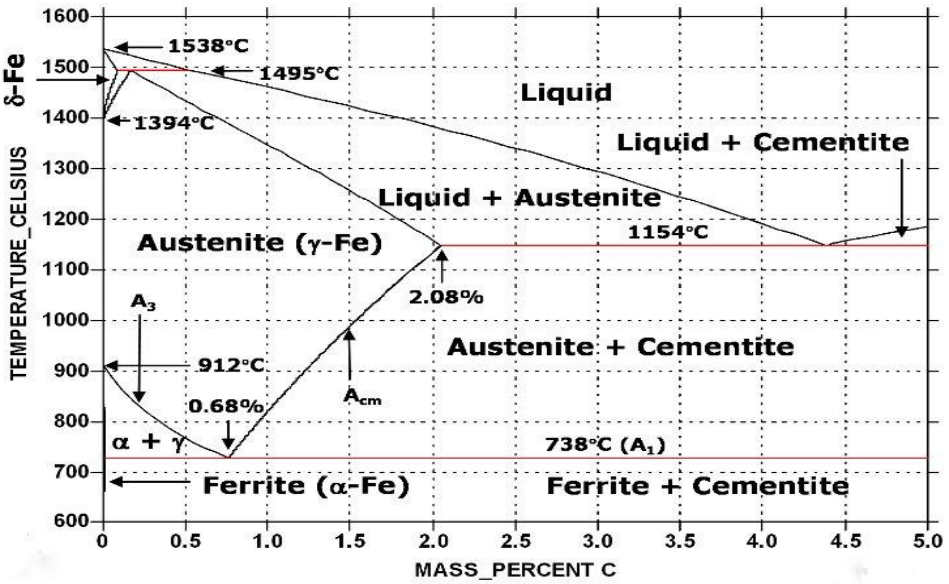

(eutectoid bearing) and in δ ferrite (peritectic bearing).

I.4.1.Iron - Chrome System:

Chromium is the cause of the passivation of steels and above 11% constitutes the essential alloying element of stainless steels. The Fe-Cr phase diagram (Figure I.2) shows that the extent of the austenitic domain decreases as the chromium content increases. Above 11 to 13% Cr, the metal is entirely ferritic. At lower temperatures, the Fe-Cr diagram shows the appearance of a new phase, the ζ phase. This intermetallic phase rich in chromium, almost 50%, is extremely hard and has the main effect of making the alloy very brittle.

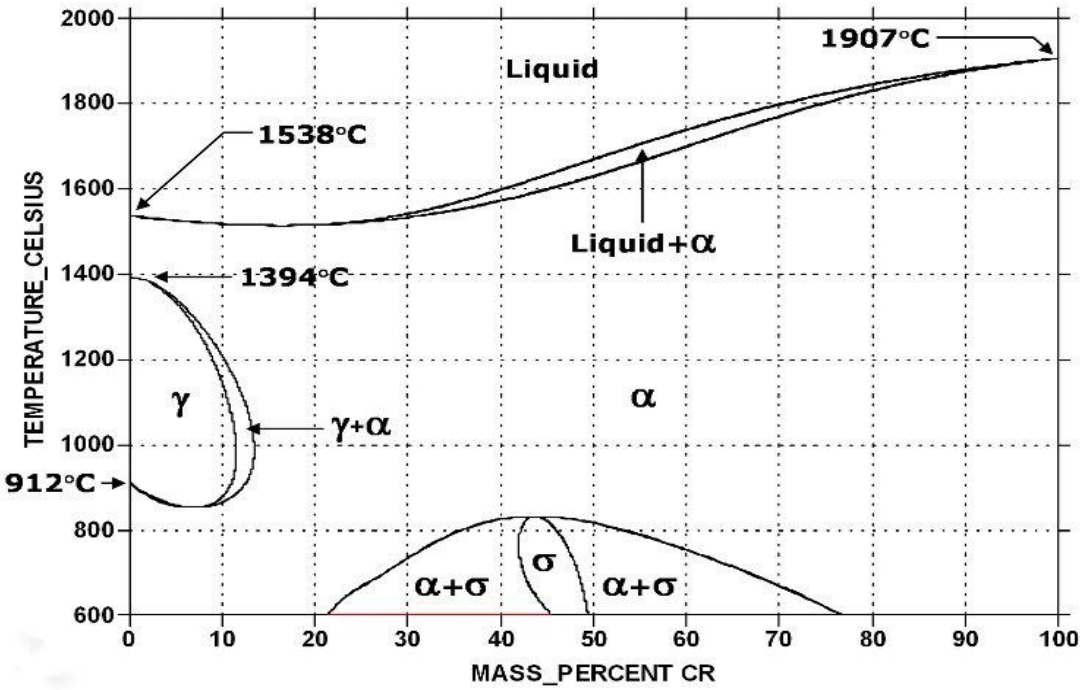

Figure I.2. Equilibrium diagram of binary iron-chromium alloys [29]

I.4.2.Iron-Chrome-Nickel System

Nickel, a gamma-genic element, widens the range of existence of the austenitic phase. Figure I.3, which is a cross-section of the Fe-Cr-Ni ternary diagram, shows the shift of the γ loop towards the high chromium contents as the nickel content is increased. The gamma-genic effect of nickel, however, is much weaker than that of carbon. If, by convention, the gamma- genic effect of nickel is assigned a coefficient equal to unity that of carbon is generally assigned a coefficient equal to 30.

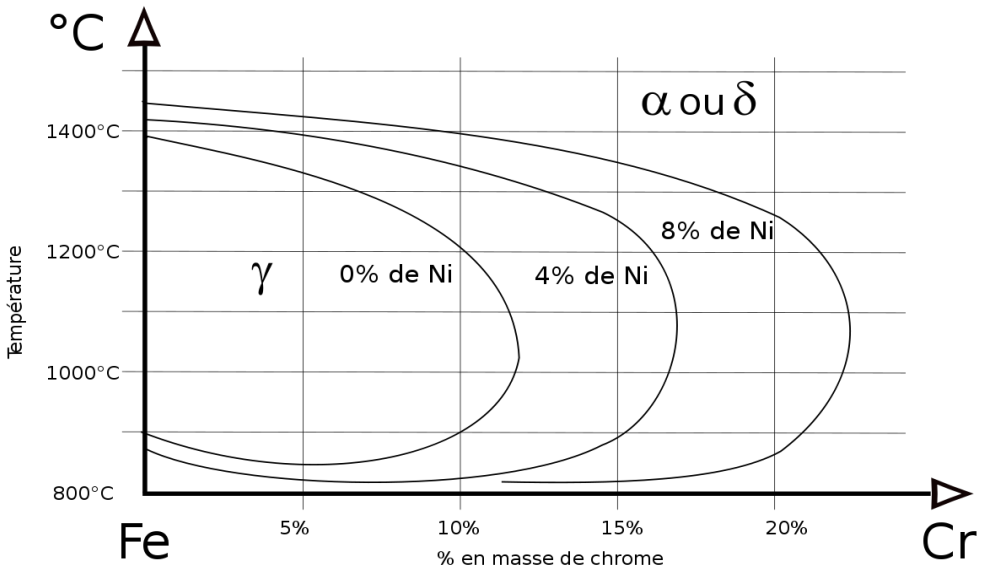

Figure I.3. Sections of the Fe-Cr-Ni ternary diagram for increasing nickel contents [29]

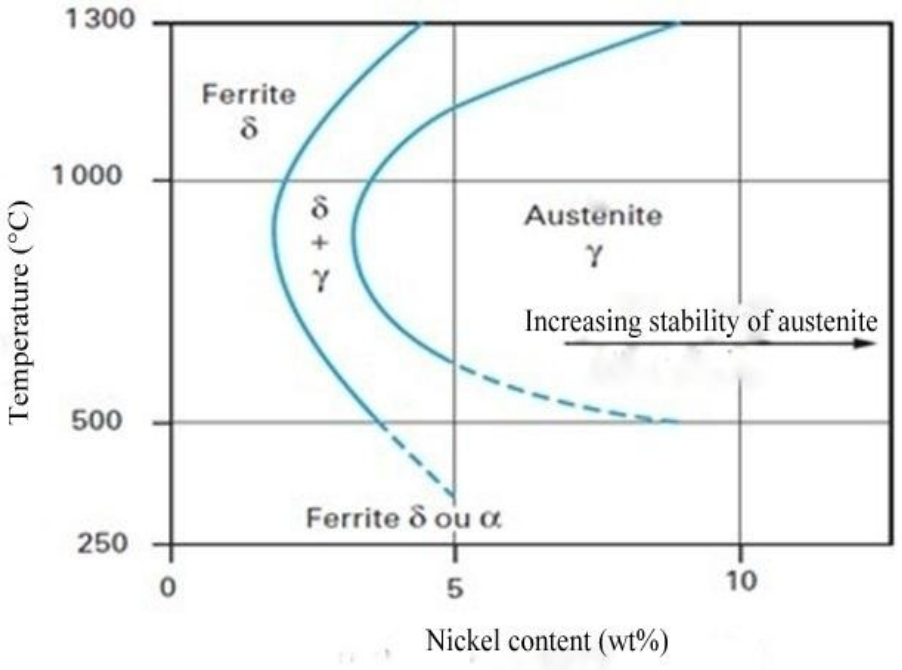

Figure I.4. Equilibrium structure of 18% Cr low carbon steel [29]

For an alloy containing 18% chromium (the most representative of austenitic grades), it is shown (Figure I.4) that if the nickel content remains below about 2%, the structure remains ferritic throughout the temperature range. Beyond a content of 2% nickel, we observe the appearance of a two-phase α + γ structure called austeno-ferritic. Beyond about 4% nickel, the domain of existence

of γ austenite widens from the melting temperature up to about 500°C for nickel contents of the order of 8 to 10%.

I.4.3.The concepts of equivalent chromium and nickel

The structure of stainless steels depends mainly on their chemical composition. The main and characteristic chemical elements of these steels are chromium (alphagene) and nickel (gammagen). Certain elements have the same influence on the structure as chromium, and others the same as nickel, with, of course, different relative importance, which makes it possible to define the concepts of equivalent nickel and chromium. These two quantities are obtained by the following expressions:

Ni_{eq} = %Ni + 30%C + 0,5 %Mn

Cr_{eq} = %Cr + %Mo + 1,5%Si + 0,5%Nb

It is possible to summarize, for the same heat treatment, the influence of the chemical elements on the structure in Figure I.5 by plotting the equivalent nickel on the ordinate, and the equivalent chromium on the abscissa.

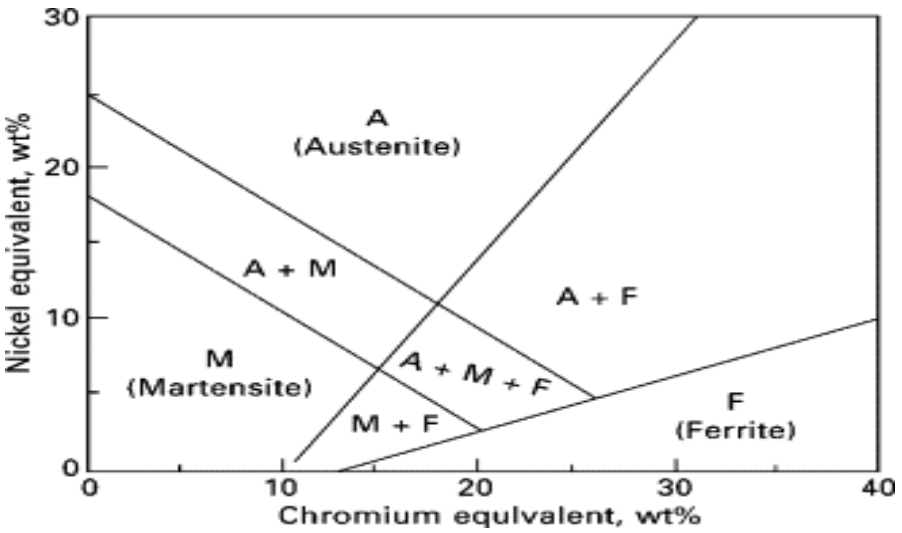

Figure I.5: Schaeffer diagram for stainless steels [30]

This diagram shows that it is possible to obtain different structures depending on the concentration of a number of elements.

I.5.Classification of stainless steels

There are four classes of stainless steels (of different crystallographic structure), the use of which depends on the desired properties

- Ferritic steels (centered cubic structure).
- Martensitic steels (quadratic structure).
- Austenitic steels (face-centered cubic structure).
- Austenoferritic steels (duplex).
- Precipitation hardening stainless steels

I.5.1.Ferritic steels.

Ferritic stainless steels [31-32] are characterized by the fact that their structure remains ferritic throughout the temperature range, that is, they do not undergo α↔γ transformation. They have very low carbon content (around 0.07% carbon). The chromium content is between 11 and 29%. They do not contain nickel. Ferritic steels are magnetic at room temperature. They are moderately ductile.

I.5.2.Austenitic stainless steels

Austenitic stainless steels of Fe-Cr-Ni composition have their face-centred cubic-type crystallographic structure which gives them exceptional ductility and toughness. It is also necessary to add an excellent metallurgical weldability, which facilitates their implementation. These are the most widely used stainless steels, in the chemical and food industries, to make cutlery, etc..

I.5.3.Martensitic (magnetic) stainless steels

These steels, with a quadratic structure, are represented by grades at 13% Cr. They are obtained by reheating a high temperature carbon-rich stainless steel followed by rapid cooling called "quenching». Martensitic steels are generally less resistant to corrosion than ferritic steels.

I.5.4.Austeno-ferritic steels (duplex)

Alloys with the composition (Cr, Ni, Mo, and Si) are balanced to obtain, by heat treatment, a mixed structure consisting of ferrite (70 to 50%) and austenite (30 to 50%). This state gives these steels excellent performance such as ductility, toughness and corrosion resistance. These steels are used in relatively aggressive conditions: chemical, petroleum and maritime industries.

I.5.5.Precipitation hardening stainless steels

The mechanical characteristics of this family of stainless steels are obtained at the end of a secondary hardening treatment followed by a heat treatment of quenching or quenching.

I.6.Austenitic steels

Austenitic stainless steels [33-34] are alloys of iron and carbon which generally contain 0.02% to 0.1% carbon, 17 to 20% chromium, 7 to 25% nickel, 2 to 5% carbon. molybdenum and other addition elements such as copper, silicon, titanium, niobium ... The addition elements make it possible to improve the corrosion resistance or the mechanical properties of the material.

The austenitic structure in these alloys is perfectly stable at high temperature, but at room temperature this structure is in a metastable state. Austenite is not the equilibrium phase and can transform into another so-called martensitic phase.

I.6.1.Classification of austenitic stainless steels

Depending on the carbon content and the addition elements, austenitic steels are classified as follows:

1) **Austenitic steels without molybdenum:** These grades are widely used because they provide a good compromise between cost and resistance to corrosion.
2) **Austenitic Molybdenum Steels:** Molybdenum improves resistance to pitting corrosion (in the presence of chlorides).
3) **Very low carbon austenitic steels:** A carbon content of less than 0.03% helps prevent intergranular corrosion because carbon remains in solid solution and does not combine with chromium to form chromium carbides.
4) **Stabilized austenitic steels:** The addition of titanium and/or niobium prevents precipitation of chromium carbides following a heat treatment operation and /or welding processes. These steels also have good mechanical properties up to 600°C.
5) **Super austenitic steels:** Nickel and nitrogen enriched contents provide a fully austenitic structure to these steels initially enriched in chromium and molybdenum, which gives them excellent resistance to corrosion in an aggressive environment.

I.6.2.Properties of austenitic stainless steels

Austenitic steels have good resistance to corrosion in general. They do not show any hardening after heat treatment; their mechanical properties can be increased by addition of nitrogen or by cold deformation.

These steels are generally delivered in the hyper-hardened state: they have undergone heating to around 1050 ° C (solution of chromium carbides) then rapid cooling in air or water (to prevent precipitation of the chromium carbides). Chromium carbides).

They are characterized by good weldability associated with good resilience at low temperature, and good safety vis-à-vis the risk of brittle fracture, which justifies their use in the field of pressure equipment.

I.7.Stress corrosion

Stress corrosion is another form of corrosion that is important in many fields, including civil engineering structures.

Stress corrosion [35-37] occurs when a material exists in a relatively inert environment but corrodes under the effect of applied stress. The stress can be applied externally or residual. This form of corrosion is particularly dangerous because it cannot occur under certain specific conditions before a stress is applied. Corrosion is not clearly visible before failure and can lead to catastrophic failure.

Many alloys can undergo stress corrosion, and the applied stress can also be due to residual stress in the material. An example of residual stress could be residual stress in a material after forming or stress due to welding.

Stress corrosion cracking [38-39] typically causes brittle failure of the material, which can have serious consequences as there are usually few or no warnings before failure occurs. Stress corrosion is a form of galvanic corrosion, in which areas of material under stress are anodic to unstressed areas of the material. Practically, the best way to control stress corrosion cracking is to limit or reduce the stresses placed on a material when it is in a corrosive atmosphere.

I.7.1.Static Stress

A static stress is a constant stress over the extent of the solid with a uniform or homogeneous strain image; this is for example, the state of stress that prevails in a gas which undergoes uniform expansion; like a uniform strain, a static stress [40] is extremely difficult to achieve on the whole of a solid but easier to approach on a well-designed part of that solid.

I.7.2.Residual stress

Residual stresses are stresses stuck in a metallic object, even if the latter is free from external forces. These stresses result from a region of the metal being constrained by adjacent regions to expand, contract, or release elastic stresses. The residual stresses [41-42] can be in tension or in compression. In fact, residual tensile and compressive stresses coexist in a component.

Residual stresses are spontaneously in equilibrium as residual tensile stresses (harmful) and residual compressive stresses (beneficial). For example, a surface formed under tensile stresses will include compressive residual stresses, and a surface formed under compressive stresses will contain residual tensile stresses.

I.7.2.1Residual tensile stresses

Residual tensile stresses decrease fatigue resistance and cause fatigue failure. Residual tensile stresses are usually the side effects of production, such as aggressive grinding which causes crack growth. They can also be introduced with shrinkage, adjustment, bending or twisting. For example, moulded components generally have residual stresses in the form of residual stresses that can cause cracking on the component surface. In addition, stress corrosion cracking is a phenomenon that occurs in the presence of residual tensile stresses.

I.7.2.2.Residual compressive stresses

Residual compressive stresses increase both fatigue resistance and resistance to stress corrosion cracking. They are intentionally formed by various processes such as blasting, laser blasting, low plasticity burnishing, and auto-shrinking. These processes cold work or harden the material. Often the real purpose of inducing residual compressive stresses is to balance the damaging effects of tensile stresses**;** Figure I.68**.** One of the heats treatments processes, stress relaxation annealing, can also be used to reduce residual tensile stresses. The total stress of a component is the sum of all the applied service stresses and the residual stresses.

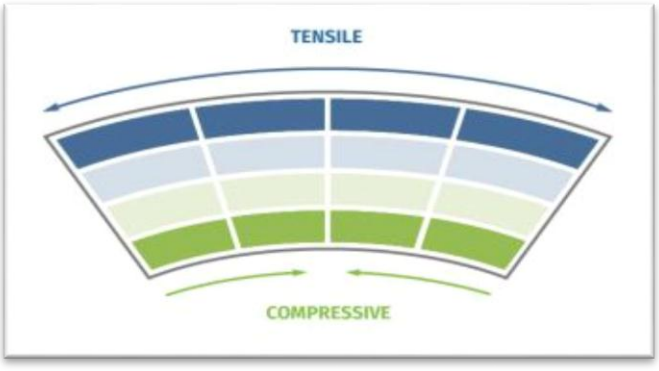

Figure I.6. Formation of tensile and compressive stresses on a bent sample

There are three different known residual stresses:

- **Residual Stress Type**

The macro-residual stresses are developed in several grains. Any modification of the balance of type 1 residual stresses will lead to a modification of the macroscopic dimensions. Any treatment or process leading to an inhomogeneous distribution of the strains produces type 1 residual stresses.

- **Residual stress Type-2**

Micro-residual stresses are developed in a grain. They can be of different sizes in different grains. A particularly martensitic transformation produces residual stresses of type 2. During the transformation, an incomplete transformation of the austenite is observed. The volume martensitic is greater than that of austenite and this difference forms residual stresses.

- **Residual stress Type-3**

Sub-micro residual stresses are developed in several atomic distances of the grain. Formation is caused by crystal defects such as vacancies, dislocations, etc. In real life, components have all types of residual stresses. All manufacturing processes create some degree of residual stress. The effect of these stresses could be imperceptible or create cracks. Cast and welded components, in particular, without an external load at room temperature can fail catastrophically due to residual stresses. Residual stresses directly affect the life of components. Failures and other problems caused by residual stresses have caused industries to focus on finding, controlling, measuring and revitalizing residual stresses thus residual stresses have become an important research topic in the engineering world today.

I.7.2.3.The causes of residual stress

Residual stresses appear whenever a component is stressed beyond its yield strength and plastic deformation occurs. Plastic deformation occurs when the stress exceeds the yield strength of a metal. It may be as a result of:

- Non-uniform plastic deformation during mechanical processing, such as rolling, forming operations (bending or stretching), machining and mechanical surface treatments (shot peening and roller polishing).
- Phase transformations during cooling from elevated temperatures
- Non-uniform plastic deformation upon heating or cooling.

- Heterogeneity of a chemical or crystallographic order (nitriding or cementation)

A. Residual stress due to temperature variations

In parts cooled by high temperatures [43], residual stresses are caused by temperature changes in the metal during cooling; Figure I.7. Cooling from high temperatures occurs during heat treatment and welding.

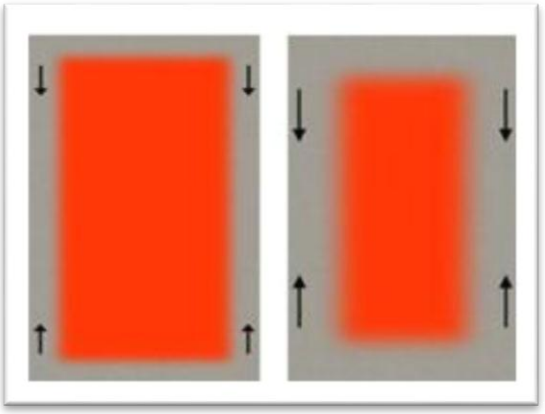

Figure I.7. Residual stress due to temperature variations

Changes in temperature in a metal during cooling from an elevated temperature cause localized changes in the amount of thermal contraction. Thermal contraction generates non-uniform stresses due to the different cooling rates experienced by the surface and the interior of the metal. During cooling, the outer part of a component cools down first and that part of the metal contracts, compressing the hotter inner metal. When the internal part of the component cools, the metal tries to contract, but is constrained by the already cooled external part. As a result, the inner part will have residual tensile stress and the outer part of the component will have residual compressive stress.

B. Residual stress due to phase transformation

A phase transformation is a change in the metallurgical phases present in an alloy; Figure I.8, For example, the transformation austenitic to martensitic in steel during full hardening is a phase transformation. The residual stresses generated during a phase transformation are due to the volume.

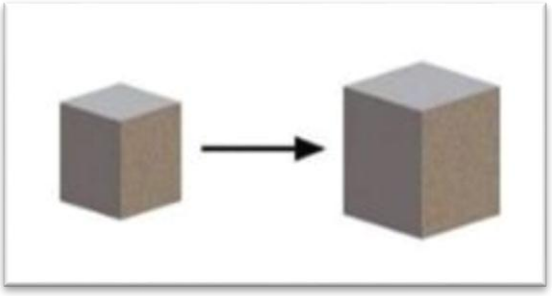

Figure I.8. Difference between the newly formed and initial metallurgical phases

For phase transformations that occur during cooling from an elevated temperature, such as in steel, the outer parts of the metal cool first and undergo the phase transformation first; Figure I.9. If the volume of the new phase is different from the volume of the initial phase, the volume of metal transformed will change as the new phase is formed. As the metal cools, it will also attempt to increase or decrease its volume. However, the change in volume of the metal interior will be limited by the cooler outer layer of metal that has already transformed.

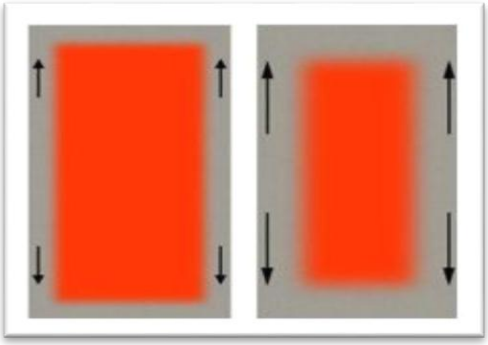

Figure I.9. Residual stress due to phase transformation

When the volume of the new phase is greater than the volume of the initial phase, the central part of the component will be under compression and the surface will be under tension. When the volume of the new phase is less than the volume of the initial phase, the central part of the component will be under tension and the part of the metal on the surface and near the surface will be under compression.

For example, upon complete hardening of steel during quenching, austenite turns into martensite, the volume of martensite being about 4% greater than that of austenite. During quenching, the steel on the surface first turns to martensite since the surface cools the fastest. As the metal inside continues to cool, it turns into martensite. However, its volume expansion is limited by the hardened and cooler surface layer. This stress causes compression of the interior and tension of the exterior surface.

Under certain conditions, changes in volume can produce residual stresses large enough to cause plastic deformation, resulting in warping or deformation of components. With severe quenching, the quench stresses can be so great that they cause cracks.

C. Residual stresses caused by mechanical treatment

Residual stresses also appear when plastic deformation is not uniform in the cross section of an article being deformed, for example during bending, stretching, rolling and extruding. When a metal undergoes plastic deformation, part of the deformation is elastic. Once the load causing the strain is removed, the metal attempts to recover the elastic part of the strain. However, the elastic recovery is incomplete because it is opposed by the adjacent plastically deformed material. Figure I.10

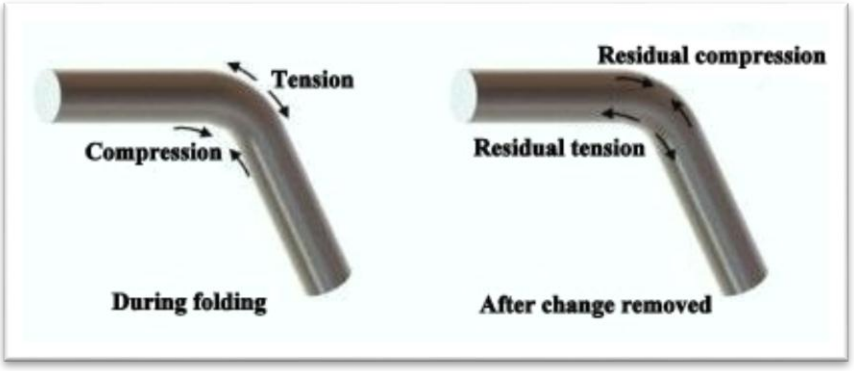

Figure I.10. Residual stress caused by mechanical treatment

Consider a metal article that has been bent. The regions adjacent to the curvature will only have undergone elastic deformation and this region will attempt to recover, a phenomenon known as spring back. After the removal of the external force, the regions that have been bent prevent the adjacent regions from undergoing full elastic recovery to the undeformed condition. These regions are left in a state of residual tension and the plastically deformed regions are in a state of residual compression.

In general, the sign of the residual stress produced by non-uniform strain [44] will be opposite to the sign of the plastic strain which produced the residual stress.

I.7.2.4.Effects of residual stress

Residual stress can be beneficial or detrimental, depending on whether the stress is strained or compressive. The residual tensile stresses can be large enough to cause component distortion or cracking. In addition, fatigue and stress corrosion cracking require the presence of tensile stresses. Since the residual stresses are added algebraically to the applied stresses, the surface residual tensile stresses combined with an applied tensile stress can reduce the reliability of the components. In fact, sometimes residual tensile stress is sufficient to cause stress corrosion cracking.

Residual surface compressive stresses are generally useful because they reduce the effects of applied tensile stresses. In most cases, the superficial compressive stresses help to improve fatigue resistance and resistance to stress corrosion cracking.

I.7.2.5. Control of residual stress

Control of the type and magnitude of residual stresses is important for applications where components will be exposed to stress corrosion fatigue or cracking conditions or if the residual stresses are large enough to cause deformation or cracking components. This can be achieved by mechanical treatment, stress relieving heat treatment, control of heat treatment processes and alloy selection.

Mechanical treatments such as cold shot peening; cold rolling, stretching, and small compressions are used to intentionally induce residual compressive stress on the surface of a component.

Since the yield strength of the metal decreases as its temperature increases, metals can be relieved by heating to a temperature where the yield strength of the metal is the same or less than the magnitude of the residual stress. At this temperature, the metal can undergo microscopic plastic deformation, thus releasing at least part of the residual stress. After stress relief, the maximum residual stress that can remain is equal to the elastic limit of the material at the stress relief temperature.

From a component processing point of view, residual stresses can be minimized by using reduced cooling rates to reduce temperature variations and allow phase transformations to occur more evenly across the cross section of the machine. a component. Additionally, alloys can be chosen to combine lower cooling rates, while still allowing desired phase transformations to occur. For example, for hardened carbon steel components, low alloy carbon steels allow slower cooling rates to be used than ordinary carbon steels.

I.8. Welding processes for austenitic stainless steels

Welding is a permanent joining process by which "materials of the same or the same type are joined together through a chemical reaction resulting from a combined action of heat and pressure". To ensure the continuity of the material, the atoms at the boundary of the joint must "reach distances of the order of magnitude of the inter-node distances of their own crystal system".

I.8.1. Weldability of Steel

The main factors that influence the weldability of steel are: Hardenability, carbon equivalent, preheating and cracking phenomena. Several formulas have been proposed to define the weldability of steels [45-46] and assess the effect on hardenability; they allow the equivalent carbon to be calculated by the equation:

$$C_{éq}\% = C + \frac{Mn}{6} + \frac{Cr + Mo + V}{5} + \frac{Ni + Cu\%}{15}$$

Ceq : Metallurgical equivalent carbon

If Ceq ≤ 0.40, we weld without precaution,

If 0.41 ≤ Ceq ≤ 0.60, a preheating is carried out with a temperature between 100 to 250°C,

If Ceq ≥ 0.6, steel is difficult to weld.

I.8.1.1.Welding of austenitic stainless steels

The microstructure, at room temperature, of the molten metal in the welds of austenitic stainless steels depends on both the solidification parameters and the transformations in the solid state. Austenitic stainless steels can solidify as primary ferrite or primary austenite, depending on the chemical composition of the filler metal.

Four types of solidification can occur in the welds of austenitic stainless steels:

- **Type A:** the molten bath solidifies into primary austenite. No transformation into ferrite occurs in this type of solidification.

-**Type AF:** a percentage of ferrite appears after solidification to primary austenite via the eutectic transformation.

- **Type FA:** the molten bath solidifies into primary ferrite then a transformation of a few austenitic grains appears at the end of solidification.

- **Type F:** the molten bath solidifies entirely into ferrite. No transformation to austenite occurs in this type of solidification. This type of solidification is less common in austenitic stainless steels.

I.8.2. Welding characteristics

To obtain a welded joint [47] under ideal conditions, there must be, between the welded parts, a perfect continuity from the point of view of the properties of the material, more

particularly on the mechanical, physical and metallurgical level. In practice, these conditions are only very rarely met. However, there are many ways to obtain welds whose properties are sufficiently close to the ideal conditions or the minimum conditions desired for the execution of a welded joint.

Welding processes must be adapted to the required operating conditions, hence the need for a judicious choice of the process and the conditions under which the welding will be carried out.

I.8.2.1. Metallurgical characteristics

To unite 2 surfaces satisfactorily, these must be examples of oxides, organic films or absorbed gases. Although useful, cleaning surfaces is not always essential if the welding process dissolves or disperses surface films (chemical action of a flux, direct action of the electric arc or mechanical means). During the welding operation, the films must not reform. Almost all welding processes are carried out shielded from the atmosphere with appropriate protection. The execution of the weld, which must make it possible to obtain a welded joint having the desired properties (mechanical, metallurgical, etc.), requires 4 conditions:

1. Have a source of energy to unite the faces by fusion or pressure
2. The process must be able to eliminate contamination from the two sides to be joined.
3. During the welding operation, avoid atmospheric contamination or its effects.
4. Have metallurgical control of the weld.

The welded joint contains different zones [48], the mechanical properties of which depend on several factors, such as the cooling rate, grain size and residual stresses. The welded joint, as shown in Figure I.11. May consist of:

- **The Fusion zone (FZ):** Where the maximum thermal effect made it possible to temporarily reach the liquid state, possibly with the participation of a filler metal.
- **The Heat Affected Zone (HAZ):** Where the thermal action was sufficient to introduce structural modifications into the base metal, a function of the residence time at high temperature and of the cooling kinetics.
- **The Binding Zone (BZ):** This zone forms the link between the molten zone and the HAZ, it corresponds to the first solidification point of the molten bath.
- **Unaffected Zone or Base Metal (BM):** Also called the unaffected zone, there is no change in metallurgical structure in this zone because it has not undergone heating during the thermal cycle of the molten bath.

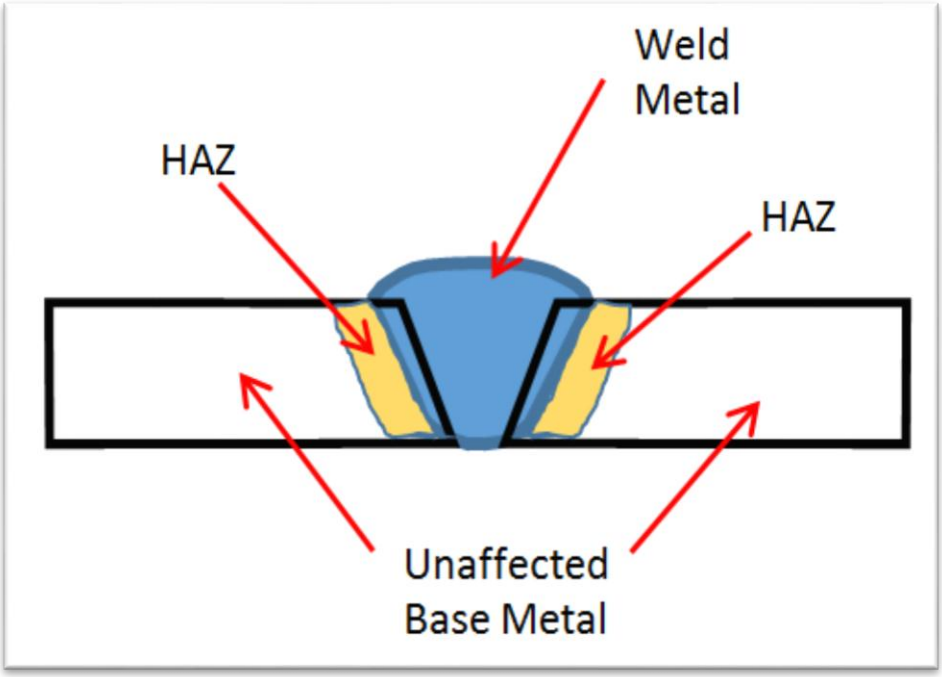

The profile and extent of these different zones vary according to the energy and the thermal cycle of welding, the heat treatments carried out before, during or after welding.

Figure I. 11. Different parts of a welded joint.

I.8. 2.2.Thermal cycle characteristics

During welding there is a production of local heating of the parts to be welded with the addition of liquid metal. This heat input [49-50] travels along the joint to be welded. Each point of the welded zone as well as its vicinity undergoes a thermal cycle, that is to say a rapid heating and a more or less slow cooling.

Knowledge of the thermal cycle that has undergone the assembly at the weld level is necessary to interpret the metallurgical phenomena resulting from the welding operation. This cycle corresponds to the temperature variation as a function of time during welding.

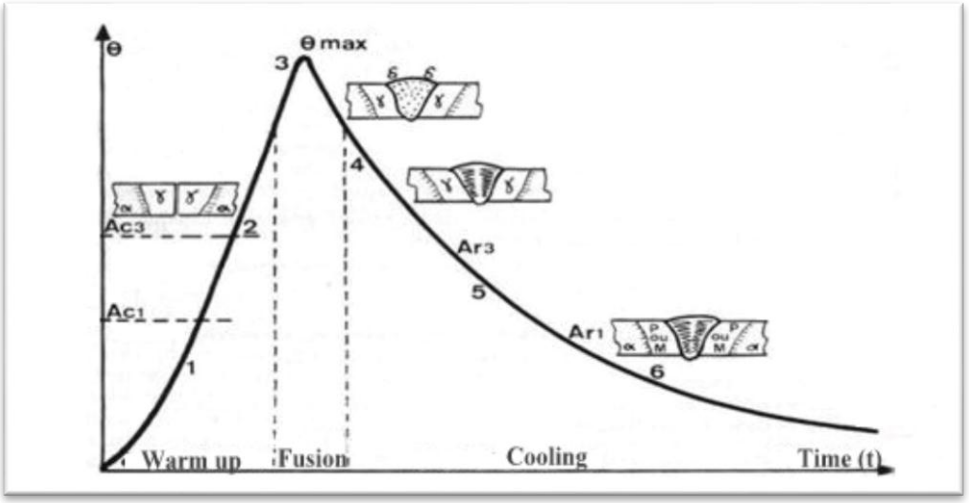

Figure I.12. Welding thermal cycle.

I.8.2.3. Classification of the main welding processes

Any attempt to classify the different welding processes is made difficult in view of the many variations from one process to another. For example, some processes where pressure is used during the welding process (electrical resistance spot welding) are in fact liquid phase processes. Table I.1 classifies protection elements based on the energy source.

Table.I.1. Classification of the main welding processes

Sources of energy	Welded joint protection elements				
	Solid flux	Inert gas	Actif gas	Under vacuum	Without protection
Electric arc	Coated electrodes Automatic under solid flow M.A.G with cored wire	T.I.G * M.I.G ** with fusible electrode wire Electrogas Plasma	M.A.G *** with fusible electrode wire		Stud welding With carbon electrode By capacitor discharge
Electrical resistance					By point By boss By sparking at the end, Pure resistance
Optic		Laser		Electronic bombardment	Laser
Thermochemic	Aluminothermy	Non-transferred plasma-arc	Oxyacetylene Oxypropane Oxydric		
Mechanic				By cold pressing	By friction By cold pressing By ultrasound By explosion at the forge

* Tungsten electrod –Inert Gas
** Metal Inert Gas
*** Metal Active Gas

I.8.3.The defects of a weld

The quality of a weld can be impaired by several types of defects:

A. Cracks

Joint defects are the most common and can be found in any metal area. A distinction is made between hot cracks and cold cracks [51-52]. The former appear when the molten zone solidifies due to excessively narrow joints, the presence of impurities or an incompatibility of the filler metal. Cold cracks are likely to appear several hours or days after welding due to too rapid cooling, humidity in the air, etc.

B. Weld bead corrosion

Welding is the juxtaposition of two different metals. We can therefore have a phenomenon of galvanic corrosion. This defect can occur in the case of heterogeneous welding of a poorly designed assembly, subject to the presence of an electrolyte. In addition, we can also see the appearance of an inter-facial corrosion phenomenon, which can be encountered during the segregation of boron at the grain boundaries in nickel bases or during the segregation of carbon at the grain boundaries in stainless steels.

C. Porosities

These are hollow spherical defects which may or may not be open; they are caused by drafts, lack of gas, obstruction of the nozzle, bad welding angle, water or impurities in the solder joint ... etc.

D. Contaminations

Unwanted contaminations are common. Metal projections (in the form of splashes) are possible on the surface of the base metal and the bead being formed. The inclusions of welding co-products or dust increase the fragilisation of the metal. When the welding field is not sufficiently protected, the contact of the molten metal with active elements (such as oxygen, sulphur or phosphorus) leads to chemical reactions, some of which cause precipitates or the oxidation of the material.

I.8.4. TIG process

The choice of the welding process, whatever the material to be joined, can pose a difficult problem to solve. There are actually a number of factors that determine the choice. The thickness of the material, the geometry of the bead, the position of the weld, the shape of the weld pool and the welding parameters play an important role in this choice. Nevertheless, it is advisable to use

the TIG process [53-55] when the shape of the weld pool (penetration and width) must be strictly controlled.

The advantages of the TIG process are linked to the fact that the arc obtained with a refractory (tungsten) electrode is easily controllable and that its power is not limited by the diameter of the electrodes as when they are coated. In addition, when it is necessary to use a filler metal, the filler wire is fed separately, which makes it possible to control all process parameters individually and precisely; unlike other processes (MIG, MAG, FE ...). Where it is much more difficult to master them.

I.8.5.Description of the TIG welding principle

The heat required for welding is produced by an electric arc spurting between a tungsten electrode and the work pieces. Tungsten does not melt at welding temperatures (3500°C). The arc and the weld pool are protected by an inert atmosphere, argon jet or sometimes argon + helium. The filler metal is independent of the welding torch and is in the form of a rod held by the operator, or in the form of a wire if the welding is automatic FigureI.13.

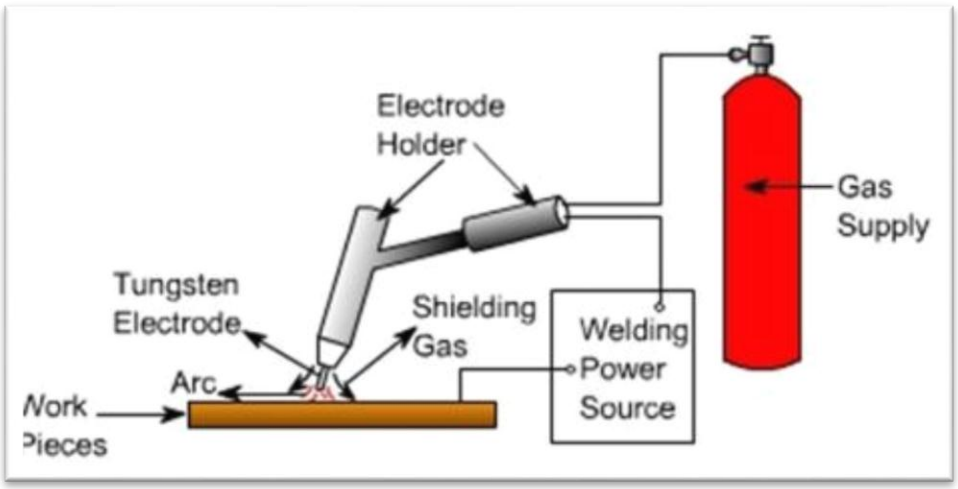

Figure I.13. Schematic Diagram of TIG Welding System.

A. Welding current generator

They have plunging external characteristics, like those of arc welding with coated electrodes.

A.1.Alternative current

It is essential for welding aluminum and its alloys. The alternating current has a mechanical action inside the molten metal and tends to break the layer of alumina. A device makes it possible to stabilize the arc and to initiate remotely in order to avoid pollution of the weld pool. Usually a high frequency generator and electrode are used and made of pure tungsten or 0.3 to 0.5% zirconium.

A.2.Continuous current

The electrode is always at the negative pole in order to avoid its disintegration by the bombardment of electrons emitted by the part. The generator's static external characteristics are plunging, with no spike in starting current (a spike that would burst the tungsten electrode). Direct current is used for welding steels, stainless steels and copper. The electrode is thoriated tungsten (1 or 2%). The addition of thorium allows for a higher current density, less electrode wear and easier ignition.

B. Filler metal and workpiece

The filler metal must be of high purity and of a chemical composition close to that of the base metal of the parts to be welded. The filler metal and the edges to be welded must be pickled and free from any contamination (oxides, grease, contamination by particles of other metals, etc.

Beyond a certain thickness of the parts to be welded (e> = 10 mm) for aluminum and its alloys and for stainless and refractory steels, the M.I.G. is more advantageous.

C. Protective gas

C.1.Pure argon

- 99.995% purity for high quality welding on aluminum and alloys.
- Purity 99.99% for welding stainless steels, copper, light alloys.

C.2.Argon + helium

The mixture improves penetration for welding stainless steels; it allows higher speed and better arc stability in automatic welding.

C.3.Argon + helium + hydrogen

The mixture increases the tension of the arc; it allows a higher welding speed. For welding nickel 200 and monel 400, it avoids or significantly reduces the porosity of the joint.

D. Welding speed

The influence of the welding speed can be evaluated by its effect on the linear heat input of welding. The heat input is related to the welding speed by the relation:

$$Q = (I \cdot U)/ v$$

with :

Q : Calorie intake (KJ/cm) ;

1 : Current (A) ;

U: Tension (V);

V: Welding speed (cm/min).

An increase in the welding speed decreases the amount of heat per unit weld length, which results in a decrease in the cross section of the molten zone. However, several authors have found that the arc efficiency is higher when the welding speed is relatively high.

I.8.5.3.Field of application of the process

The GTAW process allows the welding of ferrous and non-ferrous metals and alloys, in particular aluminium, copper and nickel, in all positions. Due to the limitation of the energies involved, it applies mainly to low thicknesses ($e <= 10$ mm). In this case, it is used for multi-pass welding of thick parts or for performing the root pass.

I.8.5.4.Advantages of the process

The joints produced are of very high quality. Welding can be done with or without filler metal. The process is excellent for low thicknesses (0.2 mm to 0.8 mm). The surface finish of the weld bead is very nice (clean and shiny) and the weld pool is not polluted during welding.

I.8.5.5.Disadvantages of the process

The preparation of the edges to be welded must be neat, the chamfers executed with great precision, the filler metal and parts pickled, resulting in a high cost price. The energy efficiency of the arc is low (40%).

I.8.5.6.Effect of welding parameters

The weld parameters control the shape, dimensions and structures of the heated regions of the weld bead. The energy required to melt the metal, which depends on parameters such as welding power and speed, controls the cooling rate. The welding speed directly governs the growth rate of the solidification front and therefore also the shape of the weld pool. The structure and mode of grain growth depend on the linear heat input. The grain growth becomes very fast and gives rise to a coarse structure with increasing heat input while a fine structure is obtained with moderate linear energy. These parameters also affect the induced thermal stresses which apply to the weld and which result in the formation of residual stresses and geometric distortions.

There were many works carried out to study the corrosion resistance [56] and the microstructure of various grades of stainless steel using different welding processes.
A detailed microscopic study has been made to study the effect of welding gun angle on the fusion zone, heat affected zone and base metal. The study on the structure of the specimen's revealed the influence of process parameters on grain structure, grain coarsening in the heat affected zone and weld metal. It also gave an idea about formation of martensite and ferrite veins in the weld metal.
Some of the researchers have been made investigations to weld austenitic stainless steels [57-64], those are discussed as follows. Taban et al. [57] investigated the microstructural, toughness properties and mechanical properties of dissimilar welds joints between Ferritic Stainless Steel Modified 12% Cr and carbon steel. Taban et al. [58] also studied the properties of a modified 12% Cr ferritic stainless steel were evaluated when welded with three different consumables and finally they recommended to use 309 and 316 welding wires for better corrosion resistance compared to 308 welding wires. Mukherjee and Pal [59] studied the influence of heat input on martensite formation and impact property of ferritic-austenitic dissimilar weld metals. Kah et al. Investigate weldability of ferritic stainless steels and their investigation shows that it is possible to provide adequate resistance to hot cracking during welding and usable mechanical properties and resistance to intergranular cracking in the as-welded condition by means of stabilization.

Shanmugam et al.The present study is concerned with the effect of filler metals such as austenitic stainless steel, ferritic stainless steel and duplex stainless steel on tensile and impact

properties of the ferritic stainless steel conforming to AISI 409M grade. it is found that the joints fabricated by duplex stainless steel filler metal showed higher tensile strength and hardness compared to the joints fabricated by austenitic and ferritic stainless steel filler metals. Joints fabricated by austenitic stainless steel filler metal exhibited higher ductility and impact toughness compared with the joints fabricated by ferritic stainless steel and duplex stainless steel filler metals. Lakshminarayanan et al. studied the effect of welding processes such as shielded metal arc welding (SMAW), gas metal arc welding (GMAW) and gas tungsten arc welding (GTAW) on tensile and impact properties of the ferritic stainless steel confirming to AISI 409M grade. They found from their investigation that gas tungsten arc welded joints of ferritic stainless steel have superior tensile and impact properties compared with shielded metal arc and gas metal arc welded joints and this mainly due to the presence of finer grains in fusion zone and heat affected zone. Soasale [60] Analyzed the MIG welding process parameters to optimize bead width, dilution and depth of heat affected zone of weldment.

Ahn et al. [61] also introduced FSW as a proper welding method for 409L ferritic stainless steel due to the comparable mechanical properties and corrosion resistance of the welded zone with the base metal.

Kondapalli Sivaprasad et al. [62] studied the influence of welding parameters on pitting corrosion rate of AISI 304L welded sheets using pulsed current micro plasma arc welding process. They developed an empirical relation correlating various process parameters for pitting corrosion rate. They conducted experiments using five factor and five level central composite rotatable design matrix. They have studied the effects of process parameters using surface and contour plots.

Siva and Murugan [63] studied the effects of plasma transferred arc welding parameters on the pitting corrosion resistance of Colmonoy 5 overlays deposited on austenitic stainless steel plates. They used Potentiodynamic polarization technique for conducting the corrosion tests. A mathematical model was developed using multiple regression technique and the effects were studied.

Subodh and Shahi [64] studied the influence of heat input on the microstructure of GTA welded AISI304 grade stainless steel joints. They used three heat input combinations for their study. They designated the heat combinations as low heat (2.56 kJ/mm), medium heat (2.784 kJ/mm) and high heat (3.017 kJ/mm). From their study, they have found that significant grain

coarsening was inferred in the heat affected zone for all the joints. They have also found that the coverage of grain coarsening in the HAZ increased with the increase in heat input and average dendrite length and interdendritic spacing in the weld zone also increases with the increase in heat input.

Huaibei et al [65] investigated the microstructure analysis of low carbon 12% chromium stainless steel at high temperature in the heat affected zone. The main problems attained during welding with low carbon 12% Cr stainless steel was coarsening and embrittlement. In their study, they did microstructures microstructural investigations in the heat affected zone under high temperature with different chemical constituents and heat inputs using thermal simulation tests. From their study they have inferred that the heat input influences the microstructure of steel in high temperature heat affected zone and the grain size grows up with the increase in heat input.

Chapter 2

Experimental Technique

In this chapter, we present the metal subject of our study which is the austenitic stainless steel AISI304L, in the raw states (before welding) and welded, we present the approach and experimental methods used, subdivided into three sections:

- Metallographic and mechanical characterization (micro-hardness) of the base metal and different microstructural areas of the AISI304L welded joint linked to the change of welding parameters;

- Characterization of electrochemical behavior is described with stationary potentiodynamic polarization tests and non-stationary electrochemical impedance spectroscopy;

- Characterization of the welded joint by using different techniques of non-destructive testing for the investigation of the pitting corrosion.

Each technique by its principle, the experimental set-up used, the operating conditions and the method of processing the results will be detailed in this chapter.

II.1.Study materials

To carry out our study, we chose the grade of pipeline stainless steel AISI 304L according to the standard designation of the American Iron and Steel Institute (X2CrNi18-9 according to the European standard EN10088-1).

Our materials are welded in accordance with ASME IV (2013). The multi-pass GTAW or TIG process was used for the realization of homogeneous butt welds according to normative requirements (figure II.1). Welded joint by filer metal AISI 308L, the dimensions of which are specified by the welding conditions.

Homogeneous welding requires a filler metal of the same grade as the metal to be welded. X-ray fluorescence spectroscopy analysis at GTP/Z (ARZEW-SONATRACH) has enabled it to be check by the mass percentages of the different alloying elements in our materials. The chemical composition is given in Table II.1.

Table II.1: Chemical compositions of the base metal and the filler metal (in Wt. %)

Materiel	Fe	C	Si	Mn	Cr	Ni	Mo	S	P
Base (304L SS)	Balance	0.03	0.35	2.0	18.02	8.0	0.18	0.004	0.01
Filler(308LSS)	Balance	0.07	1.0	1.57	18.15	10.1	-	0.03	0.04

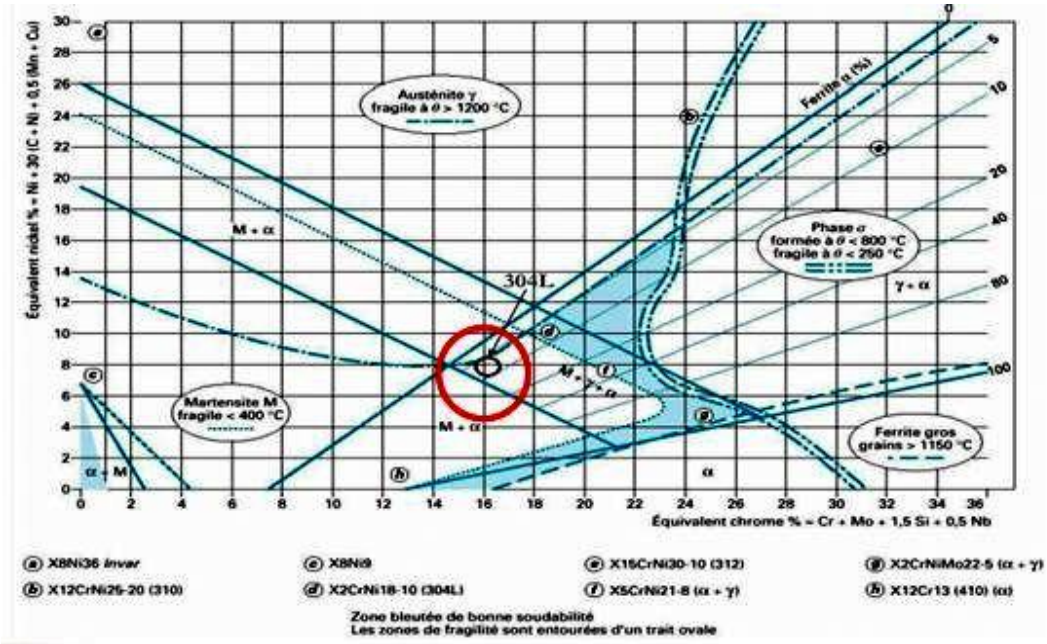

Figure II.1. Schaeffler diagram for AISI 304L

By comparing the two compositions, we notice that the filler metal is chosen with a carbon content close to the base metal content to minimize the risk of precipitation of the Chromium carbides in the weld bath, the choice of welding metal is made according to the Schaeffler diagram [69] as it is illustrated in the (Figure II.1). On the other hand, the nickel content is higher in the AISI308L filler metal in order to stabilize the austenite in the molten zone. We notice that the contents of all elements are within recommended limits for pipeline stainless steels.

II.2. Experiment plan using Factorial Experimental Design (FED)

Butt joints of cylinders of AISI 304L SS, each of dimension 150mm x 51mm x 4mm, are joined by GTAW process by using austenitic filler metal ER308L of 2.4mm in three different conditions (Number of pass, gas flow argon (L/min), current (A)) Table II.2. In addition, nitrogen purge used inside the cylinder depends of the pipe area to prevent oxidation of the welding ring (joint).

When developing an experimental protocol for the study of a physical phenomenon, it is important to identify factors and interactions that can influence the outcome of the tests. The result of a test is usually a measure of a variable called a response.

A design of experiments is a series of tests organized in advance, so as to determine in a minimum of tests and with a maximum of precision, the influence of multiple parameters on one or more responses. It can help in the design and industrialization of a process or product, as well as in solving complex optimization problems (adjustments) during its production. This method therefore fits perfectly into the quality approach.

The method consists in establishing a design of the experiment and then analyzing the effect of each of its operating parameters. The goal is to establish a protocol to guarantee the quality. A response by limiting the number of attempts. Concretely, this method identifies the combinations of parameters that reduce the effects of the causes of errors, without directly addressing them.

An experimental plan was put prior to conducting experiments and to allow us to study the influence of welding parameters on the stress corrosion process of the welded joint in AISI 304L stainless steel. In our study, we adopted the Factorial Experimental Design (FED). The steps of this method are as follows:

1. Formalize the problem;
2. Select the parameters set their modalities (level of parameter variations) and select their interactions;

3. Select the appropriate table;
4. Perform the tests from the assignment of factors to the response;
5. Analysis of Variance (ANOVA) study
6. Determine the contribution of each factor and their interaction.

Each parameter has two levels changed by using full Experimantal design (FED), the welding parameters chosen are: A: Welding current (A) [50-55]; B: Number of pass [1-2]; C: Argon flow (L/min) [3-10] (Table. II.2).

Table II.2. The input welding parameters and their ranges.

	Range and Level	
	Lower Limit (−1)	**Upper Limit (1)**
X_1: Number of pass	1	2
X_2: Gas flow Argon (L/min)	3	10
X_3: Welding current I (A)	50	55

Table II.3. Orthogonal table adopted in our study by FED

Experiences	Control Parameters		
	Number of pass A	Argon flow rate L/min B	Current Amp C
EXP 01	**-1**	**-1**	**-1**
EXP 02	**1**	**-1**	**-1**
EXP 03	**-1**	**1**	**-1**
EXP 04	**1**	**1**	**-1**
EXP 05	**-1**	**-1**	**1**
EXP 06	**1**	**-1**	**1**
EXP 07	**-1**	**1**	**1**
EXP 08	**1**	**1**	**1**

The FED is applied between low and high levels: the low level is indicated by a negative (-1) symbol and the high level indicated by appositive (+1) symbol. Design matrix is developed from the notation of **Table 2**. The experimental range and levels of independent

variables for specimens are given in **Table 3**. Six responses are analyzed: R_1 = Rp: resistance of polarization, R_2 = σ :residual stress (MPa), R_3 = B: peak width (°2θ), R_4 = F_{HAZ}: Average Ferrite content in HAZ (%), R_5 = F_{FZ}: Average Ferrite content in FZ (%) and R_6 = E_{corr}: corrosion potential (mV). The interaction effects are calculated by multiplying the parent terms.

II.3. Sample collection and sizing

Butt welded joints being done under varied input parameters, visual inspection of all welded specimens has been made. After visual inspections the specimens have been prepared from the welded joints, the samples were cold cut by an automatic saw at the machine shop of the company GTP/Z (Arzew, Sonatrach, Oran). In our study, we adopted a sample taking in the direction of welding by cuts far away with 20 mm distance of the weld joint as it is illustrated in the (Figure II.2).

The cutting is carried out under spraying a mixture of water and oil to prevent sample heating, ensuring a clean and shiny cut without altering the microstructure of the cut sample. These precautions were taken in order to provide identical samples which have kept the characteristics of the initial material for better reproducibility of the results.

Figure II.2. Cold cutting of samples by an automatic saw

To carry out the electrochemical tests separately, the electrodes of each material, with a working surface of 35mm × 20mm×4mm were cold cut using a micro-saw-automatic under continuous lubrication, in three specimens relating to the microstructure (base metal, heat affected zone and center of the weld). (Figure II.3 and Figure II.4).

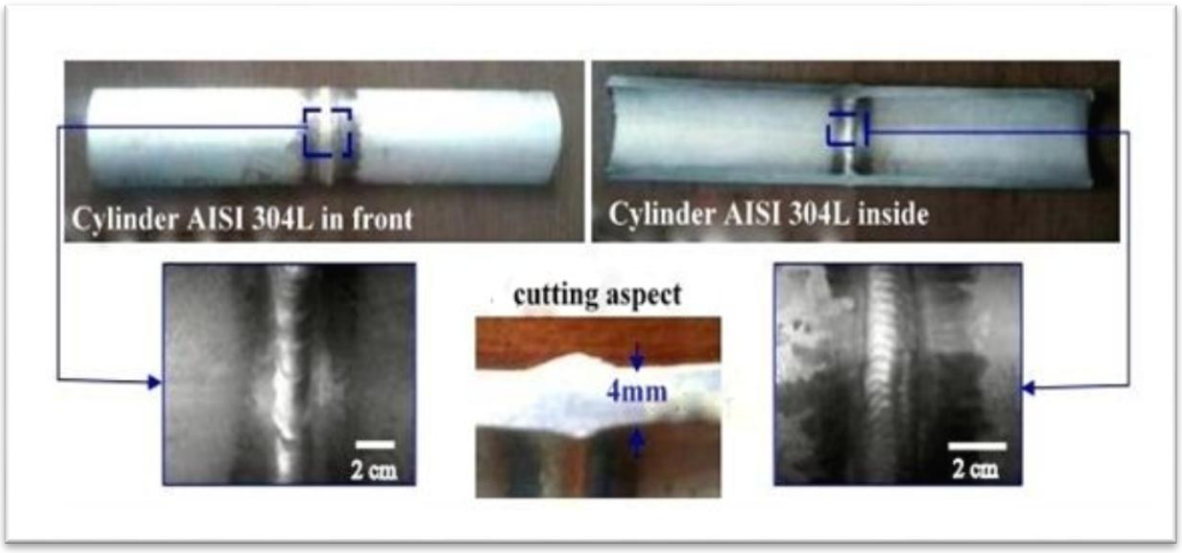

Figure II.3. AISI 304L sample collection cylinder and cut appearance[66].

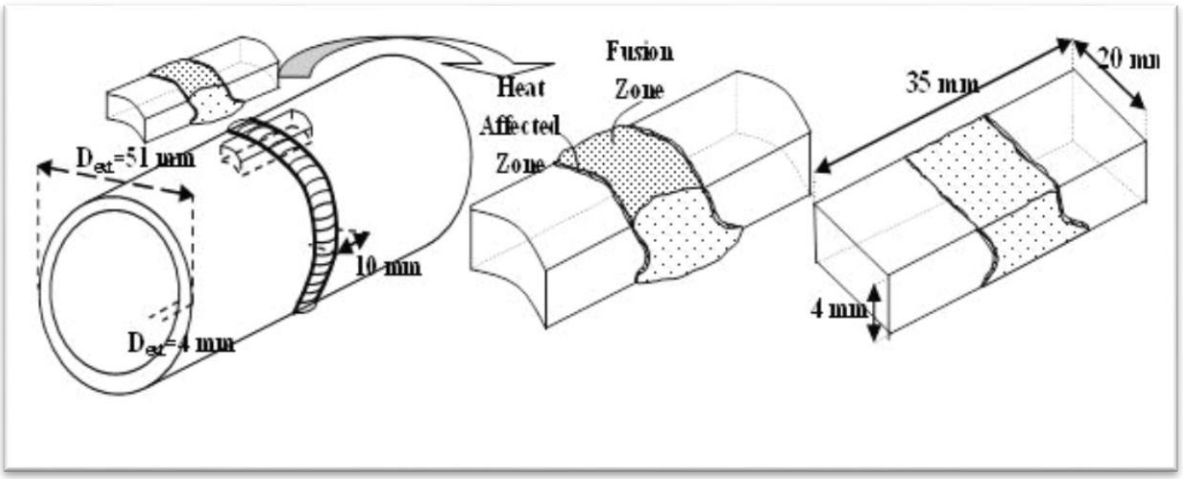

Figure II.4. Schematic illustration of the welded specimen.

II.4. Mechanical Characterization

In Table II.3 and II.4, we present the different mechanical properties of base metals before welding, taken from the technical data sheet for the material. Knowledge of these characteristic is important for the approved welder of the GTP/Z in order to validate the grade of the steel intended for welding as well as for the choice of welding parameters.

Table II.3. Mechanical characteristics of AISI 304L before welding

Dimension	**Re (N/mm^2) 20° C**	**Rm (N/mm^2)**		**Hardness Brinell HB**	**Elongation A%**	**Resilience At -50 ° C KV(J)**
mm	Min	Min	Max	Max	Min	Min
≤ 160	310	500	700	215	50	100

Table II.4. Mechanical characteristics of AISI 308L filler metal before welding

Dimension	**Re (N/mm^2)**	**Rm (N/mm^2)**		**Hardness Brinell HB**	**Elongation A%**	**Resilience At -50 ° C KV(J)**
mm	Min	Min	Max	Max	Min	Min
2.4	420	570	700	215	45	80

II.4.1. Vickers hardness test

The simplest method to obtain information on the point resistance properties of the metal constituting the weld is hardness. Hardness has often been related to elastic limit and breaking load.

The Vickers hardness test method consists of indenting the test material with a diamond indenter, in the form of a right pyramid with a square base and an angle of 136 degrees between opposite faces subjected to a load of 1 to 100 kgf. The full load is normally applied for 10 to 15 seconds. The two diagonals of the indentation left in the surface of the material after removal of the load are measured using a microscope and their average calculated. The area of the sloping surface of the indentation is calculated. The Vickers hardness is the quotient obtained by dividing the kgf load by the square mm area of indentation (Figure II.5).

The value of Vickers hardness is estimated by the following relation

$$H_V = \frac{2F * Sin\frac{136}{2}}{(d1+d2)^2} \quad \text{..... (II.1)}$$

$$H_V = 1.854 * \frac{F}{(d1+d2)^2} \quad \text{..... (II.2)}$$

With:

F: the load applied during the test (10Kgf);

d_1 and d_2: the diagonals of the imprint observed on the measurement surface.

H_V: Vickers hardness

On the microdurometer used in our study, the hardness value is converted from the measurement results of the diagonals (d_1 and d_2) and then displayed on an LCD screen. The hardness imprints were made in the different microstructural areas of the materials studied as illustrated in (figure II.6). At least five tests in each zone are carried out randomly and the final result is estimated by the mean value of hardness (H_{Vavg}).

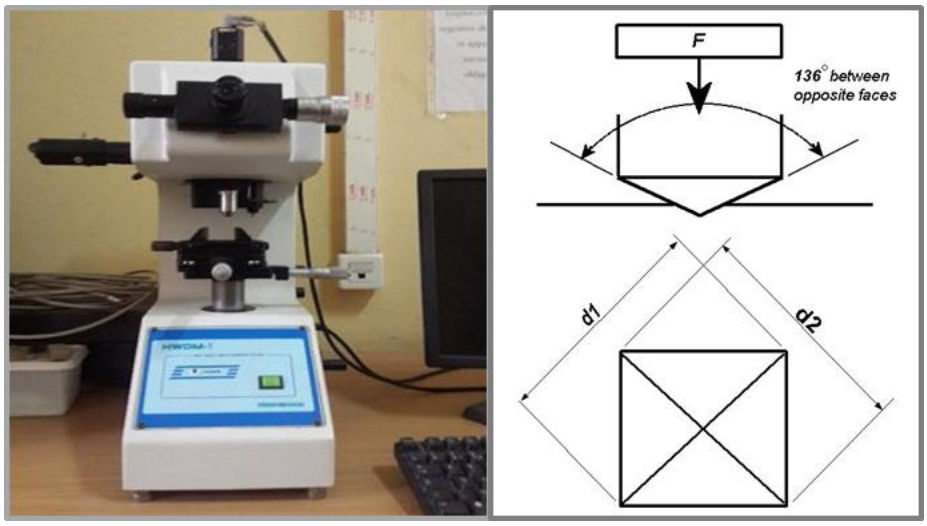

Figure II.5. Microdurometer type HWDM1.

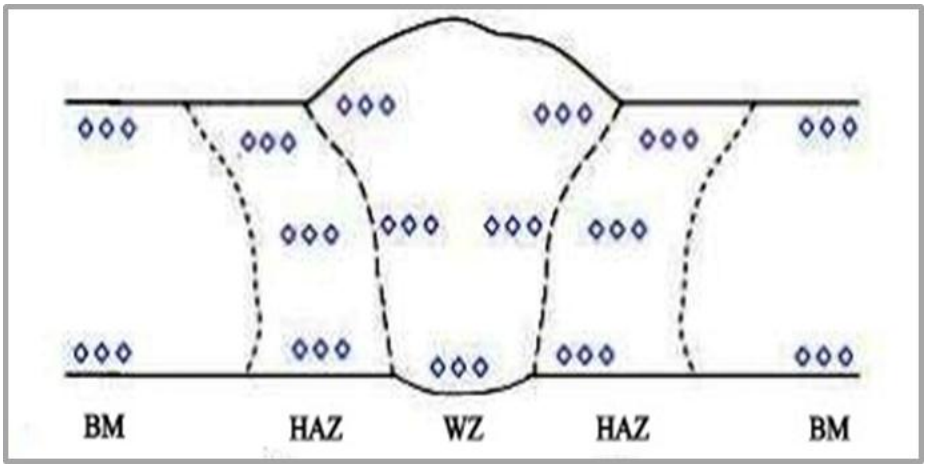

Figure II.6. Making Vickers hardness impressions on welding joint

II.4.2. Residual stress measurement using XRD

Residual stresses (RS) are internal stresses present in the material after external loading forces have been removed. Manufacturing processes such as machining, casting, alloying, quenching, cutting and tooling can all contribute to a change in residual stress. Residual stress measurements are particularly useful for quality control purposes. Determining the distribution of residual stress is important because high residual stress can lead to premature catastrophic failure of a component. There is no direct method available to measure stresses: they are calculated or derived from a measured quantity such as elastic strain or displacement. X-ray diffraction is used to measure residual stress in a non-destructive manner. With this technique, the deformations of the atomic crystal lattice of the metal are measured, then the residual stresses are calculated from the strain measurements.

In x-ray diffraction residual stress measurement, the strain in the crystal lattice is measured, and the residual stress producing the strain is calculated, assuming a linear elastic distortion of the crystal lattice. Although the term stress measurement has come into common usage, stress is an extrinsic property that is not directly measurable. All methods of stress determination require measurement of some intrinsic property, such as strain or force, area and the calculation of the associated stress.

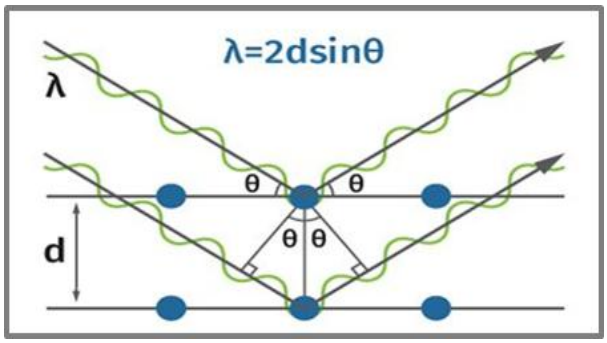

Figure II.7. Illustration of the Bragg's law which describes X-ray diffraction from crystal lattice planes[67].

In diffraction-based methods, the elastic strain is measured using Bragg's law and calculation of the stress is done with Hooke's law together with elastic modulus (E) and Poisson's ratio (v).Bragg's law describes X-ray diffraction from crystal lattice planes. In a stressed material, the wavelength of the X-ray (Λ) is known, the distance between atomic planes (d) is unknown and the diffractions are observed at angles θ. Stress causes small

changes in d and shift the diffraction angle. Bragg's law assumes incoming and diffracted waves to be in phase and undergoing constructive interference.

Residual stresses are determined from the diffraction data by calculating the strain from the diffraction peak positions. Any stress, including applied or residual stresses, induces a strain which corresponds to changes in lattice spacing. In practice, a metal powder with no stress is measured first to set the angular scale of the detectors for a certain material. Stress is then calculated by measuring lattice distance with multiple tilt angles and plotting the results as d vs. $\sin^2X$ graph, where d is the measured lattice spacing and X is the tilt angle.

The residual stresses can be determined from the slope of this d vs. $\sin^2X$ graph. Measurements are usually fast, lasting from seconds to few minutes. Irradiated area size affects the measurement time; using a larger collimator reduces the needed time to make measurements.

Stress calculation is affected by material-based parameters such as differences in lattice parameters, precipitations, interstitial occupation, and micro stresses. In a poly-crystalline structure with disordered crystals at the grain boundaries, precipitations and lattice defects, the diffraction line widens and forms a Gaussian-like peak. The width of the peak is measured as Full Width at Half Maximum (FWHM) which illustrates micro stresses and/or hardness and plastic deformation; typically, value increases with increasing hardness.

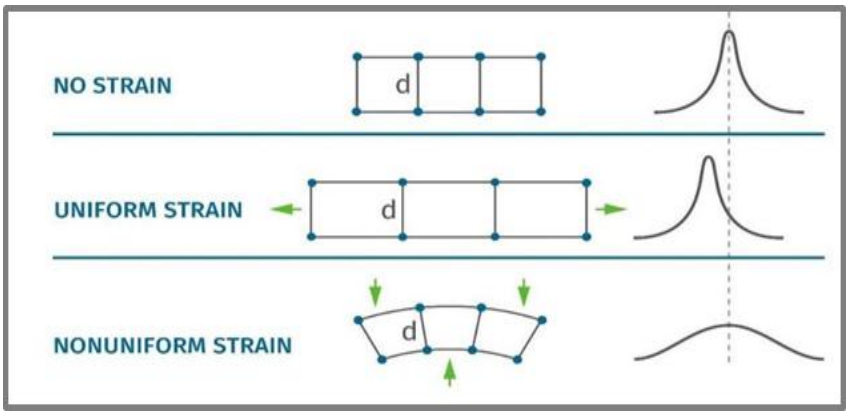

Figure II.8. Uniform strain shifts the diffraction peak. Non-uniform strain can alter both the peak shape and position

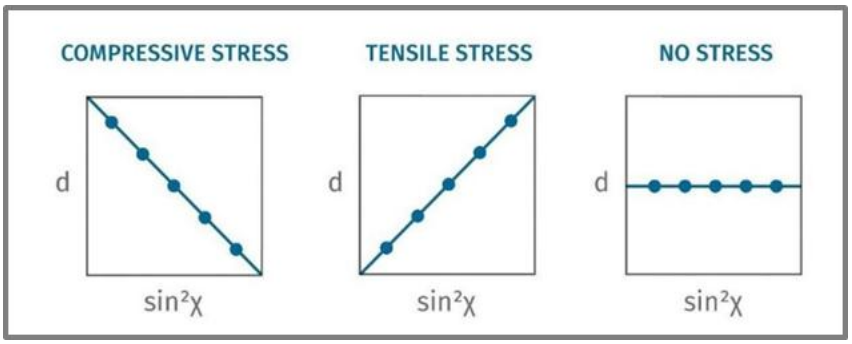

Figure II.9. Residual stresses are determined from the diffraction data by calculating the strain from the diffraction peak positions

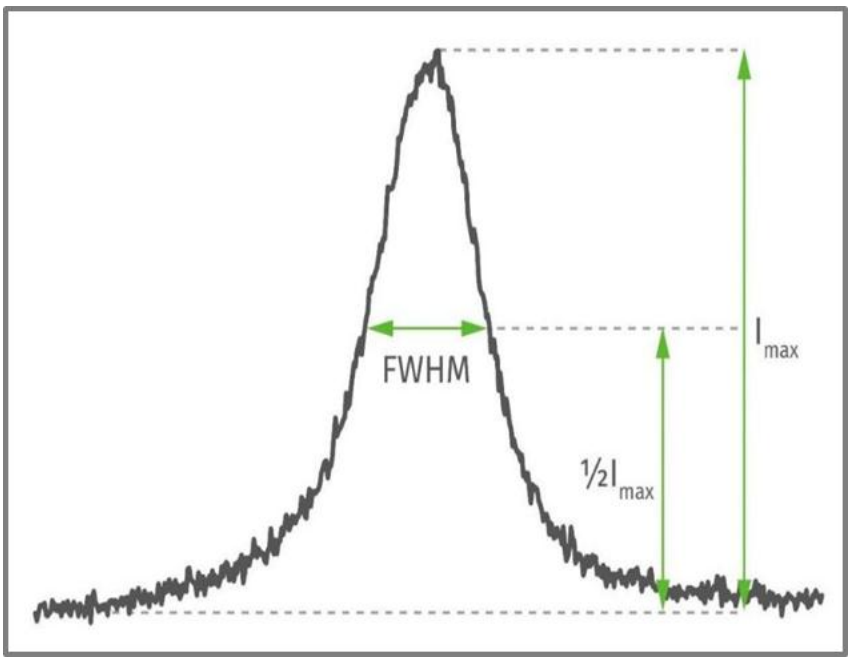

Figure II.10. The width of the diffracted peak is affected by micro stresses and imperfections in the crystal structure (i.e. dislocations, plastic deformation, etc.)

- **Macroscopic stresses** or macro-stresses, which extend over distances that are large relative to the grain size of the material, are of general interest in design and failure analysis. Macro-stresses are tensor quantities, with magnitudes varying with direction at a single point in a body. The macro-stress for a given location and direction is determined by measuring the strain in that direction at a single point. When macro-stresses are determined in at least three known directions, and a condition of plane stress is assumed, the three stresses can be combined using Mohr's circle for stress to

determine the maximum and minimum residual stresses, the maximum shear stress, and their orientation relative to a reference direction. Macro-stresses strain many crystals uniformly in the surface. This uniform distortion of the crystal lattice shifts the angular position of the diffraction peak selected for residual stress measurement.

- **Microscopic stresses**, or micro-stresses, are scalar properties of the sample, such as percent of cold work or hardness that are without direction and result from imperfections in the crystal lattice. Micro-stresses are associated with strains within the crystal lattice that traverse distances on the order of or less than the dimensions of the crystals. Micro-stresses vary from point to point within the crystal lattice, altering the lattice spacing and broadening the diffraction peak. Macro-stresses and micro-stresses can be determined separately from the diffraction peak position and breadth.

Figure II.11 shows the diffraction of a monochromatic beam of x-rays at a high diffraction angle (2θ) from the surface of a stressed sample for two orientations of the sample relative to the x-ray beam. The angle ψ, defining the orientation of the sample surface, is the angle between the normal of the surface and the incident and diffracted beam bisector, which is also the angle between the normal to the diffracting lattice planes and the sample surface.

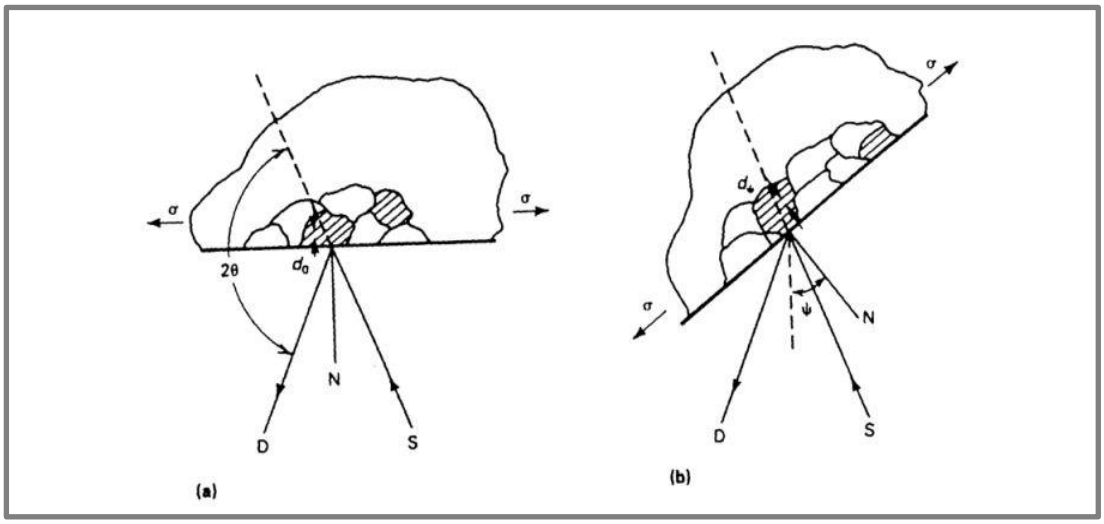

(a)ψ = 0. (b) ψ = ψ (sample rotated through some known angle ψ). D, x-ray detector: S, x-ray source; N, normal to the surface.

Figure II.11. Principles of x-ray diffraction stress measurement

Diffraction occurs at an angle 2θ, defined by Bragg's Law:

$$n\lambda = 2d \sin\theta \quad \text{.....(II.3)}$$

where *n* is an integer denoting the order of diffraction, λ is the x-ray wavelength, *d* is the lattice spacing of crystal planes, and θ is the diffraction angle. For the monochromatic x-rays produced by the metallic target of an x-ray tube, the wavelength is known to 1 part in 105.

Any change in the lattice spacing, *d*, results in a corresponding shift in the diffraction angle 2θ. Figure II. 11 (a) shows the sample in the ψ = 0 orientation. The presence of a tensile stress in the sample results in a Poisson's ratio contraction, reducing the lattice spacing and slightly increasing the diffraction angle, 2θ. If the sample is then rotated through some known angle ψ (Fig II.11 b), the tensile stress present in the surface increases the lattice spacing over the stress-free state and decreases 2θ. Measuring the change in the angular position of the diffraction peak for at least two orientations of the sample defined by the angle ψ enables calculation of the stress present in the sample surface lying in the plane of diffraction, which contains the incident and diffracted Xray beams.

To measure the stress in different directions at the same point, the sample is rotated about its surface normal to coincide the direction of interest with the diffraction plane. Because only the elastic strain changes the mean lattice spacing, only elastic strains are measured using x-ray diffraction for the determination of macro-stresses. When the elastic limit is exceeded, further strain results in dislocation motion, disruption of the crystal lattice, and the formation of micro-stresses, but no additional increase in macroscopic stress. Although residual stresses result from non-uniform plastic deformation, all residual macro-stresses remaining after deformation are necessarily elastic.

The residual stress determined using x-ray diffraction is the arithmetic average stress in a volume of material defined by the irradiated area, which may vary from square centimeters to square millimeters, and the depth of penetration of the x-ray beam. The linear absorption coefficient of the material for the radiation used governs the depth of penetration, which can vary considerably.

The choice of a diffraction peak selected for residual stress measurement impacts significantly on the precision of the method. The higher the diffraction angle, the greater the precision. Practical techniques generally require diffraction angles, 2θ, greater than 120°.

II.4.3.The XRD-sin2ψ technique

The XRD-sin2ψ technique calculates the residual stresses existing in the surface layer of polycrystalline materials by assuming a plane-stress state. The theory of the technique can be found in numerous literatures, Fig. 12 illustrates schematically the in-plane stress σϕ with

respect to the two principal stress components σ1 and σ2. When a X-ray beam hits the sample surface at an incident angle Ω, those grains, with their (hkl) lattice planes meeting the Bragg diffraction condition and having an off-axis angle ψ with respect to the sample surface normal, emit a diffraction X-ray beam at a diffraction angle 2θ. Then the d-spacing dϕψ of the (hkl) lattice plane is measured. The principal formula for the XRD-sin2ψ stress measurement can be written as:

$$\frac{d_{\phi\psi}-d_0}{d_0}=\left(\frac{1+\nu}{E}\right)\cdot\sigma_\phi\cdot\sin^2(\psi)-\left(\frac{\nu}{E}\right)\cdot(\sigma_1+\sigma_2) \qquad \text{.....(II.4)}$$

where E and ν stand for the Young's modulus and the Poisson's ratio normal to the (hkl) orientation of the material respectively, and d_0 the lattice spacing at stress-free condition. It should be pointed out that, the surface of a polycrystalline material contains large quantity of grains having different orientations and, more importantly, these grains exhibit an elastic anisotropy. In order to describe the deformation of the individual crystallites and hence the lattice spacing due to an in-plane stress state, a grain interaction model is needed [68]. It was reported that only in the rare case of a (001) or (111) textured film of cubic material the film is in plane elastic isotropic and no grain interaction model is needed [69]. In the present project we assume elastic isotropy in the individual crystallites and hence forgo the use of a grain interaction model.

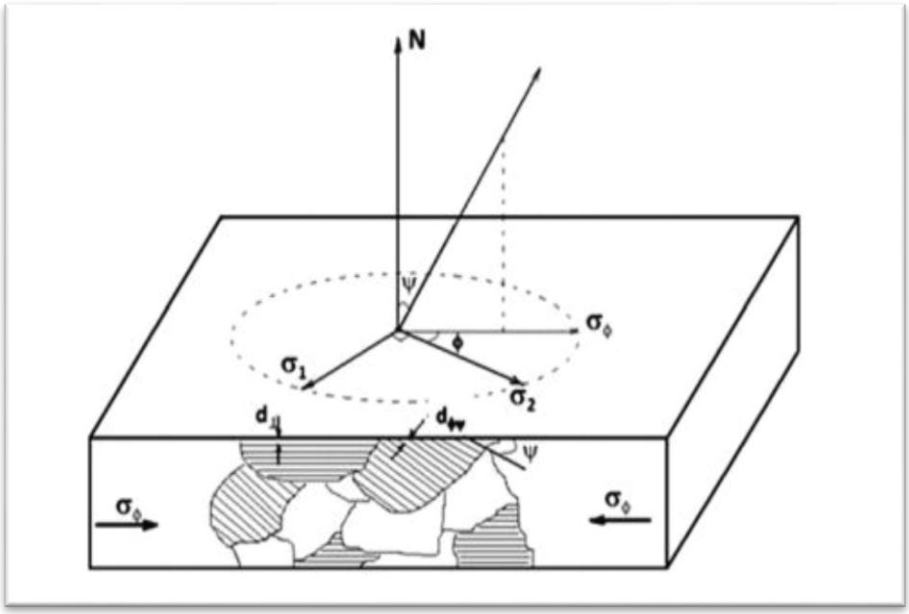

Figure II.12. A schematic diagram showing the set-up of the XRD-sin2ψ in-plane stress measurement [**70**].

Assuming $\boldsymbol{\sigma_\phi=\sigma_1=\sigma_2}$ when the in-plane stress σϕwhen the in-plane stress g the set-up of 5) can be re-written as:

$$d_{\phi\psi} = \left[\left(\frac{1+\nu}{E}\right)\cdot\sin^2(\psi)-\left(\frac{2\nu}{E}\right)\right]\cdot\sigma\cdot d_0 + d_0 \qquad \text{.....(II.5)}$$

Then Eq. (6) can be treated as a linear function Y=a·X+b by letting:

$$Y = d_{\phi\psi}=\frac{\lambda}{2\cdot\sin(\theta)};\ X=\left[\left(\frac{1+\nu}{E}\right)\cdot\sin^2(\psi)-\left(\frac{2\nu}{E}\right)\right] \qquad \text{.....(II.6)}$$

Therefore after making a series of XRD scans covering a known Bragg 2θ at fixed glancing angles Ωi (for i=1, 2, 3, etc.), the Bragg diffraction half angle θi can be measured in each diffraction peak and the associated off-axis angle ψi is calculated according to the relation ψi=θi - Ωi. The obtained θi and ψi are subsequently used to calculate the data group {Xi, Yi} according to Eq. (6), from which a linear regression processing of Eq. (5) is used to obtain the value of the constants a and b. Finally the in-plane stress σ, as well as the strainfree lattice d-spacing d_0, can be obtained from the relations d_0=b and σ=a/d_0 respectively.The method, a standard procedure in Japan and Germany, provides no significant improvement in precision over the two-angle technique if the two data points are selected at the extreme ends of the sin2ψ range. The primary advantage of the sin2ψ technique, considering the additional time required for data collection, is in establishing the linearity of *d* as a function of sin2ψ to demonstrate that x-ray diffraction residual stress measurement is possible on the sample of interest.

The effect of welding parameters on the longitudinal welding residual stresses [71-72] at the Heat Affected Zone of 304LSS was investigated using a Bruker type D8 Discover Xray diffractometer which was set up in Chi mode with a θ-2θ acquisition; (figure II.13). All the 6 reflection measurements were made using Cu-Kα monochromatic radiation, with a nickel filter, excited at 40 kV/40 mA. The stresses were measured perpendicular to the weld (≈ 1µm from weld) at the diffraction angle of 147.1° in 2θ corresponding to the lattice plane family {420}. The stresses were evaluated using the sin²ψ technique. The lattice spacing were determined for 12 ψ angles, ranging from 0° to 66° with stress oscillation of 6° to minimize grain size effects. After removal of a linear background, the diffraction peaks were fitted by a pseudo-Voigt function.

Table II. 5 lists recommended diffraction techniques for 304L SS. The relative sensitivity is shown by the value of K45, the magnitude of the stress necessary to cause an apparent shift in diffraction-peak position of 1° for a 45°ψ tilt. As K45 increases, sensitivity decreases.

Table II.5. Recommended diffraction techniques, x-ray elastic constants, and bulk values for 304L SS

Alloy	Radiation	Lattice plane, *(hkl)*	Angle (2θ), degree	Elastic constants(a) (E/1 = v) GPa (10^6 psi) *(hkl)*	Bulk	Bulk Error %	K_{45}(b) MPa	K_{45}(b) Ksi	cm $^{-1}$	Linear absorption Coefficient (μ) in.$^{-1}$
304L	Cu Kα	(420)	147.0	157.2 ± 2.8 (22.8 ± 0.4)	151.0 (21.9)	-3.9	814	118.0	2096	5321

(a) Constants determined from four-point bending tests. (b) K45 is the magnitude of the stress necessary to cause an apparent shift in diffraction-peak position of 1° for 45° angle tilt.

Figure II. 13. Bruker type D8 Discover XRD

II.5. Metallurgical characterization methods

The purpose of metallographic characterization is to observe the material at a microscopic scale; it makes it possible to identify the homogeneous or heterogeneous metallographic structure [71-73] of a cross section of a part.

II.5.1. Metallographic preparation

After cutting according to the procedure described above, the different samples underwent a succession of following metallographic preparation steps:

- Embedding the samples in a cold epoxy resin; The surface to be examined is then dressed and polished with abrasive papers whose grains have a decreasing fineness (N°.240 to N°.2400) on a STRUERES ROTOPOL-35 type polisher (Figure II.14).For better identification of transformation zones and better measurement precision. Polishing with diamond paste to 1µm is completed until a mirror appearance is obtained. Selective etching, chemical or electrolytic, to reveal the microstructure by means of a chemical reagent appropriate to the grade of stainless steel.

Figure II.14. Metallographic preparation of the specimens; (a) STRUERES ROTOPOL-35 polisher, (b) specimen after polishing.

II.5.2. Attack reagents for microstructural observation

The choice of chemical attack reagent depends on the metallurgical state such as the nature of the phases present, the grain size and the presence of precipitates. To study the microstructure of the bead, mechanical polishing is followed by an electrochemical attack with kalling2 (100 ml HCl (32%), 100 ml ethanol (96%) and 5g of $CuCl_2$) for 10 to 20 seconds (Figure II.15). The measurements of the different aspects of the cord were carried out using an optical microscope.

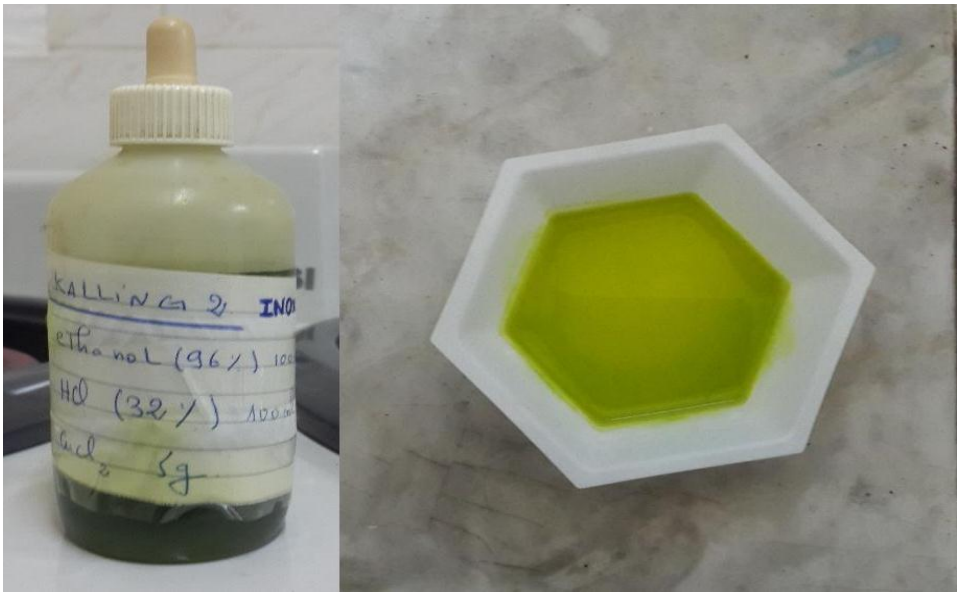

Figure II.15. Kalling2 chemical attack solution

II.5.3. Realisation of micrographs by optical microscopy

The optical microscope used in this study is Zeiss- primo-star type (Figure II.16); it allows the observation of samples with magnifications of 20 to 100 times. This microscope is equipped with a camera, a display set and image acquisition. Observing the surfaces after each treatment allows us to obtain information on the morphology and the thickness of the oxide layer formed on the substrate.

Figure II.16. Zeiss- primo-star optical microscope.

The goal of image analysis is to extract information from digital photographs in a quantitative and automatic manner. The advantage of optical microscopy image analysis is to make measurements on objects of interest such as grain size, the presence of a second phase

or corrosion defects. This requires two fundamental steps: first the extraction of the objects of the study and second the choice of parameters to be measured. An image analyzer is then necessary to transform the image into the "digital" format necessary for subsequent compilations according to the needs of the operator.

II.5.4. Observation under a scanning electron microscope and analysis of the chemical composition by EDS

Scanning electron microscopy is a powerful technique for observing surface topography. Its use in the analysis of steel microstructures has the advantage of obtaining resolutions significantly higher than those obtained by optical microscopy. This technique is based mainly on the detection of secondary electrons emerging from the surface under the impact of a beam of primary electrons which sweeps the surface to be observed. Quasi-parallel of electrons strongly accelerated by adjustable voltages from 0.1 to 30 kV, to focus it on the area to be examined and to sweep it gradually. The interaction between the electron beam and the sample gives rise to different types of emissions as shown in (figure II.17).

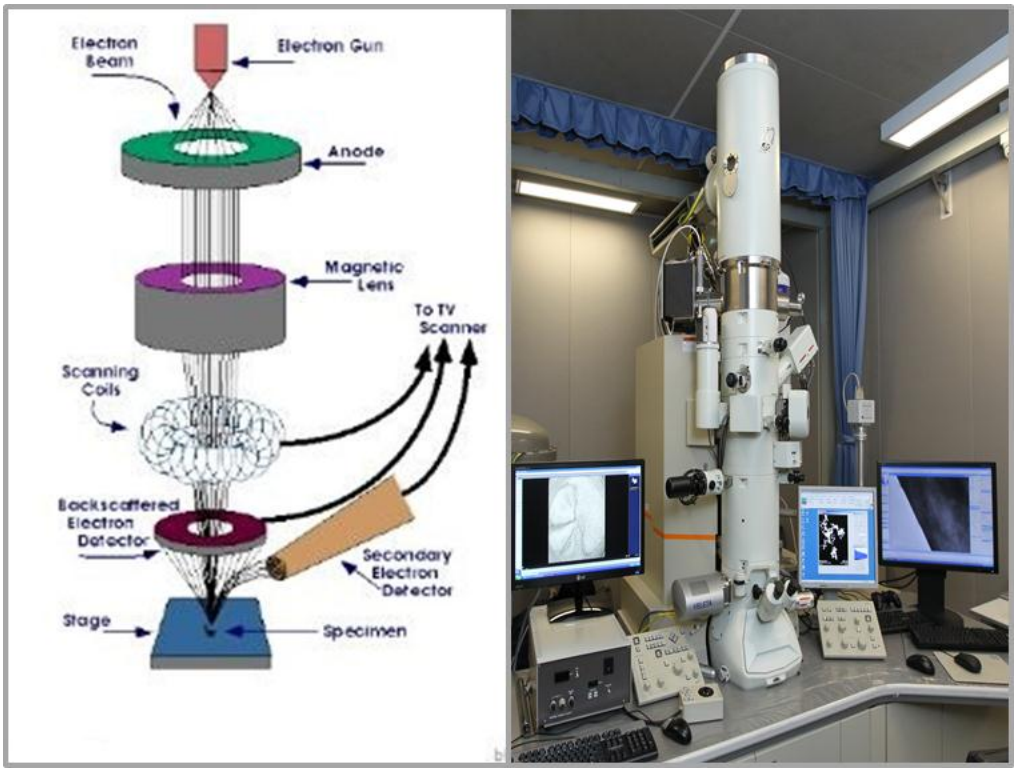

Figure II. 17. Schematic representation of the interaction between an incident electron beam and the surface of the sample to be examined by SEM

Specific electron detectors (secondary, backscattered, sometimes absorbed, etc.), supplemented by photon detectors, make it possible to collect the signals during the scanning of the surface and to form various meaningful images. For other tasks related to the analysis

of the chemical compositions of materials, the scanning electron microscope is equipped with an EDS system (energy dispersive spectrometry). This technique allows the spectrum of x-rays to be analyzed using the energy of the photons detected. For this, we have a semiconductor detector (a diode), subjected to a pre-polarization voltage.

When an X photon enters the detector, it generates defects (electron / hole pairs) that allow an electric current to flow. The more energy a photon has, the more defects it creates in the diode, so the stronger the generated pulse will be. The height of the pulse is proportional to the energy of the photon, so we can immediately know which photon it is. Then, just count the number of pulses of a given height to find out how many photons of a given energy the detector has received. The energy of the photons received is subsequently determined by the detector, thus obtaining diffracto-grams containing the spectra corresponding to the chemical elements detected, with an acceleration voltage of 25KV. For EDS analyzes, the ray count rate was estimated at $2x10^3$ counts/s.

II.5.5. Welded joint non-destructive testing methods

In our work, we opted for non-destructive testing techniques with a view to studying the surface and volume effect of corrosion tests in 3% NaCl. The techniques explained below were carried out at NDT and Quality Control Services at GTP / Z and are:

- Visual examination;
- Liquid penetrant testing;
- Ferritescopy;
- Radiography.

A. Visual control

Visual inspection consists of examining with the naked eye any changes in the surface finish of each sample as well as the condition of the test medium. The aim is to verify the criticality of corrosion damage as a function of time and to have a qualitative assessment of the corrosion resistance.

B. Liquid penetrant examination

Is one of the most popular Nondestructive Examination (NDE) methods in the industry. It is economical, versatile, and requires minimal training when compared to other NDE methods. Liquid penetrant exams check for material flaws open to the surface by flowing very thin liquid into the flaw and then drawing the liquid out with a chalk-like developer. Welds are the most common item inspected, but plate, bars, pipes, castings, and forgings are also commonly inspected using liquid penetrant examination.

Over the years, liquid penetrant examination has been called many names: penetrant testing (PT), liquid penetrant testing (LP), and dye penetrant testing (DP). The American Society for Nondestructive Testing (ASNT) uses the name liquid penetrant testing (PT). The *American Society of Mechanical Engineers Boiler and Pressure Vessel Code* (ASME B & PVC) and the *National Board Inspection Code* (NBIC) use the name liquid penetrant examination (PT). There are several advantages and disadvantages to using liquid penetrant examination.

1).Advantages

- High sensitivity to small surface discontinuities
- Easy inspection of parts with complex shapes
- Quick and inexpensive inspection of large areas and large volumes of parts/materials
- Few material limitations (metallic and nonmetallic, magnetic and nonmagnetic, and conductive and nonconductive can all be inspected)
- A visual representation of the flaw are indicated directly on the part surface
- Aerosol spray cans make the process portable, convenient, and inexpensive
- Indications can reveal relative size, shape, and depth of the flaw
- It is easy and requires minimal amount of training

2).Disadvantages

- Detects flaws only open to the surface
- Materials with porous surfaces cannot be examined using this process
- Only clean, smooth surfaces can be inspected. (Rust, dirt, paint, oil and grease must be removed.)
- Metal smearing from power wire brushing, shot blasting, or grit blasting must be removed prior to liquid penetrant examination
- Examiner must have direct access to surface being examined
- Surface finish and roughness can affect examination sensitivity. (It may be necessary to grind surfaces before PT.)
- Multiple process steps must be performed and controlled
- Post cleaning of parts and material is required, especially if welding is to be performed
- Proper handling and disposal of chemicals is required
- Fumes can be hazardous and flammable without proper ventilation

It is important to remember penetrant is a very thin liquid designed to seep into the smallest crack. Consequently, if an assembly has stitch welds or material not sealed by a weld, the penetrant will travel behind the welds and between layers of unfused material. Penetrant can be nearly impossible to remove from these areas. Trapped penetrant will cause defects in welds if further welding is done or will bleed out over time and contaminate paint and process fluids.

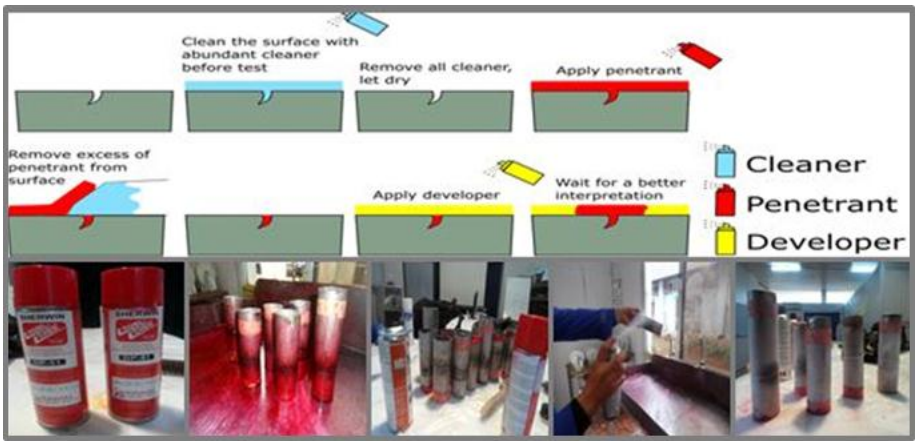

Figure II.18. Penetrant control steps

C. Ferritescopy

Ferrite testing, also referred to as a feritscope test, is a rapid non-destructive inspection method used to measure the amount of delta ferrite on austenitic stainless steel and duplex stainless steel materials. Ensuring proper ferrite content ensures corrosion resistance, durability and crack prevention. When ferrite levels exceed the maximum allowable content amount the stainless steel welds become susceptible to hot cracking.

The benefits to using ferrite testing is that this method leaves practically no markings on the test specimen. Additionally, it brings the convenience of a portable test machine which can be used to determine values very quickly, accurately and efficiently. In order to conduct a proper ferrite test, both a minimum and maximum material thickness is required for the test specimen. The results are then interpreted taking into consideration specifications and requirements as defined by the customer.

The control of the level of ferrite in our stainless steel is determined by using FMP30 Fischer type feritscope in different areas especially in the heat affected area HAZ, measured by the magnetic induction method. A magnetic field generated by a coil interacts with the magnetic components of the sample. Variations in the magnetic field induce a voltage proportional to the ferrite content in a second coil. This voltage is then evaluated.

Figure II. 19. Feritscope type Fischer FMP30

D. Radiographic testing

Industrial radiography is a modality of non-destructive testing that uses ionizing radiation to inspect materials and components with the objective of locating and quantifying defects and degradation in material properties that would lead to the failure of engineering structures.

Radiographic inspection by ionizing radiation X-ray or radioactive source, it possible to detect often very fine internal compactness defects (cracks, blisters, inclusions, lack of bond, lack of fusion) in the walls of metallic materials. Low wavelength electromagnetic rays are partially absorbed by the heterogeneities of the medium by passing through the wall of the irradiated material. The beam impresses the radiosensitive film according to the radiation transmitted through the controlled room to give rise to the radiographic image. The presence of a defect results in a variation in the absorption of the radiation emitted and therefore in a variation in the optical density of the film in line with the image of the defect.

The object to be examined is placed between a source of radiation and a photographic emulsion. As the blackening of the film depends on the amount of radiation received, we obtain a photograph which is the shadow of the object (variations in color correspond to variations in absorption). These rays propagate in a straight line; the formation of shadows is identical to that observed with the rays.

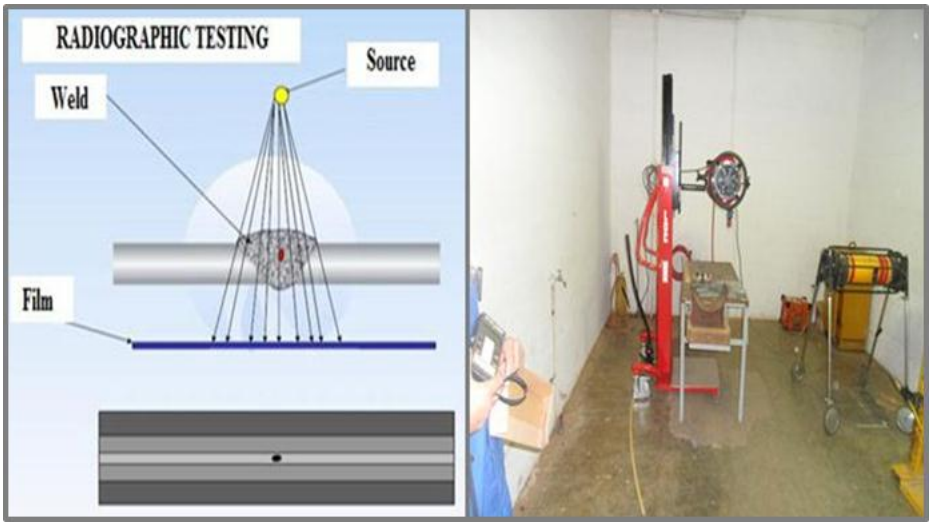

Figure II. 20. Radiography test

II.6. Electrochemical Characterization

After collection, the samples are cold-coated in an epoxy-based resin in which a coated conductive wire is firmly adhered to the sample. This is how our electrodes for corrosion testing are prepared. The test area of all samples is approximately 0.6 cm². Before each test, preparation of this surface is required, starting with a first mechanical polishing with emery papers (grain size index 240 to 2400) followed by a finishing polish to mirror state.

II.6.1. Assembly of the electrochemical cell

The electrochemical measurements of the 08 samples of the different weld metals were conducted in a conventional three-electrode cylindrical glass and thermostatic cell. A platinum disc was used as counter electrode, the reference electrode was a saturated calomel electrode (SCE) and the working electrode was Stainless steel of AISI 304L disc embedded in Araldite with surface area (0.6 cm^2) was the only surface in contact with corrosive solution. Measurements were performed using an autolab metrohm potentiostat/galvanostat (PGSTAT 302N) controlled with Nova 1.9 Software. Before recording the polarisation curves, the open circuit potential was stable within 50 min. The anodic and cathodic polarisation curves were recorded from -190 to 190 mV and potential scanning rate of 1mV s^{-1}. The 08 specimens of the different weld metals were determined from corrosion currents calculated by the Tafel extrapolation method and fitting the curve to the polarisation equation as well. Electrochemical impedance spectra (EIS) were obtained in the frequency range of 100 kHz to

10 mHz after 30 min of immersion. Each test was repeated two times to ensure reproducibility [74-77].

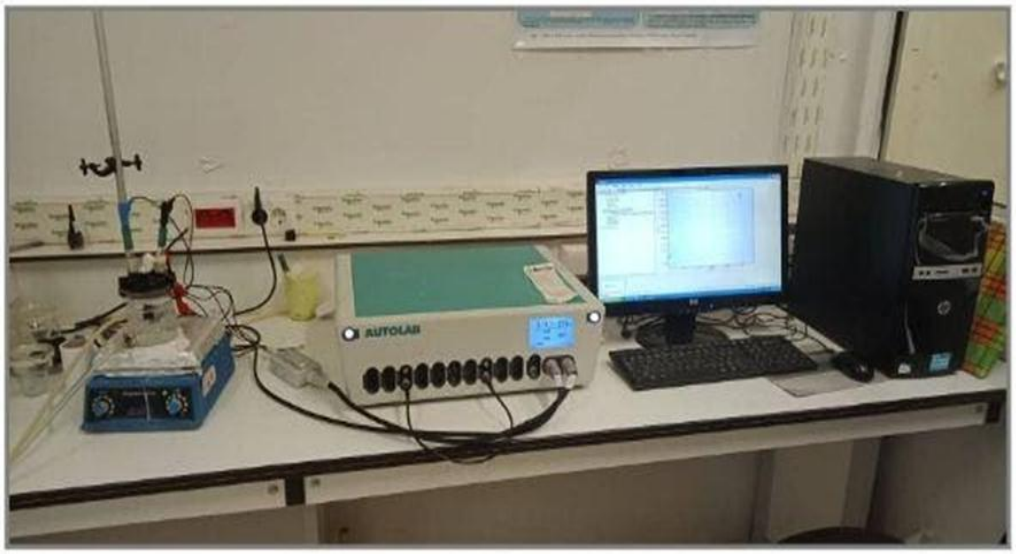

Figure II. 21. Device for the electrochemical tests of our study Autolab PGSTAT 302N model.

II.6.2. Potentiodynamic polarization tests

This method uses the phenomenon of electrochemical polarization [66] to determine corrosion current. These polarization curves are obtained either by the potentio-kinetic method or by the intension-kinetic method. These two methods require the use of an assembly comprising three electrodes: a working electrode (metallic), a reference electrode (saturated calomel ECS) and an auxiliary electrode (eg platinum).

The potentio-kinetic method involves applying a variable potential to the metal electrode relative to the reference electrode and measuring the intensity of the current flowing between the metal electrode and the auxiliary electrode. With the intension-kinetic method, it is the current that is imposed and the variation of sample potential is measured for each corresponding value. Thus, each of the anodic and cathodic reactions is represented by a polarization curve E = f (log i). These curves reflect the polarization mechanisms that govern these reactions. From these curves, the corrosion current can be deduced using Tafel's law or the Stern and Geary equation.

The corrosion current is determined by the linear polarization of the metal electrode. The polarization test establishes an imbalance at the surface of the sample by promoting either its anodic behavior or its cathodic behavior. So, we apply a potential other than the free potential and the metal is thus traversed by a non-zero overall current. The value of the

difference ΔE between the imposed potentials relative to the free potential is called "polarization". This method in the general case where the anodic reaction is the dissolution of the metal M in the n-valent state, the cathodic reaction is the reduction of the H^+ protons into molecular hydrogen.

Tafel's law expresses linearity between the overvoltage η, which can be defined as being a variation of the difference in metal-solution potential due to the effect of an electric current, and the logarithm of the current density (i) by the following relation:

$$\eta = a \pm b \log i \quad \text{(II.7)}$$

Where a and b represent Tafel's constants which can be positive or negative, depending on whether the overvoltage is anodic or cathodic, this equation is also expressed in the following form:

$$\eta_a = \beta_a \log i / icorr \quad \text{(II.8)}$$

$$\eta_c = \beta_c \log i / icorr \quad \text{(II.9)}$$

$$\eta = E_{applied} - Ecorr \quad \text{(II.10)}$$

Where ηa, ηc and βa and βc represent respectively the anodic and cathodic overvoltages and the anodic and cathodic Tafel slopes, i is a current and icorr is the corrosion current (μA / cm^2). Each curve is a line corresponding to the Tafel lines.

By extrapolating these lines, we obtain an intersection point corresponding to the value of the corrosion potential Ecorr and the corrosion current Icorr. This law is only valid for finite overvoltages, positive or negative, not close to zero.

In general, the linearity zone of the polarization curve can be observed for overvoltage values (positive or negative) between 50 mV and 300 mV, on either side of the corrosion potential.

On the semi-logarithmic plot, the polarization curve shows linear portions called “Tafel branches” corresponding to the charge transfer processes. Illustrates the extrapolation of the anodic (β_a) and cathodic (β_c) branches. When the anode component is affected by an inhibition process inside the pre-Tafel region, or by ohmic drop at high overvoltage, only the cathode branch extrapolated to Ecorr gives Icorr.The current corrosion rate Icorr is therefore obtained by the intersection of the Tafel lines and the vertical plotted at the value of Ecorr.

By extrapolating these lines, we obtain an intersection point corresponding to the value of the corrosion potential Ecorr and the corrosion current Icorr. This law is only valid for finite overvoltages, positive or negative, not close to zero.

In general, the linearity zone of the polarization curve can be observed for overvoltage values (positive or negative) between 50 mV and 300 mV, on either side of the corrosion potential.

On the semi-logarithmic plot, the polarization curve shows linear portions called "Tafel branches" corresponding to the charge transfer processes. Illustrates the extrapolation of the anodic (β_a) and cathodic (β_c) branches. When the anode component is affected by an inhibition process inside the pre-Tafel region, or by ohmic drop at high overvoltage, only the cathode branch extrapolated to Ecorr gives Icorr.The current corrosion rate Icorr is therefore obtained by the intersection of the Tafel lines and the vertical plotted at the value of Ecorr.

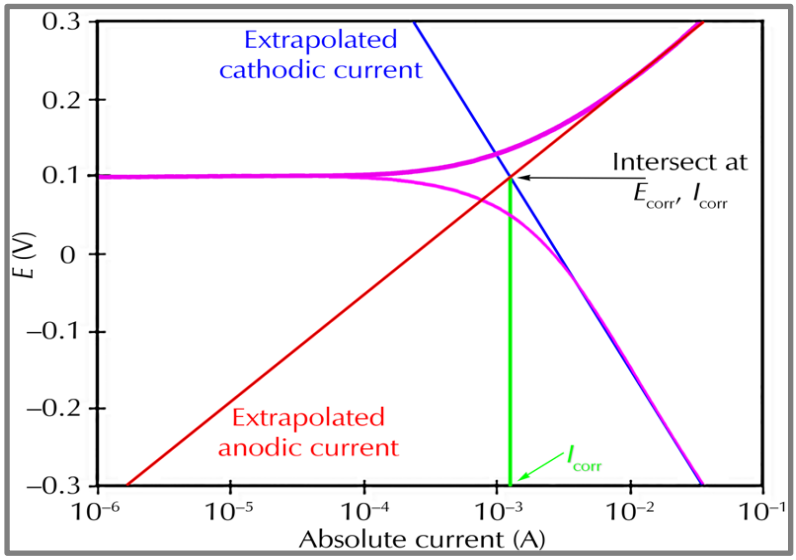

Figure II. 22. Extrapolation of Tafel lines

The polarization allows the calculation of the corrosion current from the polarization resistance Rp, slope of the curve I = f (E) in the vicinity of the point I = 0:

$$Rp = \left(\frac{dE}{dI}\right)_{I=0} \text{ ..... (II.11)}$$

Knowing the coefficients β_a and β_c [V per unit of log10 (i)] determined from the graph makes it possible to establish the relation (II.12), known as Stern and Geary:

$$Icorr = \frac{1}{Rp(\beta_a+\beta_c)} \text{ ..... (II.12)}$$

The constants B_a and B_c [V^{-1}] are related to the slopes of Tafel b_a and b_c such that**:**

$$B = \frac{\ln 10}{b} = \frac{2{,}30}{b} \text{ ..... (II.13)}$$

Equation (II.12) is also written:

$$Icorr = \frac{1}{2{,}30.Rp}\left(\frac{bc.ba}{bc+ba}\right) \text{..... (II.14)}$$

The corrosion rate is deduced from Faraday's law. It represents the rate of uniform corrosion of the metal and not the corrosion at the bottom of a pitting in the event of localized corrosion. V_{corr} is directly proportional to I_{corr} and it is written:

$$V_{corr} = I_{corr}\, M / S \cdot n \cdot F \cdot \rho \text{..... (II.15)}$$

M: the molar mass of steel (g / mol);

S: the area of the working electrode exposed to the solution (cm^2);

n: the valence number in the oxidation reaction;

F: Faraday's number (96,485.3329 s A / mol);

ρ: The density of steel (g / cm^3)

II.6.3. Electrochemical impedance spectroscopy

The measurement of electrochemical impedance is used to study the properties of the metal / solution interface. It provides information on electrochemical reactions, on the dielectric properties of interfaces as well as on transport processes.

This method consists in superimposing a sinusoidal signal of variable frequency and of low amplitude on the value of the voltage applied to the working electrode, then analyzing the current response of the system as a function of time and of the characteristics of the applied signal (frequency, amplitude, etc.); (Figure II.21). The different types of responses depending on the frequency make it possible to separate the elementary processes.

As shown in Figure II.21, a low amplitude sinusoidal voltage, V (t) = ΔV sin ωt, is superimposed on the voltage of the continuous polarization VS. As a result, a sinusoidal current of low amplitude, I (t) = ΔI sin (ωt + φ), is superimposed on the direct current I_S.

$$Z(\omega) = \frac{\Delta V}{\Delta I} \exp j\varphi \text{..... (II.16)}$$

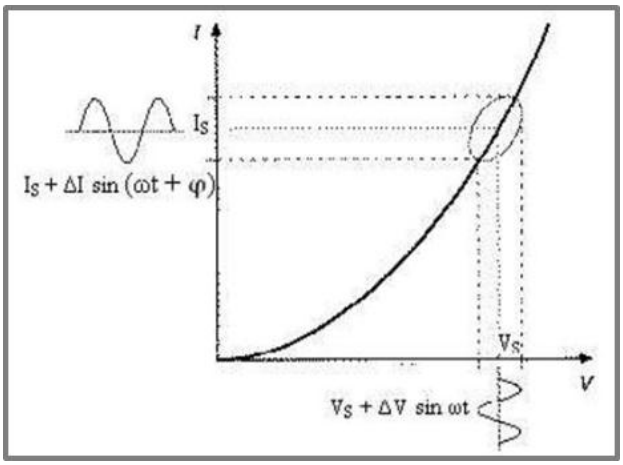

Figure II.23. Principle of electrochemical impedance spectroscopy

Z (ω) can thus be represented in polar coordinates by its modulus │Z│ and its phase φ or in Cartesian coordinates by its real part and its imaginary part (ReZ, Im Z):

We can also demonstrate that:

$$|Z|^2 = (Z_{re})^2 + (Z_{im})^2 \text{ and } \tan \varphi = \frac{Zim}{Zre} \quad \text{..... (II.17)}$$

In practice, the impedance measurements give rise to two types of graphical representation, namely the impedance spectra in Nyquist and Bode representation. The first plots the impedance by means of its Cartesian components in the complex plane where the negative imaginary part is carried above the real axis (Figure II.24b).

In this case, the frequency only appears indirectly on the diagram. The diagrams of Nyquist make it possible to determine the parameters Re (resistance of the electrolyte) and Rt (charge transfer resistance), and to calculate the value of DLC (double layer capacity).

In the second type of representation, the Bode diagram uses the polar components; the latter are reported as a function of the signal frequency (Figure II.24c). So, the Bode diagram consists in plotting the logarithm of the modulus and the phase shift angle of the impedance as a function of the logarithm of the frequency.

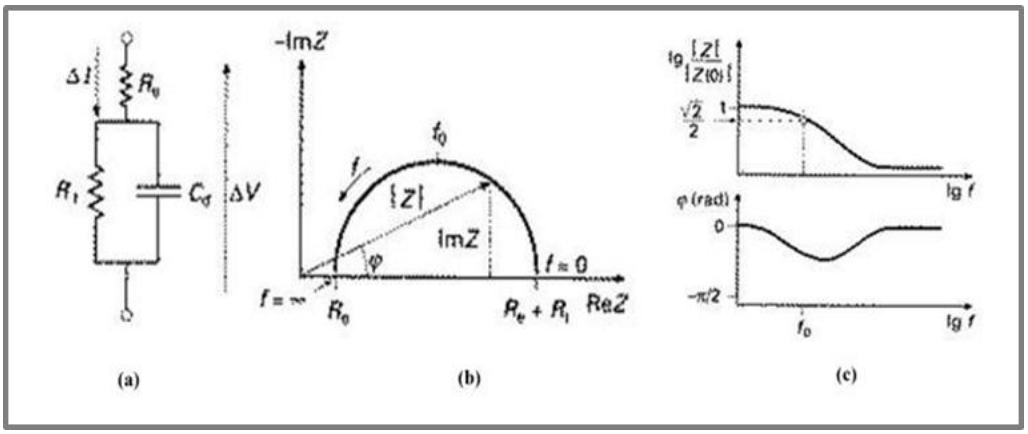

Figure II.24. Equivalent circuit and plot of the impedance of a cell Electrochemical, (a) Equivalent circuit, (b) plotted in the complex plane (Nyquist plane), (c) plotted in bode plane

The EIS tests of our study were carried out at open circuit potential after a pre-immersion of 60 minutes to stabilize its value. The VoltaMaster 4 interface is used to set the test conditions. A frequency range of 10 kHz to 1 MHz was used with an acquisition rate of 20 points per decade.

In particular when the time constants of the elementary steps are poorly decoupled, it is useful to model the impedance of an electrochemical system by that of an equivalent electrical circuit composed of simple elements: resistances, capacitors, inductors as well. Only constant phase elements (CPE) and Warburg elements (related to diffusion phenomena). They act as computational intermediaries intended to facilitate the obtaining of the kinetic constants. The frequency analysis of electrochemical impedance makes it possible to differentiate various elementary phenomena according to their characteristic frequency (or time constant).

a. Correspondence between a simple element of an equivalent circuit and electrochemical phenomena:

The circuit in Figure II.25 includes the elements that make it possible to determine the corrosion resistance of steel in contact with the electrolyte. It is composed of a resistance corresponding to that of the electrolyte Re, the capacity of the double layer Cd and the charge transfer resistance Rt.

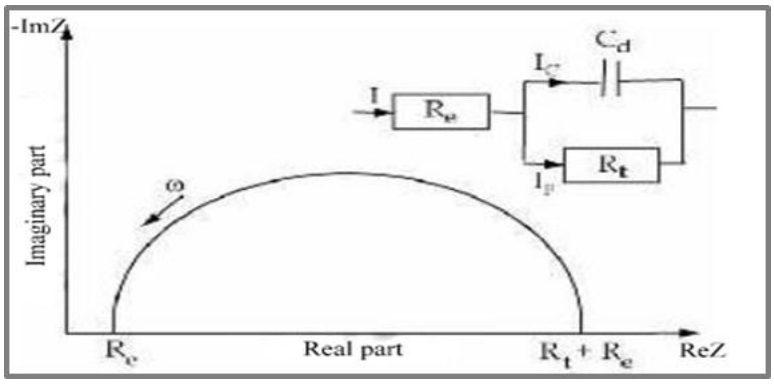

Figure II.25. Plot in the complex impedance plane of an electrochemical interface and equivalent circuit [78]

The electrochemical impedance reflects the electrochemical contribution of the system to the observed electrical response; it always includes a resistance to the transfer of ions and electrons involved in the dissolution, called charge transfer resistance Rt, in series with concentration resistors.

$$Z(\omega) = Z' - jZ'' \quad \text{..... (II.18)}$$

The total impedance of the circuit shown in Figure II.25 can be written in the following form:

$$[Z' - (Re+\frac{Rt}{2})]^2 + (Z'')^2 = (\frac{Rt}{2})^2 \quad \text{..... (II.19)}$$

b. Electrode adsorption

Reagents, reaction products and corrosion inhibitors can adsorb to the electrode. From an electrical point of view, the possibilities of recovery are described by capacitances. The phenomena of absorption are at the origin of the existence of a second semicircle at low frequencies (Figure II.26).

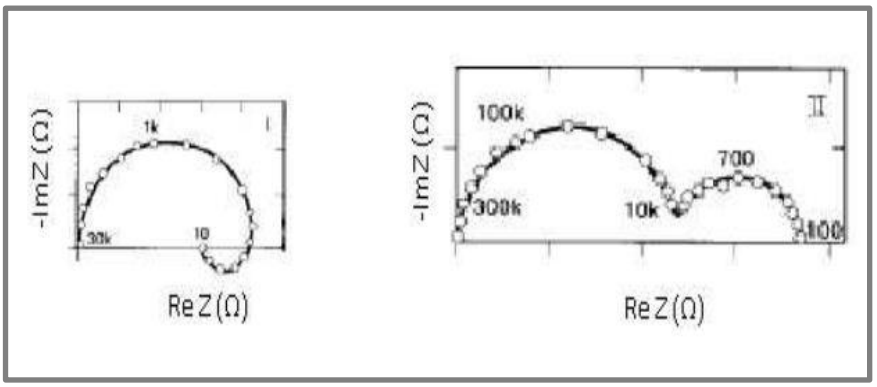

Figure II.26. Impedance diagram in the case of heterogeneous reactions with adsorption [79]

In corrosion processes, an intermediate stage of absorption of a species can take place at the electrode. This manifests itself on the impedance diagram, represented in the Nyquist plane, by an inductive loop (Figure II.27). It is modeled by a resistance R and an inductance L in parallel with the Randles circuit.

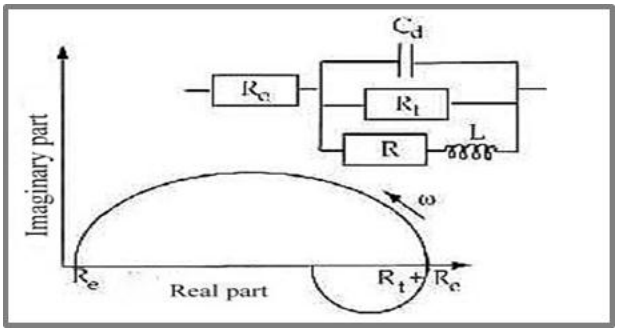

Figure II.27. Representation in the Nyquist plane, of the impedance **[8**0**]**

Electrochemical, of a species adsorbed on the surface of an electrode and equivalent electrical diagram. Slow processes, for example diffusion, are shown at low frequencies. Thus, an inductive loop present at low frequencies means that the adsorption process is limited by the diffusion.

c. Surface heterogeneities

In some cases, the modeling, by an equivalent electrical circuit, of the capacitive loop at high frequencies is difficult because of the presence of heterogeneities at the surface of the electrode. The reaction sites are then not uniformly distributed and the semicircle representing the charge transfer resistance and the capacity of the double layer in the Nyquist plane is flattened (Figure II.28).

The modeling of the behavior of the double layer by a capacitor becomes imperfect.

It is then necessary to add to this capacity a time constant, called constant phase element (CPE).

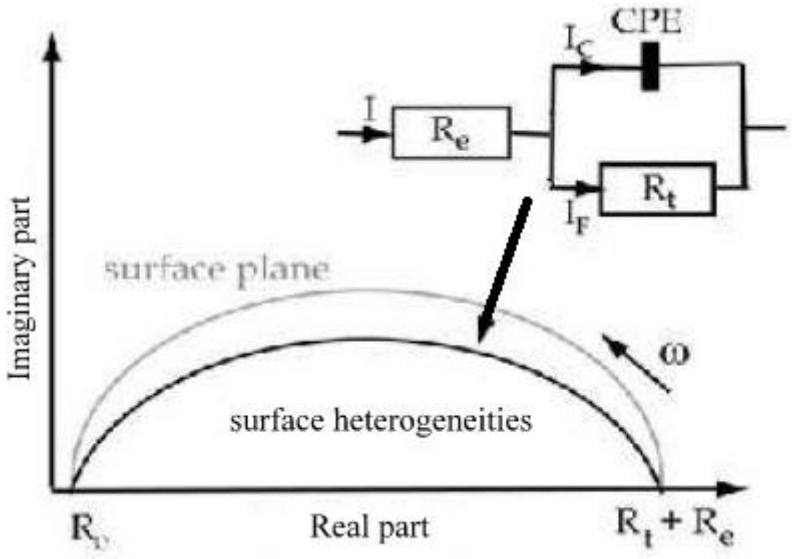

Figure II.28. Representation, in the Nyquist plane, of the electrochemical impedance of a heterogeneous surface electrode and equivalent electrical circuit **[8**1**]**

a. Diffusion

The diffusion of species in an electrolyte solution is a slow phenomenon, therefore measurable at low frequencies. For a sinusoidal disturbance of the potential, the diffusion phenomenon results in the intervention of a resistance to mass transfer and whose expression as a function of the frequency is:

$$Z\,\omega = (1 - j)\,\sigma\omega^{-1/2} \quad \text{..... (II.20)}$$

Where σ denotes the Warburg coefficient, note that the Warburg impedance remains the minimum diffusion impedance. In the complex plane, it is represented by a line 45 ° from the axes (FigureII.29)

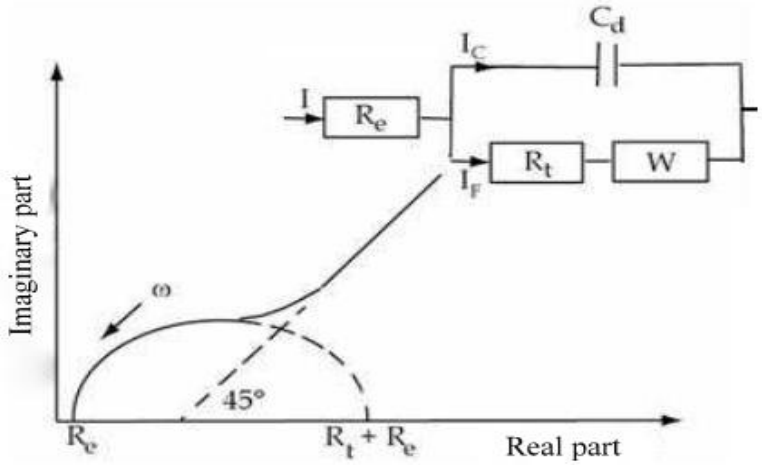

Figure II.29. Randles equivalent circuit impedance: case of a diffusion layer of infinite thickness.

Chapter 3

Effect of welding Parameters on mechanical properties

Chapter III gathers the experimental results obtained with mechanical and metallurgical characterization techniques as well as their interpretations.

First, the qualitative results of radiography and liquid penetration weld inspection are discussed. Then, the results related to the microstructural analysis by Optical Microscopy (OM), Scanning Electron Microscopy (SEM), ferrite content and X-Ray diffraction of welded joints of AISI 304L stainless steel were presented. . These analysis are done to identify the change in the morphology of welded zones as the function of the change in the weld parameters.

Mechanical proprieties as residual stress, metal mesh distortion and hardness of welded zones as the function of the change in the weld parameters are determined by X-ray diffraction and Vickers micro-hardness respectively.

In this Chapter the results of experimental Factorial Design (FED) used to study the welding process parameters effects on the stress corrosion at the Heat Affected Zone (HAZ) are presented. Three welding parameters were selected as input variables: Number of passes, gas flow (argon flow) and welding current. The main and the interaction effects of the welding parameters were studied and the correlations between the different responses were established.

III.1. Metallographic characterization results

The control or the metallographic analyzes make it possible to observe and assess the structures as well as the phases that make up the various materials (metals, ceramics, composites, etc.).

III.1.1. Macrographs of the welded joint

The macro-graphic examination of the welded joints in AISI304L reveals the geometry and the macrostructure of the two welds and makes it possible to distinguish the morphology of the weld. A metallographic section made perpendicular to the welding plane is necessary to characterize its various structural states. This structural evolution in the weld seam differs according to the grade of steel depending on the chemical composition and the rate of cooling.

Indeed, figure III.1 shows the weld made up of different zones: the first comprises the penetration passes (1) carried out by the TIG process then the tamping passes (2) which constitute a large volume of the weld and finally the last finishing pass (3).

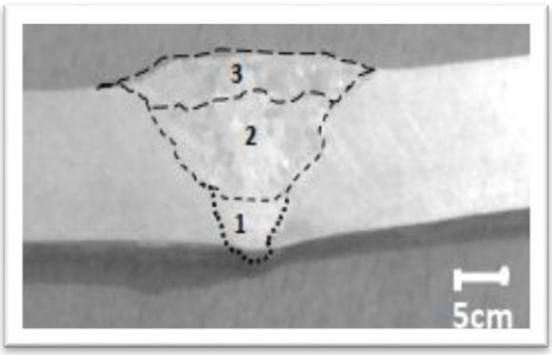

Figure III. 1. Macrograph and morphology of welded joint in AISI304L

III.1.2. Microscopic observation

The macro-structural analysis presents the micrographs examination under an optical microscope of different welding zones (figure III.2). In these figures, three zones are studied: the melted zone in the center of the weld, the HAZ (intermediate zone) beyond 2 mm from the fusion line and, finally, the base metal more than 10 mm from the axis of the weld.

Austenitic stainless steel AISI304L initially had a polygonal single-phase microstructure (Figure III.2) characterized by more or less regular crystallites. Some grains are twinned and appear to be crossed by panoply of lines corresponding to twin joints, most of which are straight and parallel and the thickness of which is variable.

The heat affected zone has a granular structure. In this area, we see the presence of large grains. This is due to significant overheating that occurred during the welding operation

where the temperature can exceed 1000 °C. The welding heat causes a heat treatment effect on the austenitic grains. The punctual heat input causes a heterogeneous microstructural gradient along the weld bead which affects the grain size distribution as well as the phase balance. This is also verified in the molten zone where the structure is two-phase composed of austenite and acicular ferrite.

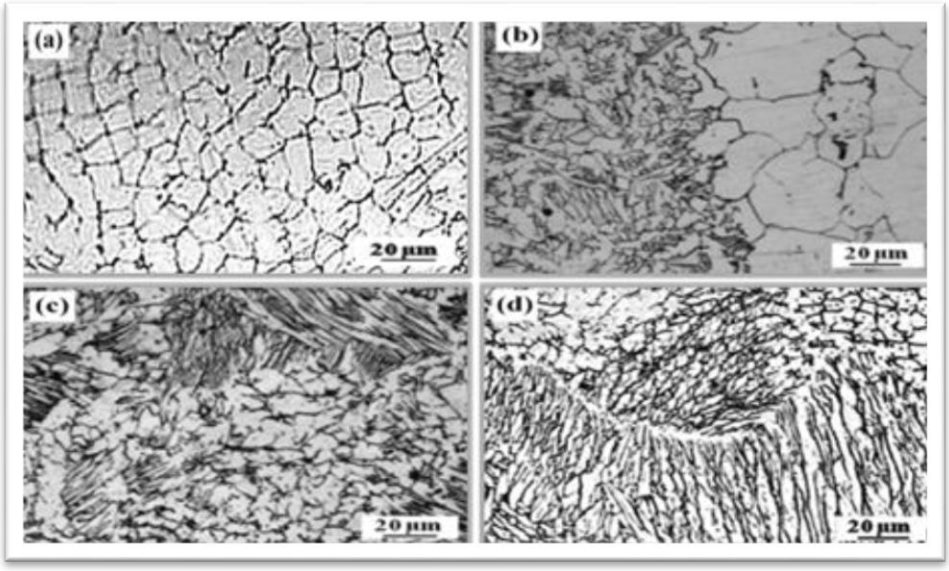

Figure III.2. Optical micrographs of (a) 304L SS base, (b) 304L SS weldment (HAZ) (c) and (d) 304L SS weldment (weld region).

The mean grain size G (grain size number) is determined by the plan-metric method. This is an image analysis method that involves drawing circular area on a micrograph and counting the number of grains per unit area, N_A. The average grain length is obtained by dividing the length of the line (based on the scale) by the number of grains. The value of N_A is calculated with:

$$N_A = (M^2/A)*(n_{inside}+[n_{intercepted}/2]) \quad \text{(III.1)}$$

where M is the magnification, A is the circular area, n_{inside} is the number of grains falling completely within the circle, and $n_{intercepted}$ is the number of grains intercepted by the circle's perimeter (refer to figure III.3). Then G can be calculated from the equation:

$$G = -3.322*\log[N_A] - 2.954 \quad \text{(III.2)}$$

The development of grain size calculation is shown below. Table III.1 gathers the mean values of different measurements carried out

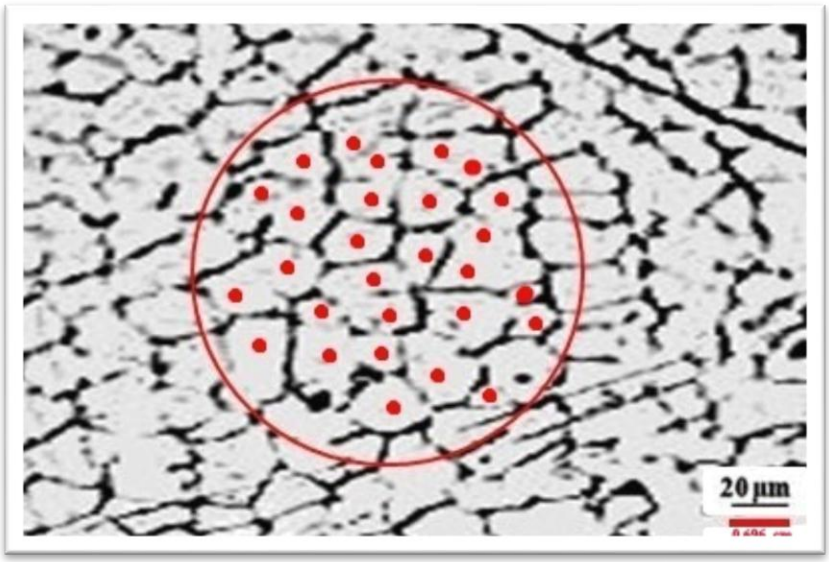

Figure III.3. Planimetric procedure

Draw circle with 6cm diam.

Calculate the internal grains which equal to 28 grains

Grains which intersect with circle was 16 grains

Total grains= internal grains+1/2(intersected grains) = 28+8= 36 grains

Now we find the magnification scale:

We measure the length of the scale on paper and it was 0.696 cm as you seen

Now: the scale can be known as= $\frac{\text{length of scale on paper in micrometer}}{\text{Scale value}} = \frac{0.696*10000}{20}$= 348

And the real circle diameter is= $\frac{5\text{ cm}}{348}$= 0.0144 cm or 144 µm

Real circle area= πr^2 = 3.14159*$(72)^2$ = 16286 μm^2

And the grain average area is: $\frac{\text{circle area}}{\text{Number of grain involved in the circle}} = \frac{16286}{36}$ = 452.39 μm^2

Finaly the grain size equal to the roof of its area: $\sqrt{452.39}$ = 21.27 µm

The density of grain per one square millimeter can be done by dividing one square millimeter (10^6 square micrometer) on the grain area

Then**,** grain Density **=** $\frac{1000000\frac{\mu m2}{mm2}}{452.39\frac{\mu m2}{grain}}$ **= 2210.48 grain/ mm^2**

Table III.1. Grain size average for three different area of welding metal AISI 304L

Welding Area	Grain size Avg (µm)
Parent metal (base metal)	35.18
HAZ	27.5
FZ	21.27

III.1.3. SEM analysis

Scanning electron microscopy is a fast imaging technique that provides high resolution and excellent depth of field.

An SEM microscope consists of an electron beam that scans the surface under study and a detector that collects signals resulting from the interaction between incident electrons and the surface. The signals collected include in particular secondary electrons, X-rays and backscattered electrons. In the case of a morphological study, the secondary electrons emitted are used for any purpose of creating the image. The reconstructed three-dimensional image makes it possible, for example, to examine a surface deposit or to visualize micro welds.

A-Base metal

Figure III.4 shows the microstructure of the base metal in the initial state obtained by SEM. The microstructure is composed of austenitic grains (Fig III.4a). The expansion of this last figure is presented in figure III.4b, and which shows the existence of macles and which were formed during the various previous thermo-mechanical treatments.

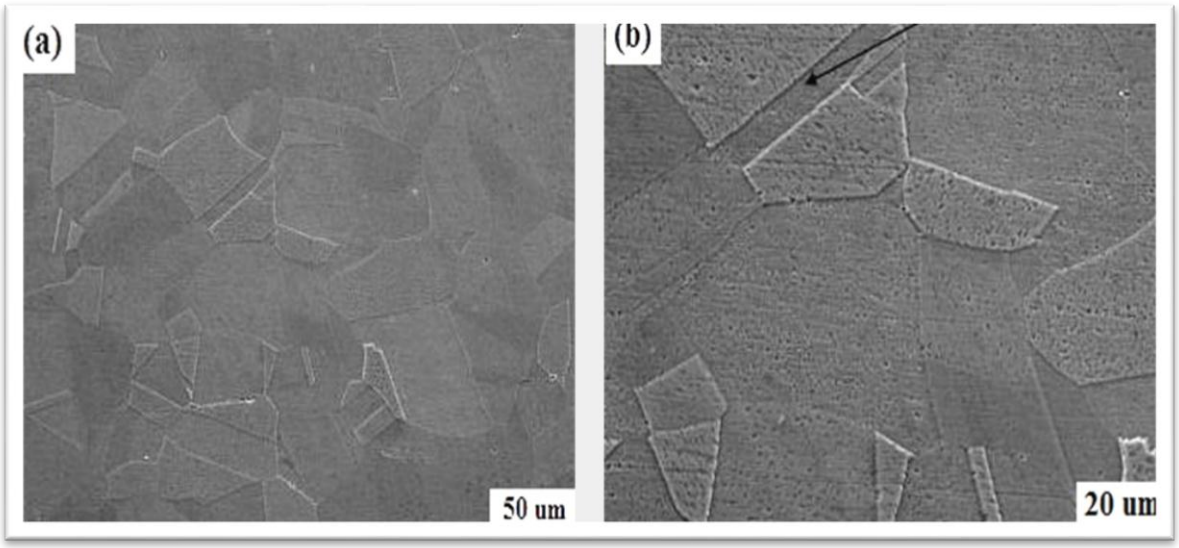

Figure III.4. Microstructure obtained by SEM of the AISI 304L base metal

B-Heat affected zone

Observation by optical microscopy of the heat affected zone reveals the formation of new large grains compared to the grains of the base metal. (Fig III.5.2a et 2b).

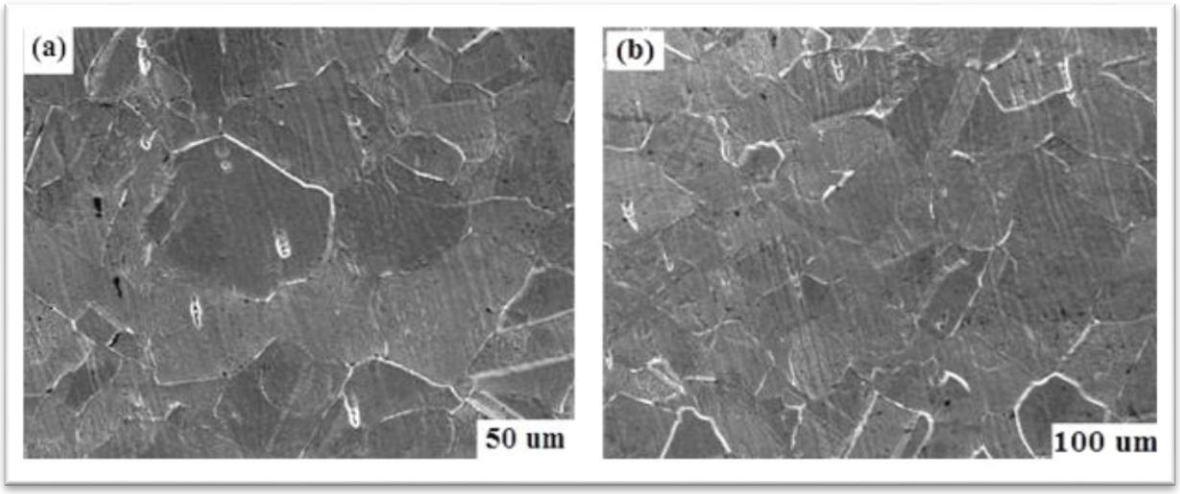

Figure III.5. Microstructure obtained by SEM of the heat affected zone of AISI 304L

The microstructure of the thermally affected zone is different from the base metal, it is generally composed of an austenite matrix and the δ-ferrite precipitates intercalated, because, under conditions of rapid non-equilibrium solidification, such as welding, the high rate of cooling will result in incomplete transformation $\gamma \rightarrow \delta$ and small amounts of δ-ferrite which inevitably remain in the microstructure at room temperature [82].

C-link area

The figures (III.6a and III.6b) clearly show the binding zone between the ZF and the HAZ, and which clearly illustrates the difference in granular morphology between the two zones.

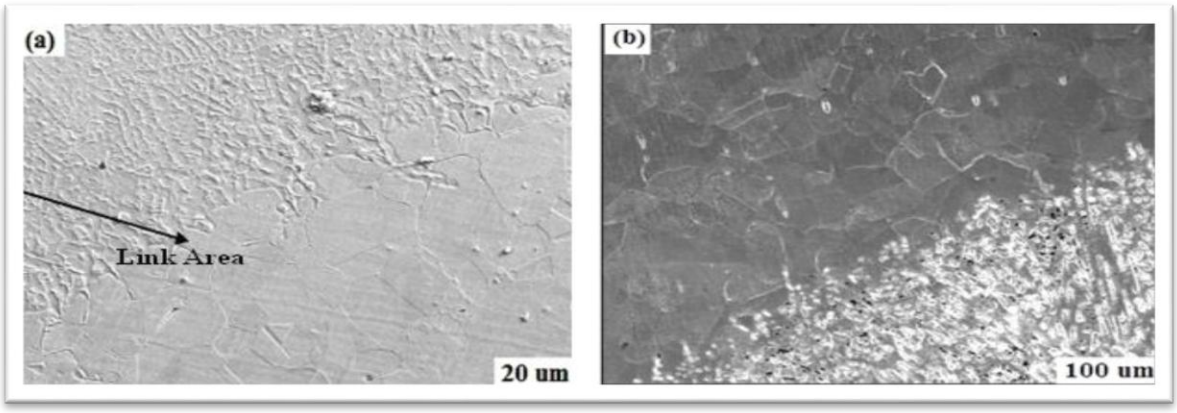

Figure III.6. Microstructure obtained by SEM of the link area of AISI 304L

D-Fusion zone

The figures (Fig III.7a and 7b) illustrate the microstructure of the molten zone (ZF) of stainless steel after welding. These microstructures at different scale show a totally different morphology from that of the base metal. This new microstructure is due to the mechanism and the solidification process which is rapid.

This new microstructure corresponds to a solidification structure. The microstructure of ZF is characterized by a lamellar morphology because it is due to rapid cooling rates after the welding operation.

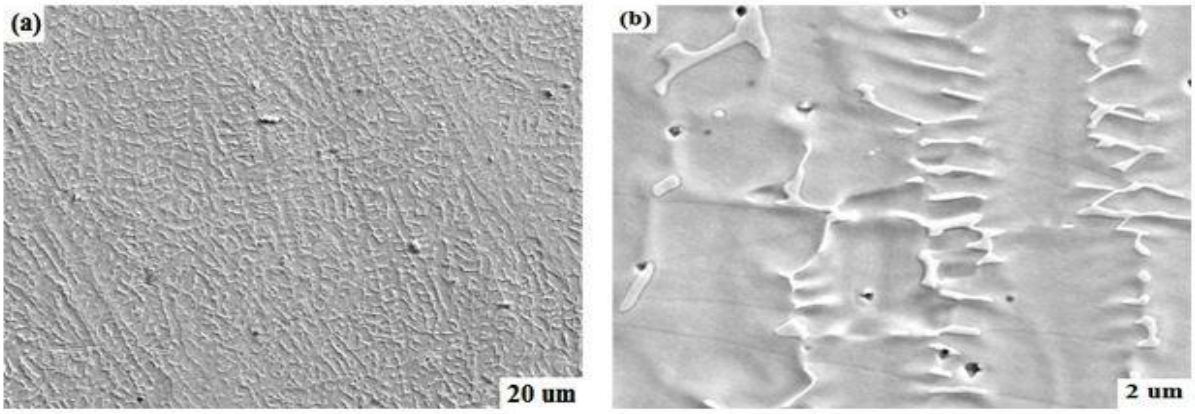

Figure III.7. Microstructure obtained by SEM of the fusion zone of AISI 304L

III.1.4. EDS analysis

The SEM observation of the surfaces of the samples of AISI304L allowed to obtain the facies of figure III.8, the rupture surface appears to be rough with the presence of cups of a few micro cracks. This is evidence of ductile failure, primarily in the parent metal. On the other hand, we notice the presence of fragile particles, such as precipitates. These particles, present in HAZ and ZF, are considered weld defects and can be areas of stress concentration.

A SEM / EDS analysis was performed on the broken AISI 304l sample. The results are presented on the diffract-grams in Figure III.8. Two tilts were made in two different places: on the fusion zone and 1mm from the weld. The comparison between the two spectra made it possible to highlight enrichment in Cr element could have been provided by the filler wire. The formation of carbides at the HAZ of AISI 304L could be confirmed with the presence of higher percentage of C, Cr as evident from the EDS analysis. Also the presence of carbon was observed to be in considerable amounts at the HAZ. This could be reasoned due to the carbon migration as reported by other researchers .

SEM/EDS analysis was performed on the various zones of the weldments to determine the presence of phases, as well as various elements across the weld to assess the structure - property correlations.

The chemical composition of ZF and the distribution of chemical elements are shown in Table and Figure III.8.b. It can be said that the main elements (Fe, C, Cr, Ni) exist in ZF and they are well distributed.

The HAZ of AISI 304L exhibited an agglomeration of delta ferrite stringers with coarse grains. These delta ferrite colonies act as a barrier for deformation mechanism. As the parent metal of AISI 304L offered lower hardness values, the tensile fracture is experienced at this zone.

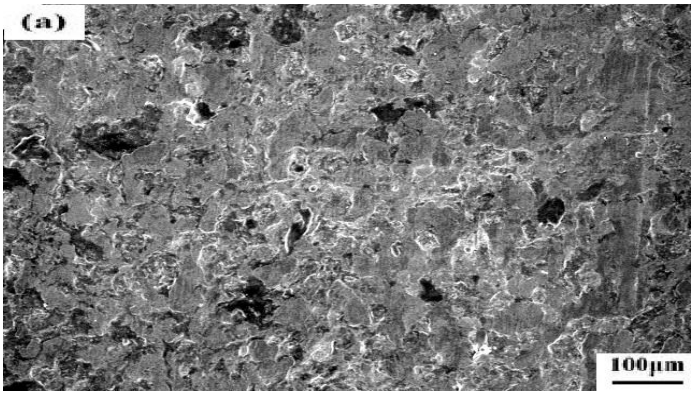

(a) SEM micrographs showing the surface morphologies of BM

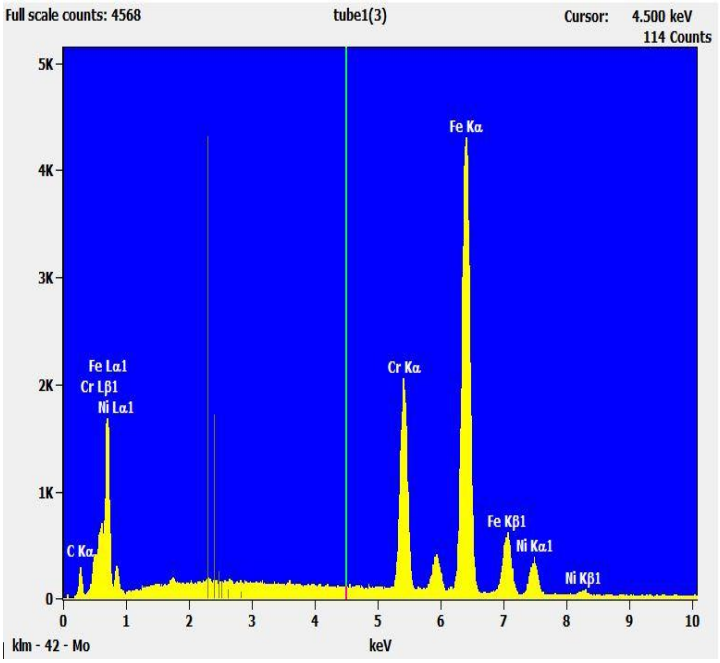

Element Line	Net Counts	Weight %
C K	1651	3.3
Cr K	30453	19.4
Fe K	69422	68.3
Ni K	6199	9.0
Total		100.0

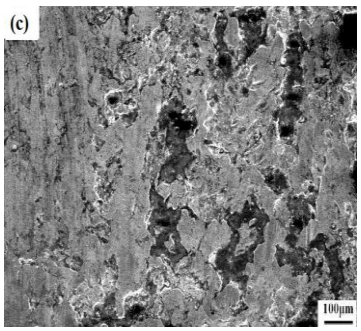

(c) EDS spectrum with chemical composition and location analysis on the (HAZ)

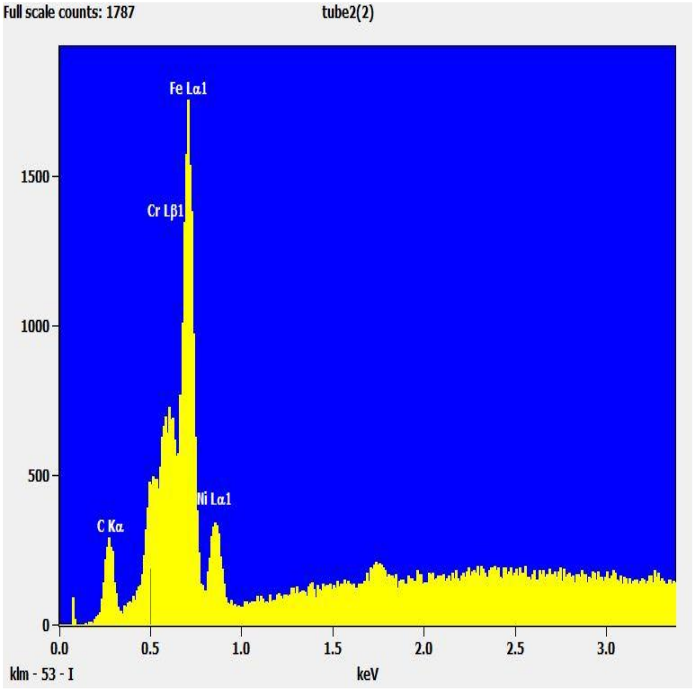

Element Line	Net Counts	Weight %
C K	1505	3.1
Cr K	29110	18.9
Fe K	70041	70.4
Ni K	5094	7.6
Total		100.0

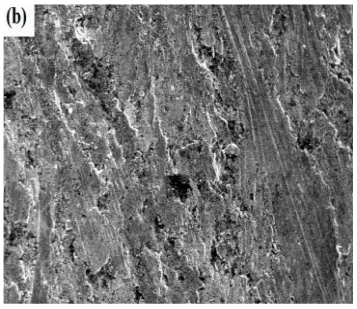

(b) EDS spectrum with chemical composition and location analysis on the welding zone (FZ)

Figure III.8.SEM/EDS point analysis on the weldments of AISI 304L

III.1.5. Ferrite content result

The ferrite content of the welded specimens in different zones: base metal (BM), HAZ and Fusion Zone (FZ) are tabulated in table III.2. It was observed that the ferrite content was higher in the FZ of 304L SS. In this zone, the high welding temperature enhances the δ-Ferrite formation as it is shown in figure III.9. The amount of δ-Fe decreases while moving away from the Fusion Zone (FZ) to the Base Metal (BM). It is also confirmed that the BM has a predominantly austenitic microstructure, with a smaller δ-Ferrite content of about 0.2 %. The presence of ferrite in the range of 4 – 8 % in austenitic stainless steel welds is ideal. This percentage has proven effective in controlling micro-cracking of weld metal during cooling.

Table III.2. Ferrite content in different zones: BM, HAZ and FZ.

Samples	Average Ferrite content (%)		Standard deviation (%)	
	HAZ	FZ	HAZ	FZ
EXP01	3.62	5.75	3.17E-03	2.67E-03
EXP02	2.37	5.85	2.33E-03	3.17E-03
EXP03	3.72	8.53	4.17E-03	3.67E-03
EXP04	2.1	5.47	2.00E-03	3.00E-03
EXP05	1.87	5.42	1.67E-03	3.50E-03
EXP06	2.37	7.05	2.33E-03	5.67E-03
EXP07	2.33	8.48	2.78E-03	4.50E-03
EXP08	3.83	9.85	5.44E-03	5.83E-03
Base metal BM	0.2		1.50E-04	

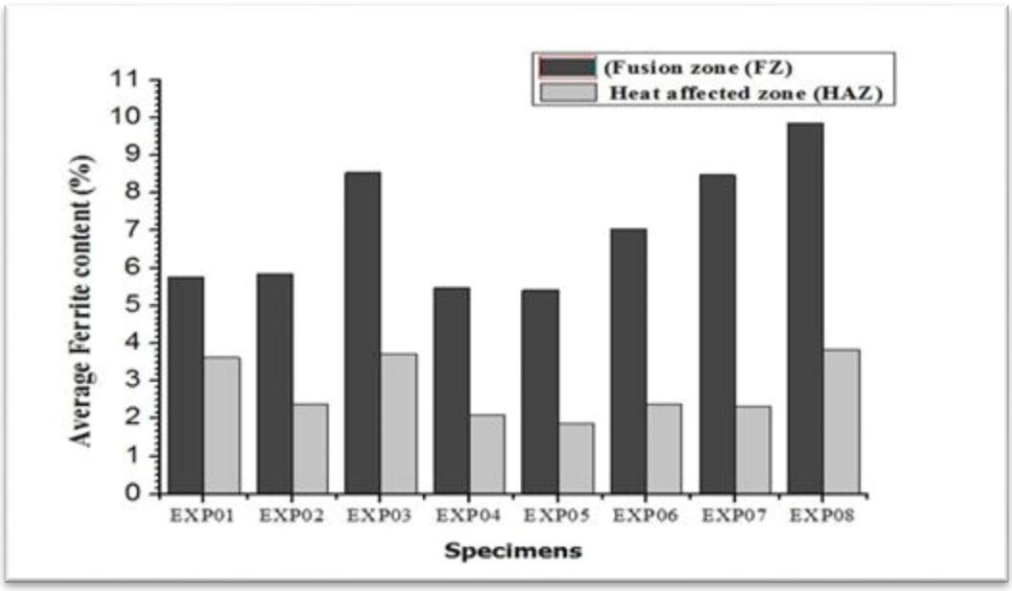

Figure III.9. Average ferrite content in two different zones (FZ) & (HAZ) of the eight specimens

III.1.6. Radiography result

X-ray radiography can be used to detect

- Heterogeneities (strong chemical segregation or inclusions),
- Continuity defects (volume defects (blowholes, porosities, shrinkages, cavities, etc.)),

- Two-dimensional defects (lack of bond in the case of welds).

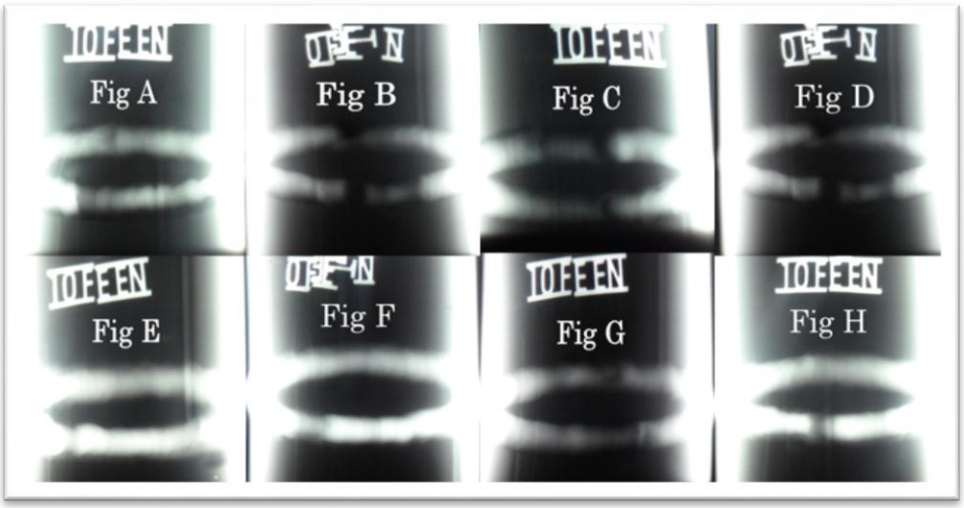

Figure III.10. Radiography test for the 08 specimens

The weld bead is irradiated by X-rays produced by an emission tube, the radiation interactions with the material cause differences in radiation absorption depending on the heterogeneities present. The zones without heterogeneities crossed by the radiation are targeted in clear, on the other hand the defects have dark zones. Generally the assemblies made by TIG, do not contain volume defects, and the welds show anomalies during the inspection, will be replaced by conforming welds [53].

Table III.3. Non-destructive control of radiography results

EXPERIENCE Number	**Face A**	**Face B**
EXP 01 (Fig A)	Crater sinkage, a lack of thickness	blowhole isolated , gutter
EXP 02 (Fig B)	flawless	bad recovery
EXP 03 (Fig C)	Bad recovery, blowhole isolated and gutter	blowhole isolated , level case
EXP 04 (Fig D)	flawless	bad recovery
EXP 05 (Fig E)	Bad recovery, blowhole isolated	bad recovery, gutter
EXP 06 (Fig F)	Blowhole isolated	spherical blowhole isolated
EXP 07 (Fig G)	Lack of fusion, gutter	lack of fusion, blowhole isolated
EXP 08 (Fig H)	transverse crack, crater crack	Excess of penetration

III.1.7. liquid penetration results

Over the years, this method has adapted to increasingly stringent hygiene, safety and environmental standards, and it remains widely used.

Indeed, apart from the low cost of implementation, one of the main advantages lies in the possibility of detecting faults such as cracks, corrosion cracks, porosity, pitting, etc. with great reliability, whatever their orientation and their location on the part to be checked, but also whatever the size and complexity of the geometry thereof. However, it is important to note that the faults must be through and unobstructed to allow reliable control.

In addition, PT can be defined as a global method, meaning that it is possible to inspect a part in a single operation or to process a large series of small parts at a time, which is naturally not possible by the radiography, gamma radiography, ultrasound or eddy currents, etc.

Those results are presented below:

Table III.4. Non-destructive control of Penetrant testing results

EXP N°	**Penetrant Testing Results**
EXP 01	The presence of pitting, Projection of tungsten
EXP 02	The presence of pitting, Projection of tungsten
EXP 03	The presence of pitting in HAZ, Projection of tungsten at base metal
EXP 04	Flawless
EXP 05	Projection of tungsten, tearing of the metal at the level of the HAZ, prick at the HAZ.
EXP 06	Flawless
EXP 07	Tearing of the metal at the level of the HAZ, pitting at the fusion joint
EXP 08	Deep pitting at the level of the HAZ, a fine crack at the fusion joint

III.2. Mechanical test results

In the mechanical part of our project, two different methods were measured as below:

III.2.1. Microhardness and residual stress profiles transversely to the welding direction

A Vickers microhardness tester (HWDM1) with a load of 0.981 N was used to measure the hardness. The microhardness maps were conducted transversely to the welding direction on the cross section of the joint with 50 µm between consecutive points.

Mechanical characterization by micro-hardness tests revealed a slight variation in the hardness profile between the three zones of the AISI 304L welded joints.

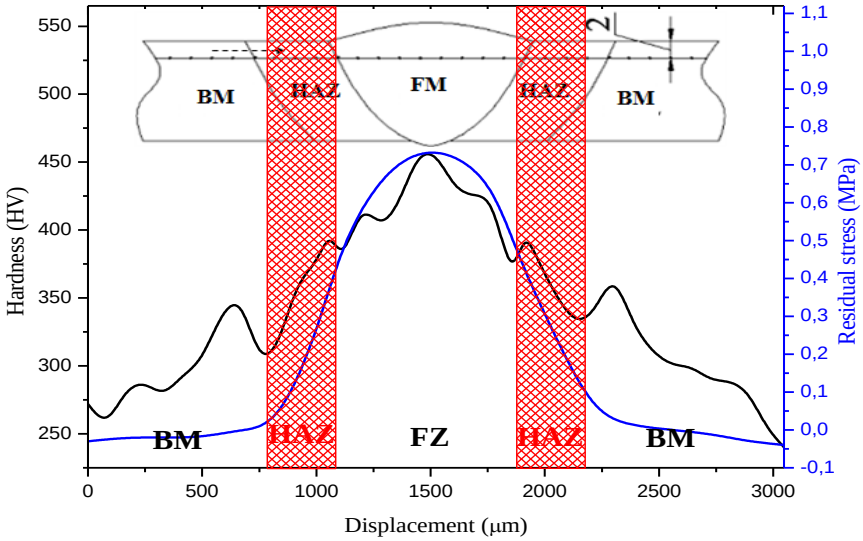

Figure III.11. Microhardness profile and residual stress across the weld metals for experiment 2

The microhardness curves across the welded joint can be divided into three regions depending on the microstructure. The microhardness of the MB sample is the lowest compared to that in other regions while the highest values remain at the molten zone.

The microhardness values of welded joints are related to the metallurgical condition. Therefore, the welding process has heat treatment effects on the weld, which promotes the formation of sigma phase precipitates in the melting zone.

The hardness of the fusion zone (FZ) was substantially higher than those of the HAZ and 304L SS base material. This result is due to the precipitation of the carbide particles and intermetallic compounds in FZ and HAZ, which resists to the propagation of slips across grain boundaries and consequently the material hardness increases.

The hardness of FZ and HAZ is slightly higher than that base metal. This is largely due to the high ferrite content, but a second contributing factor can also be residual stresses. The values of the standard deviation found illustrate the dispersion of the experimental point cloud, mainly due to the heterogeneous character of the microstructure. The melting zone has the highest value of the standard deviation due to the phenomena of chemical segregation.

III.2.2. Residual stress result

Figure III.12 illustrates XRD pattern in the Heat Affected Zone of the 304L SS. It reveals the presence of many intense peaks corresponding to austenite (γ-Fe) and some weak peaks corresponding to ferrite (δ-Fe). It also shows that the alloy contains $Cr_{23}C_6$, $FeCo_3$ and Fe_3C precipitates. The presence of precipitation in the heat-affected zone especially the carbide precipitate scan cause the fracture initiation as demonstrated by Curiel-Reyna and Verma

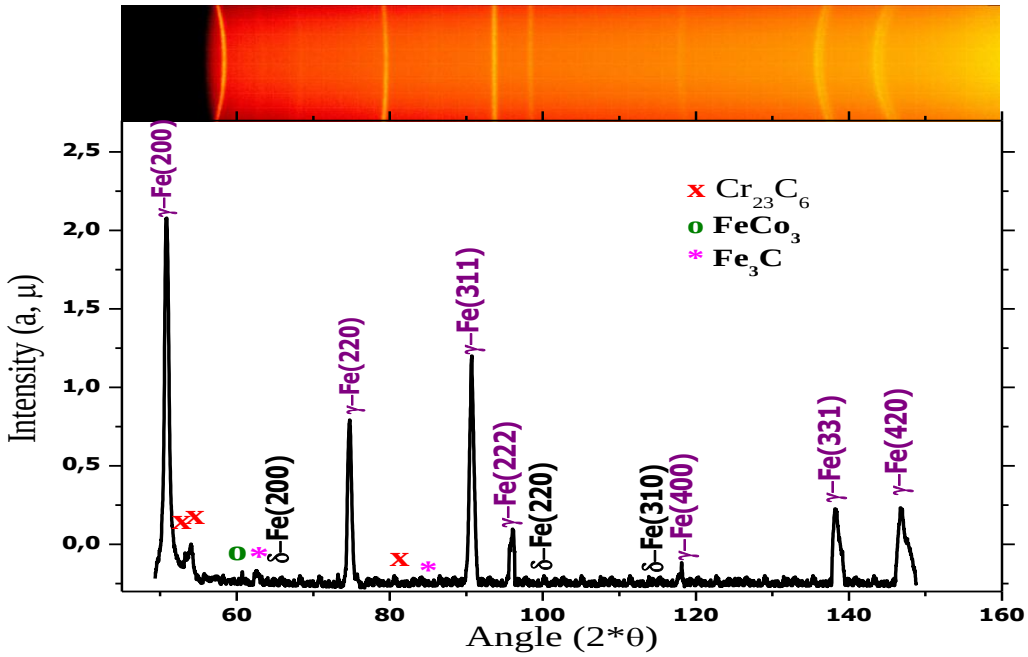

Figure III.12. XRD pattern of the samples in the Heat Affected Zone of the 304L SS [83].

The stresses were measured perpendicular to the weld (≈ 1µm from weld) at the diffraction angle of 147.1° in 2θ corresponding to the lattice plane family {420}. The stresses were evaluated using the $\sin^2\psi$ technique. The lattice spacing were determined for 12 ψ angles (figure III.13), ranging from 0° to 66° with stress oscillation of 6° to minimize grain size effects. After removal of a linear background, the diffraction peaks were fitted by a pseudo-Voigt function.

It is well known that during the welding process, residual stresses are introduced in the material as a result of thermal loading. In Figure III.12, the tensile stress, in the weld zone and HAZ, changes to compressive stress through the base metal. The maximum residual stress reached 0.7 MPa in the Fusion zone. The possible reason is that higher welding current leads to plastic deformation and contributes to relaxation of the thermo-mechanical stresses.

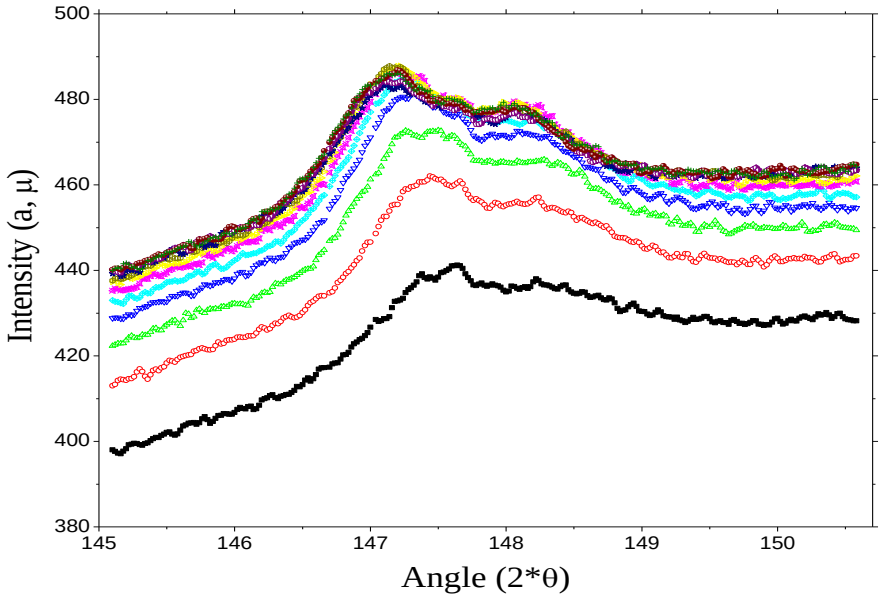

Figure III.13. Peak 147.1° displacement obtained from XRD measurements.

III.3. Use of an experimental design to study the contribution of operating welding parameters on the mechanical and metallurgical proprieties of Heat Affected Zone

The effect of welding parameters on the longitudinal welding residual stresses, microhardness, ferrite content and peak distortion at the Heat Affected Zone of 304L SS was investigated using an L8 factorial design. The experimental range and levels of independent variables for specimens are given in Table III.5. Mechanical and metallurgical proprieties responses are presented as follow: $R_2 = \sigma$: residual stress (MPa), R_3 = B: peak width (°2θ), $R_4 = F_{HAZ}$: Average Ferrite content in HAZ (%), and R5 = F_{FZ}: Average Ferrite content in FZ (%).

The increase of width peak, in HAZ, is due to the reduction in crystallite size and the increase of micro-strain. The sample (EXP 08) showed smaller lattice distortion with peak width about 1.56 µm

The increase of residual stresses in HAZ can be explained by the heating and cooling cycles produced during the welding process. From Table III.5, we can see that the residual stresses are negative and compressive in HAZ for all samples except Exp 03.

Table III.5. Mechanical and metallurgical measurement by Design Of Experiment

N° of exps	Avg	Input parameters			Output parameters			
		Number of passes (A)	Gas argon flow rate (B)	Current (C)	$R_2 = \sigma$ (MPA)	$R_3 = B$ (2θ)	$R_4 = F_{HAZ}$ (%)	$R_5 = F_{FZ}$ (%)
EXP01	1	-1	-1	-1	-51	1.91	3.62	5.75
EXP02	1	1	-1	-1	-53	1.74	2.37	5.85
EXP03	1	-1	1	-1	27	1.72	3.72	8.53
EXP04	1	1	1	-1	-76	2.21	2.1	5.47
EXP05	1	-1	-1	1	-19	2.19	1.87	5.42
EXP06	1	1	-1	1	-80	1.84	2.37	7.05
EXP07	1	-1	1	1	-104	2.42	2.33	8.48
EXP08	1	1	1	1	-15	1.56	3.83	9.85

The profiles of factors effects are shown in figure III.14. It was noted that the factors that affect the mechanical properties of HAZ are the welding current and the number of passes. Increasing in the welding current decreases residual stress and increases peak width. In fact, the higher welding current leads to plastic deformation and contributes to relaxation of the residual stresses. A high difference between the ferrite contents in HAZ and FZ at low welding current are detected. It was also observed that as the weld passes increase, the residual stresses decrease.This means that the relaxation of the tempering effect of the heat has occurred during successive runs. However, this parameter has no effect on the ferrite contents in the HAZ and FZ.

Increasing the number of passes has a negative effect on peak width. This phenomenon is correlated to the high weld depth penetration. The gas flow rate affects the metallurgical proprieties of the weld. The ferrite contents of both HAZ and FZ zones increase with increasing the gas flow rate. However, a slight effect on both residual stress and peak width was observed.

At the end, it can be concluded that the welding current has the main significant effect on the mechanical properties at low intensity level (50A). The most important effect of gas flow rate was observed at higher level 10 L/min. A compressive residual stress was obtained for 2 passes and with the lowest gas flow rate of 3 L/min. The welding current of 55 A is more appropriate for two passes to reduce the microstructure distortion.

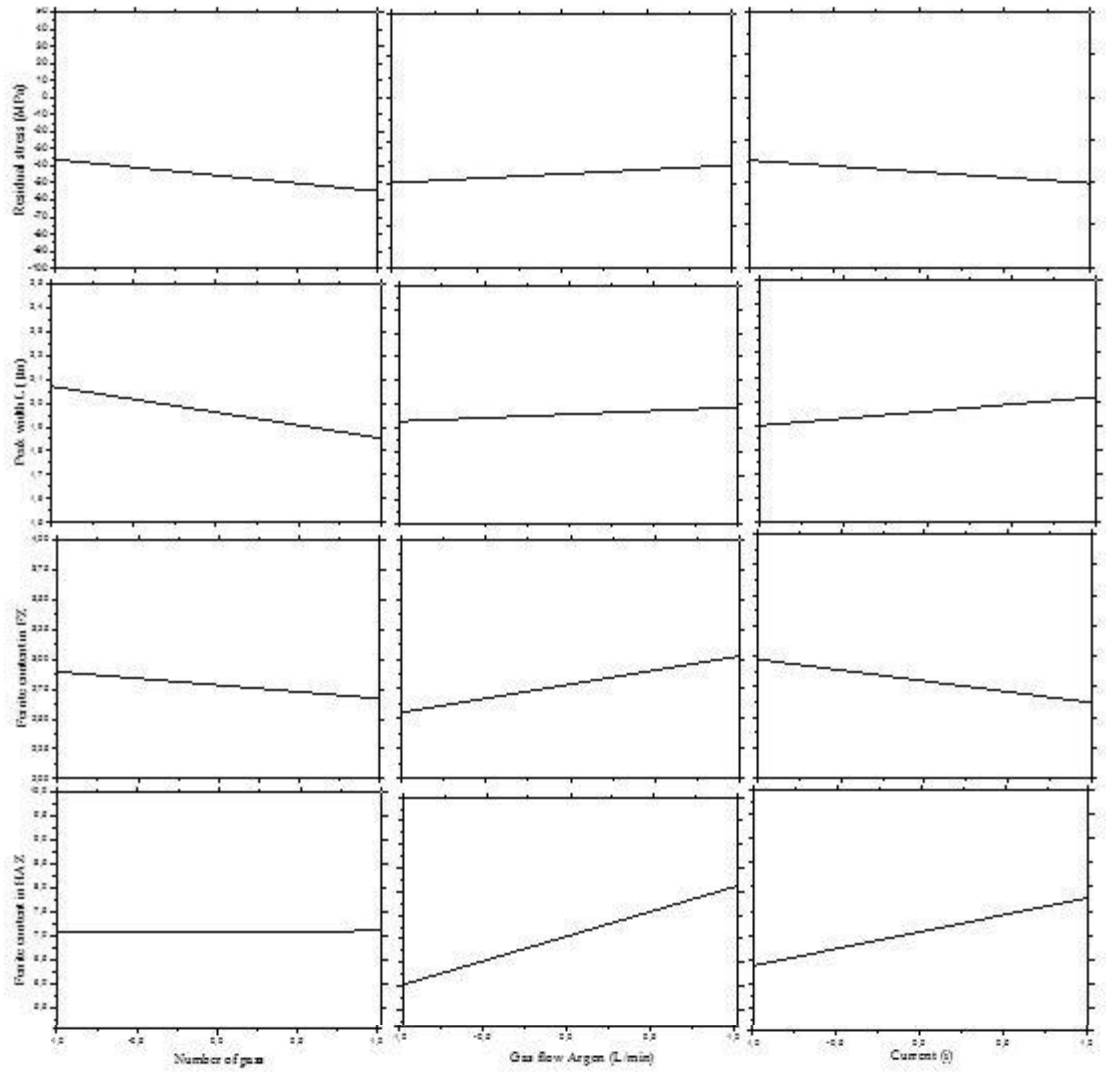

Figure III.14. Profiles of factors effects on corrosion resistance, residual stress and peak width

Generally, ferrite content in the HAZ is correlated to the FZ. A linear correlation is observed between corrosion potential and ferrite content in the HAZ in the range [0.032-2.33] of ferrite content ($R^2 = 0.931$). The ferrite content in fusion zone has negative correlation with corrosion potential.

III.4. Conclusion

The present study investigates the effects of three welding parameters (welding current, number of passes and argon gas flow rate) on the, residual stresses, peak width, ferrite content in FZ and HAZ. Based on the experimental investigation of the HAZ, we can conclude that:

- In the conditions of the present study, hardness value and residual stresses of the weld zone and HAZ change with HAZ microstructure and ferrite content.
- The micro hardness test results of the FZ were remarkably higher than those for the HAZ and the BM respectively.
- A compressive residual stress is correlated negatively with the both peak distortion and ferrite content in the fusion zone. However, there is no influence of the ferrite content in HAZ zone on the residual stress.

Chapter 4

Effect of welding Parameters on Corrosion resistance

The corrosion behavior and mechanism of Stainless steel AISI 304L welded joint by filer metal AISI 308L were investigated using the input parameter of welding process and characterization result as the output parameters.

This chapter presents the effect of welding parameters on the corrosion resistance of welded joints. An experimental design approach is used to study the welding process parameters effects on the corrosion statement at the Heat Affected Zone (HAZ). Three welding parameters are selected as input variables: Number of pass, gas flow (argon flow) and welding current. The various microstructures of the welded joint were characterized by electrochemical techniques as potentiodynamic polarization and impedance spectroscopy EIS.

IV.1. Study of the corrosion mechanism by potentiodynamic tests of AISI 304L

Potentiodynamic polarization is a destructive technique where the potential of the electrode is varied at a selected rate, and the resulting current is measured.

IV.1. 1.Polarization behavior in 3% NaCl

Figure IV.1 shows the electrochemical behavior for two experiments (EXP 02: with double pass and EXP 07: with single pass). The polarization curves of the above two samples are similar but the corrosion current densities of the two samples are considerably different, showing the effect of the welding parameters on the microstructure. The corrosion current densities of the three zones are different and in concordance with the amount of the ferrite content (table III.2). For both samples (figure IV.1.a and IV.1.b), the Fusion Zone has the greatest polarization resistance. A potential difference exists between the BM, HAZ and FZ, which provides a galvanic coupling between these zones.

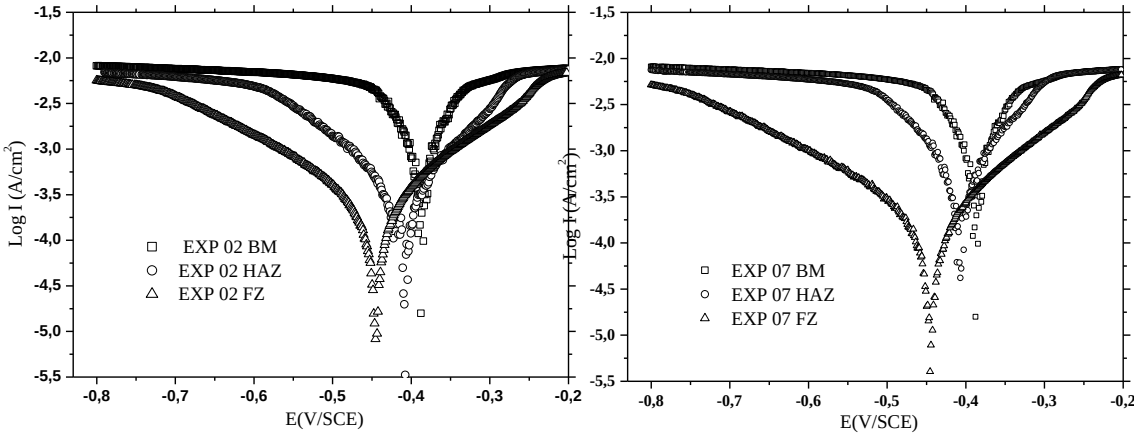

Figure IV.1. Potentiodynamic polarization curves of BM, HAZ and FZ for two experiments: 02 with 2 passes and 07 with one pass.[83]

Electrochemical corrosion test results of the Heat Affected Zone under different welding parameters in 30g/L NaCl at room temperature are presented in Figure IV.2and Table IV.1. The corrosion current density, I_{corr}, and corrosion potential were obtained from a Tafel plot by extrapolating the linear portion of the curves. The polarization resistance, R_p, can be calculated by taking the inverse of the slope of the current potential curve at corrosion potential (IV.1)

$$R_p = \frac{1}{2.303}\frac{b_a b_c}{b_a + b_c}\left(\frac{1}{I_{corr}}\right) \quad \text{..... (IV.1)}$$

b_a and b_c were the slope of the Tafel plots and I_{corr} is the corrosion current. The samples display less similar behaviors in terms of the corrosion potential, whereas their corrosion current varied strongly with change in welding parameters, which reveals susceptibility to corrosion of material. Comparatively with results of the Table III.2, the better corrosion behavior is observed for the samples with the high ferrite content at the FZ. The better corrosion resistance of the material was obtained for Exp 08.

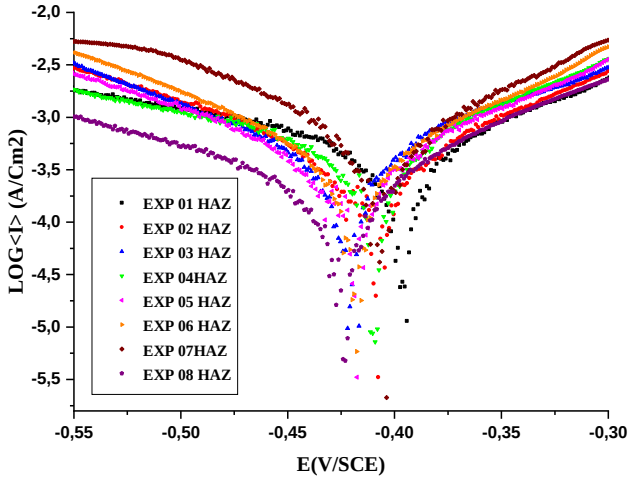

FigureIV.2. Potentiodynamic polarization curves of HAZ of different weld metals.

IV.1. 2.Interpretation of the results of potentiodynamic tests

The curves (Figure IV.2) represent the variation of current intensity as a function of potential with a scanning speed of $1mV.s^{-1}$ over an interval of [-190 ~ 190 mV]. Note that 304L stainless steel undergoes rapid dissolution (increased slope in the negative part of the potential) due to the first contact with the solution, then the alloy has a passivable behavior due to the formation of a protective layer which prevents the dissolving metal ions and acts as a barrier. The rupture of the passive film differs from one experience to another: it is the transpassive domain. This phenomenon is due to the presence of chlorine after corrosion, which attests that the Cl^- ions have been adsorbed by the passive layer of 304L stainless steel which produces pitting corrosion. Several pitting were observed on the surface of the sample after corrosion.

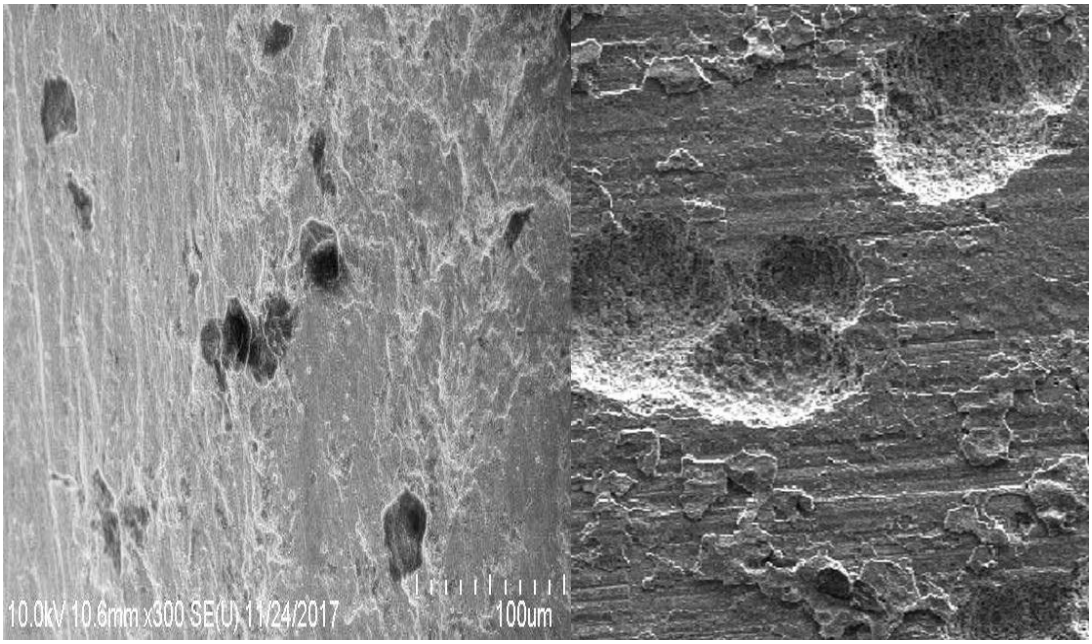

Figure IV.3.pitting corrosion of welded AISI 304L sample

Table IV. 1: Electrochemical parameters obtained from Tafel plot for HAZ

Experiences number	**icorr (µA/cm²)**	**-Ecorr (mV)**	**Rp (Ω)**
EXP 01	484.50	397.34	53.80
EXP 02	441.14	407.73	76.99
EXP 03	460.14	422.01	56.70
EXP 04	499.76	410.19	52.20
EXP 05	365.15	419.90	71.40
EXP 06	473.12	418.61	55.10
EXP 07	491.21	406.68	53.00
EXP 08	216.63	424.84	120.00

IV.2. Study of the mechanism of corrosion by electrochemical impedance

The Electrochemical Impedance Spectroscopy (EIS) [84-86] is a technique non-destructive, and it is based on the excitation of the working electrode by a low amplitude alternating current (AC) voltage at several discrete frequencies logarithmically distributed along several decades.

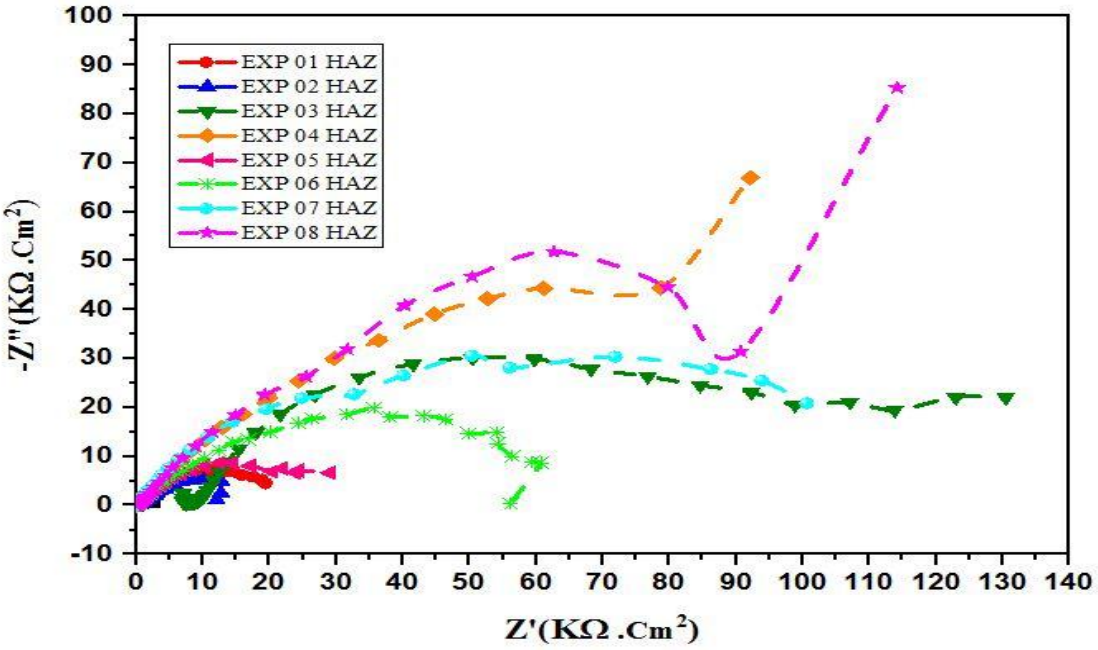

FigureIV.4. Nyquist diagram of 304L SS in HAZ for different weld metals inNaCl solution 3 %w/v.

IV.2.1.Interpretation of EIS test results

FigureIV.4 shows the Nyquist plots obtained for stainless steel samples dipped into the solution of 3% Nacl as concentration with change of the deferent welding parameters. As can be seen from the figure, all the plots contain depressed semicircles. The capacitive loop observed in all EIS diagrams can be related to the charge transfer reaction and the electrical double layer formed on the metal surface

The deviation from pure semi-circle behavior known as frequency depression happens due to roughness and inhomogeneity of the surface during corrosion.

From the Nyquist plot, it is obvious that weld tick samples have highest corrosion resistance tendency than base metal and the semicircle radius decreases from 4 mm weld to 4 mm base.

Fig IV.4 presents the electrical equivalent circuit proposed to model EIS spectra where Rs represents the solution resistance, Rct the charge transfer resistance and CPE_{dl} the constant phase element. The simple R(RC) equivalent circuit is commonly used for the systems with one time constant. In the circuit, CPE has been introduced account for the frequency depression phenomenon. The parameter admittance and exponent of CPE, respectively. The CPE exponent ranging from 0 to 1 is a good indication of the surface condition .

Table IV.2 : Electrochemical parameters obtained from EIS: (Nyquist) and (bode) plot for HAZ.

Experiences number	Rp ($\Omega.Cm^{-2}$)	R_{ct} ($\Omega.Cm^{-2}$)	CPE.e^{-2} (F)	Log(|Z| /$\Omega.Cm^{-2}$) Max
EXP 01	19,416	6,994	2,481	4,301
EXP 02	12,066	5,275	2,672	4,183
EXP 03	100,125	30,062	1,891	5,012
EXP 04	92,156	44,474	1,423	5,121
EXP 05	29,049	8,712	2,182	4,622
EXP 06	34,930	19,855	2,071	4,790
EXP 07	100,621	30,544	1,633	5,062
EXP 08	114,245	51,787	1,184	5.154

The Nyquist plots of welding specimens from the EIS measurement in fig.4 shows the real component (*Z'*) and the imaginary component (*Z''*) of the impedance of the AISI 304 austenitic stainless steel welded at different welding parameters and 3% NaCl as electrolyte solution specially in the heat affected zone (HAZ).

In Nyquist diagram (Figure IV.4) all 304SS samples show a capacitive behavior respectively from higher to lower altitude of the semi circles, as expected for austenitic stainless steel in aerated NaCl 3% w/v solution.

These impedance curves reveal similar corrosion pattern for all specimens since their electrochemical features are relatively similar. At high frequencies, these curves are characterized with single capacitive loops due to inherent charge transfer processes controlling the corrosion reactions.

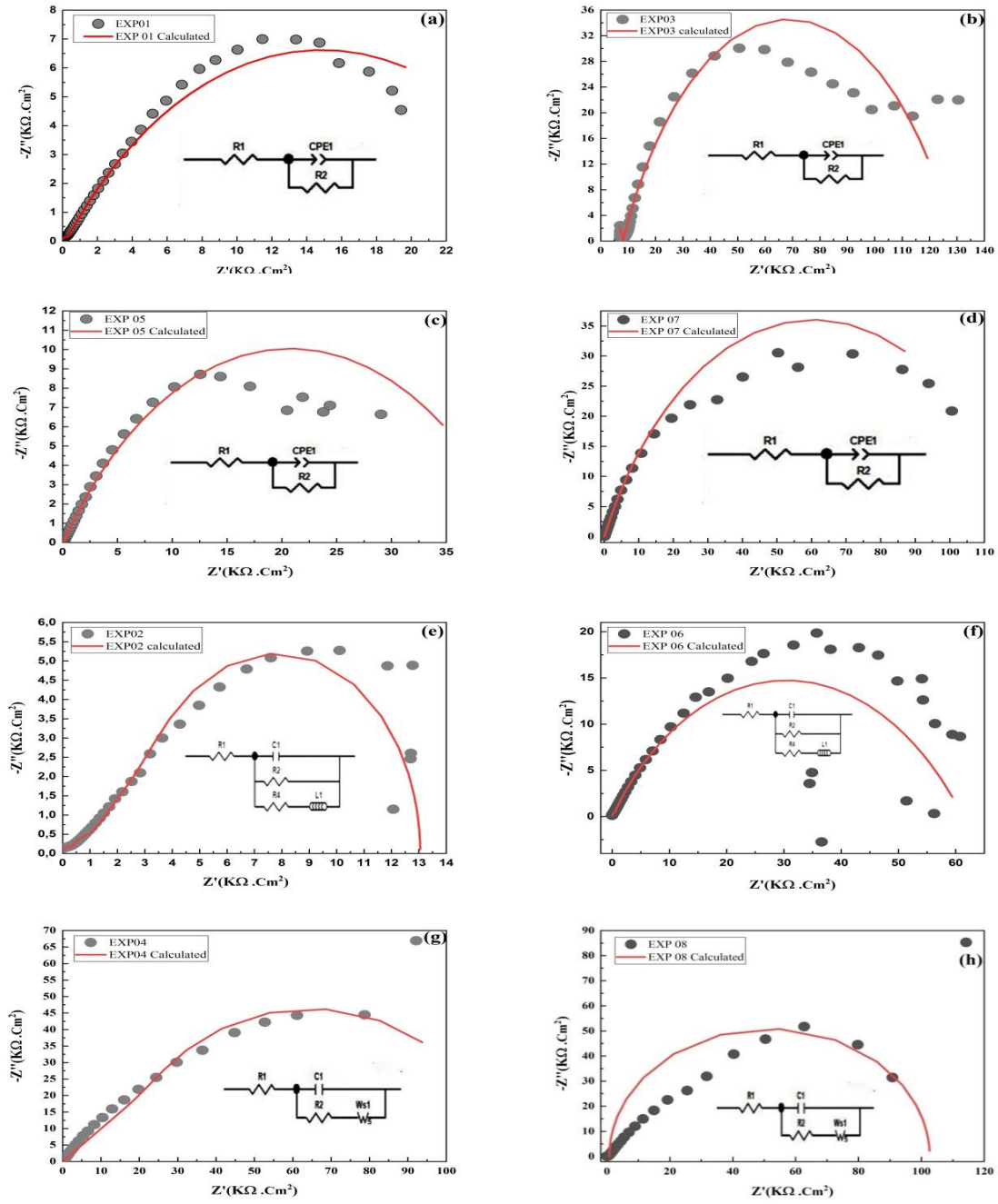

FigureIV.5. Nyquist curves and fits based on the equivalent circuits for modeling the impedance data, in 3 %w/v solution of NaCl at different welding parameters.

The Nyquist plot of the samples 8, 4, 7, 3 and 6 respectively samples resulted in semicircles with larger diameters indicating higher values of polarization resistance, due to a faradaic process of high charge transfer resistance. The pending samples 5, 1 and 2 showed the smallest diameter semicircle resulting in the lowest polarization resistance. Experimental impedance data were fitted into an appropriate equivalent circuit model as

shown in Figure IV.5. The electrochemical parameters extracted from this theoretical operation are presented in Table IV.2.

The variations in impedance at different frequencies can be explained by considering the passive film as an amorphous or highly disordered semiconductor; highly disordered nature implies a high charge density. When a semiconductor is brought into contact with an electrolyte,

a thermodynamic equilibrium is established which modifies the free charge densities on either side of the interface so as to equalize the electrochemical potentials [92-93].

The equivalent circuit equipped with simple Randle cell is shown in Figure IV.5 where the double-layer capacitance (Cdl) (the solution–substrate interface) represents the CPE represented in Figure IV.5 parallel to impedance, i.e., the resistance of polarization (Rp) and in series with corrosion solution resistance (R_s) [87], R_{ct} is the charge transfer resistance at the solution–substrate interface. The calculated impedance parameters are enlisted in Tables IV.2.

An equivalent circuit model has been proposed .Nyquist plots only contain a semi-circular appearance which is attributed to a passive surface. Therefore, the phase constant element (CPE) is used to model the impedance of the electrical double layer.

Figure IV.5 ; Exp 02 et 06, the equivalent circuit corresponding to SS304L under different welding parameters as shown in Table IV.2, comprising a time constant and an inductor. When an electrode is placed in an electrolyte, its surface is severely corroded and the absorption and reabsorption of the corrosion debris on the surface generate an effective inductance.

The impedance spectrum of each sample in the 3% NaCl solution may include several inductive loops where each inductive loop represents the substance adsorbed on the surface. High surface porosity and holes with relatively large diameters generate ways of infiltration of the electrolyte into the substrate's metallic surface. Therefore, the less porous the surface, the higher its resistance to corrosion. Thus holes and the porosity field have been tested by using the CND techniques corresponding to the visual inspection of the welding joint presented by the acceptable defaults of welding and crater holes. These phenomena belong to higher pass number and less gas flow argon (without protection).

The Nyquist plot contains a semicircle curve with two intersecting points for the real axis (Z'), Values of solution resistance (R_s) obtained from the first intercept point, closer to the origin, and the value of total resistance (R_s+R_{ct}) obtained from the second intercept farthest from the origin point. Simultaneously, the double layer capacitance C_{dl} is measured

from the intermediate frequency from the equation.

$$C_{dl} = 1/ (\omega \times R_{ct}) \quad \text{(IV.2)}$$

Where $\omega = 2\pi f$ where f is the frequency in Hertz

The semicircular curve is attributed to the small charge transfer capacity between oxide coating and solution. In contrast, the linear curve of the non-anodized sample refers to the increases in the diffusion of corrosive species through the pores in the metal/solution interface. The straight line indicates a diffusion mechanism of ions through the pores.

Two regions are clearly seen; a semicircle response is due to the charge transfer reaction and straight line with a 45° angle to the abscissa means to the diffusion of reactants. This is typical for analytical electrochemistry in diffusion controlled (W) in corrosion measurements, which is expressed by the Eq. (IV.3), where σ is the Warburg coefficient and can be calculated from the slope of the straight line in the complex plane of Figure IV.5(g) & (h).

$$W=\sigma.\omega^{-1/2(1-J)} \quad \text{(IV.3)}$$

The linear curve presented on the sample number 4 and 8 can be explained by considering the precipitation of chromium carbides which is localized at the grain boundary because they are high-energy regions. This has been explained as that, in fine-grained material, there are more grain boundary areas (GBA) and therefore less chance for a continuous network of carbides to form at the grain boundaries. In our case especially in the Heat affected zone, the GBA are less compared by the fusion zone, leads to the continuous diffusion of the chromium at the high distance between the grain; hence the possibility of sensitization is increased even the desensitization is also decreased in this case , the replenishment will be decease at higher distance .as known the Carbide precipitation is accelerated at higher temperatures, whereas it is slowed down at lower temperatures, thus related to the welding current improvement. The increase of number of pass at less thickness also had more influence on the GBA and the zone got less fine grained also the increasing of the grain size is referred to the increases of the susceptibility to intergranular corrosion (IGC) and intergranular stress corrosion cracking (IGSCC) due to sensitization as presented in the figure.6.

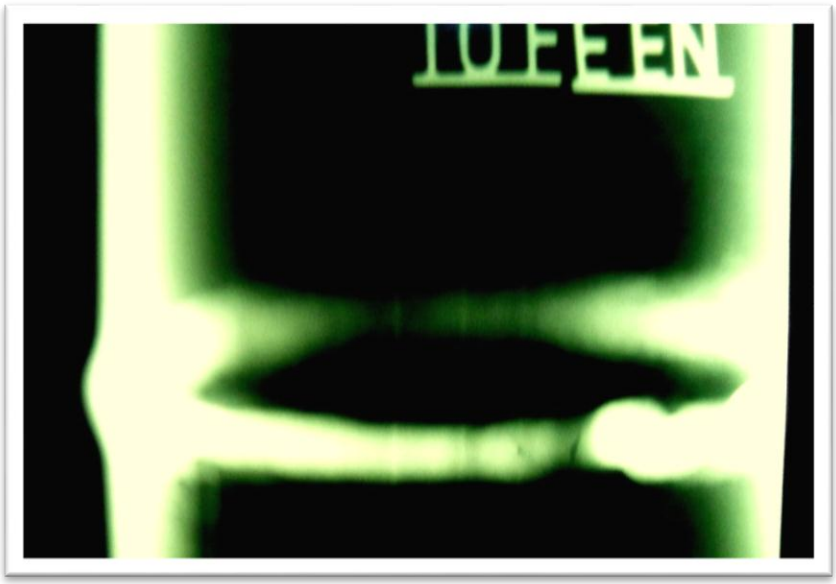

FigureIV.6. Crack detection using radiography at specimen eight

Local stresses arise in areas where secondary phases begin to precipitate and grow .Due to this considerable energy differentials are produced in these zones. This leads to imperfect passivation those results in poor corrosion resistance.

The specimen number 07 shows a lower value of CPE (1,18 . 10^{-2} µF/cm^{-2}), whereas specimen number 02 shows higher value (2,67. 10^{-2} µF/cm^{-2}. The lowest value of CPE leads to a thicker and more protective passive film that provides better resistance to corrosion. These results may be related to the presence and the competition of two kinds of oxides, chromium and iron. At low potentials (potentials lower than the trans-passive potential of chromium), passive films are more enriched with chromium, making the films more protective. At high potential in the passive range, chromium decreases continuously and iron increases progressively and hence the protective effect reduces [88].

From Figure IV.6, it could be observed that all the Bode plots decrease with load, and it presents the same capacitive semi-circles.

The Bode plot measurement in 3% NaCl solution is shown in Figure IV.7. It is evident that the impedance magnitude varies with the frequency Area combined with the nature of passive film formation. The magnitude of impedance in higher-frequency area is related to the oxidation process and describe the anodic behavior of the sample, whereas the lower-frequency region is associated with the reduction behavior of the NaCl.

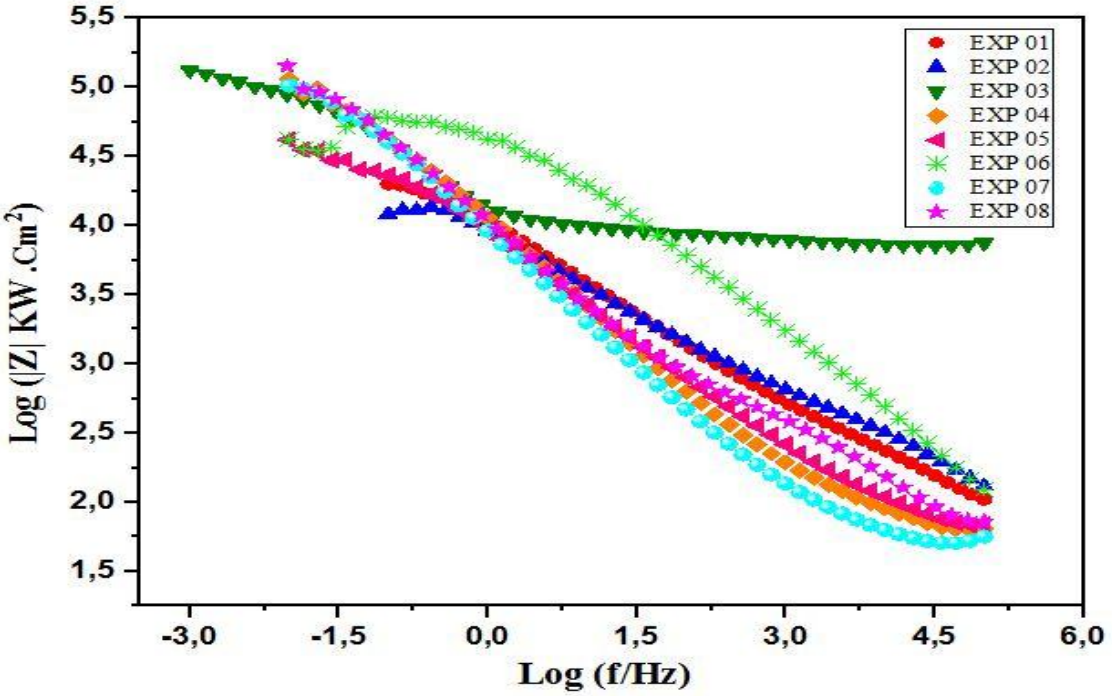

FigureIV.7. Bode diagram: impedance module for the 304SS of different weld metals NaCl solution 3 %w/v.

In Bode plots, the impedance modulus at low-frequency region signifies the resistance to corrosion, while the higher impedance values at high-frequency region signify the passive film compactness [89,90]. Similar to the Nyquist plots, the higher impedance values can be seen for sample number 8, 4, 7, 3 and 6 respectively; all of them have a higher impedance modulus at lower frequencies. A similar trend can be seen for impedance modulus at high-frequencies region. Hence, these results indicate that exp 07 depicts more corrosion resistance than Exp 02. This can be attributed to fine-grained structure in the exp07 [91].

IV.3. Use of an experimental design to study the contribution of operating welding parameters on the corrosion mechanism

The quality characteristics after the polarization tests, impedencemetry and bode tests were evaluated to verify the effect of the experimental parameters, using an L8 factorial design for a robust experimental design. All the electrochemical and mechanical parameters were presented in response form.

The characteristics measured and the responses calculated for each series of experiments are presented in Table IV.2.The profiles of factors effects are shown in figure IV.8. It was noted that the factors that affect the Electrochemical properties of HAZ are the

gas flow argon and the number of passes. Increasing in the gas flow argon increase the charge transfer resistance R_{ct} , in other side the increasing of the number of pass increases slightly the corrosion resistance.

Increasing the gas flow argon has a positive and higher effect on the resistance charge of transfer. This phenomenon is correlated to the high protection of the internal welding joint. The gas flow rate affects the metallurgical proprieties of the weld.

The welding current factor has a slightly positive effect corrosion resistance due to weld depth penetration. The gas flow rate affects the metallurgical proprieties of the weld.

Decreasing of the gas protection flow (gas argon) has a positive sense on the CPE; this influence leads to a thicker and more protective passive film that provides better resistance to corrosion whereas the pass number and welding current slightly affected on the CPE.

From figure 8, we can found correlation between responses summarized as follow:

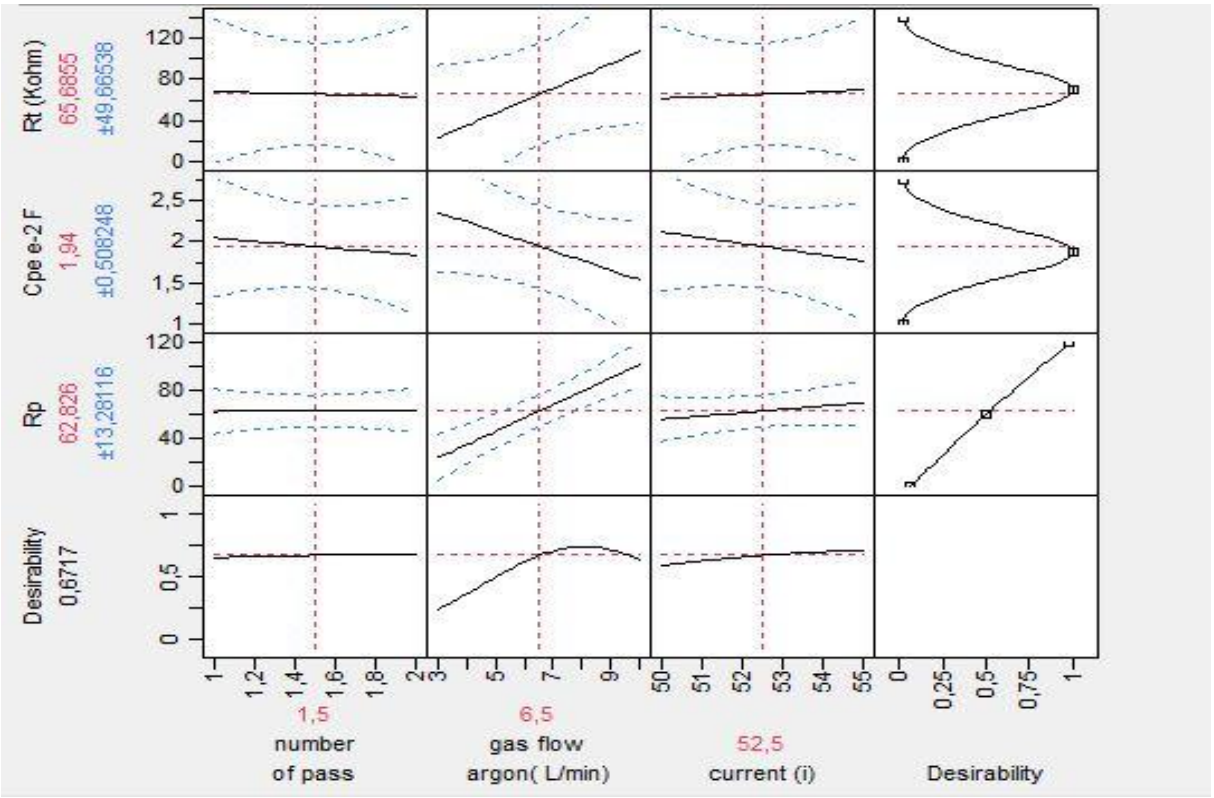

Figure.V.8. Profiles of factors effects on corrosion resistance, resistance charge transfer and double layer capacitance represented on (CPE)

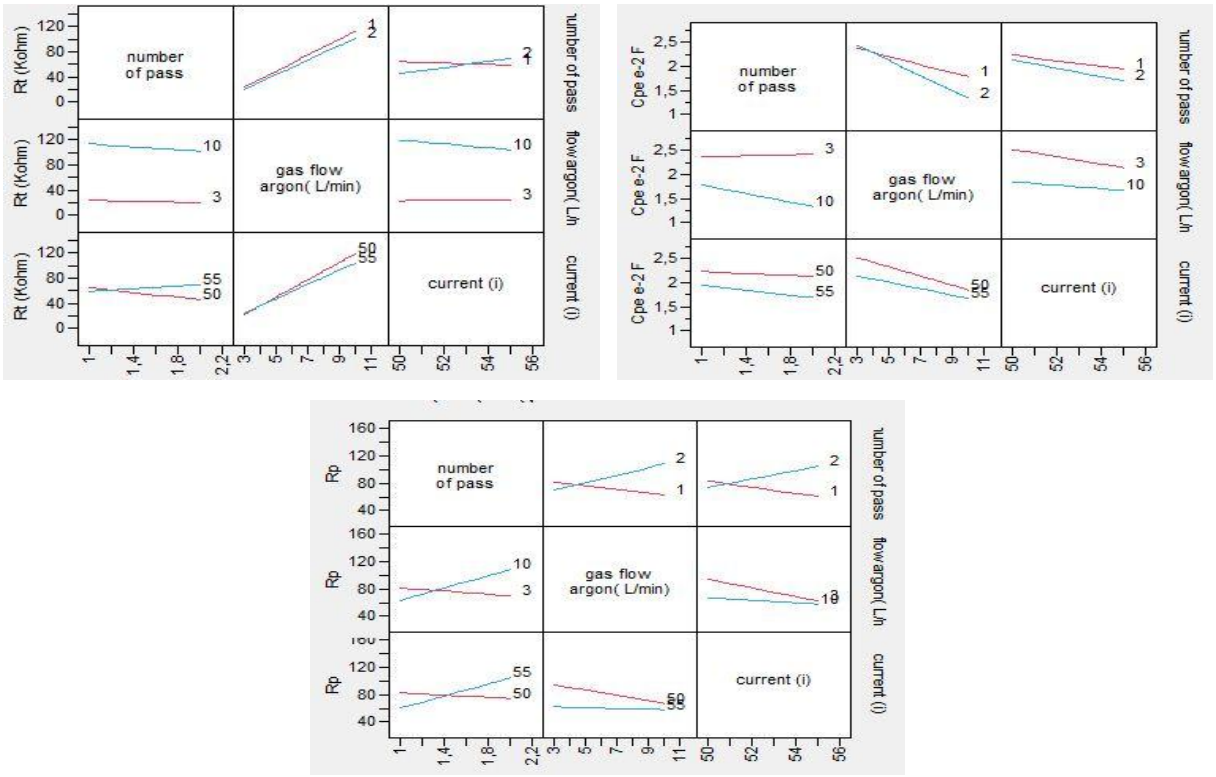

Figure V.9. Interaction profiles of factors effects on corrosion resistance, resistance charge transfer and double layer capacitance represented on (CPE)

V.4. Conclusions

The purpose of this Chapter is to use an application of full factorial design for GTAW Welding parameters to reduce the effect of stress corrosion .to achieve this target , the paper offers a five-step strategy to apply design of experiment technique in studying a process and optimizing the welding process performance.

In step1, the main factors are selected that are used for further investigation. In step 2, the factors and their levels are chosen for the full-factorial experimentation. In step 3an experimental design is selected. In step 4, a randomized of all the combinations of experiments was done by JMP software. In step 5, the optimal settings of the welding process parameters were chosen.

The electrochemical characterization by potentiodynamic polarization and EIS was carried out in order to understand the magnitude of the welding parameters on the corrosion behavior of stainless steel.

Corrosion resistance has non-linear correlation with residual stress as the stresses are tensile or compressive, and it is in a good correlation with high ferrite content in the FZ and

the HAZ zone. The both peak distortion and corrosion potential have identically the same correlation with the corrosion resistance.

The use of an experimental design allowed us to highlight the effect of the experimental parameters as well as to evaluate the contribution of the operating parameters on the corrosion mechanism. Among the three factors and 2 levels examined, we concluded that the gas flow argon is the most significant effect on the polarization resistance, charge transfer resistance and phase constant element. The slight variation in R_P and R_{ct} after corrosion tests were found to be influenced by increasing of the pass number.

The full factorial design represented by the welding parameters and the electrochemical responses, these results conclude that the optimum specimen from the 8 specimens is represented in the sample number seven.

General Conclusion

This thesis proposes to study the electrochemical & behavior of a welded joint in austenitic stainless steel AISI 304L, susceptible to stress corrosion in a neutral chlorinated medium at a concentration of 3%. We approached this problem under the heading "materials" by establishing a close link between the metallurgical state of welded joints with their resistance to corrosion and more precisely, the passivation mechanism.

In the piping industry, the choice of austenitic stainless steel is preferred to remedy the risk of corrosion of the austenitic grade (AISI 304L). The bibliographical aspect was diversified and enriched, targeting the study in question and the various points relating to the aspects of welding, corrosion and degradation of stainless steels.

Our work within this theme "Damage to Metallic Materials- Study project on techniques and early detection of SCC in stainless steels Type 304L Control of initiation and propagation of SCC cracks, has led us to carry out the following operations:

- A mechanical characterization was made by measurements of the micro-hardness and residual stress impact of the samples.
- A metallographic characterization was carried out by optical and scanning electron microscope allowed us to see the change in the microstructure of stainless steel afterwards and to observe the evolution of the surface state of the samples and the observation of corrosion. by pitting after the electrochemical tests.
- The electrochemical characterization by potentiodynamic polarization and impendency was carried out in order to understand the extent of the welding parameters on the corrosion behavior of austenitic steel 304L.

The metallurgical study showed the effect of welding on the balance of the phases present and the morphological texture. However, the quality of the welded joints is found to be very satisfactory; the weld bead has good mechanical properties, compatible with the base metal. The study of SEM fracture facies allowed us to confirm the transition from intergranular rupture mode to trans-granular rupture. This is due to the precipitation of the ferrite phase by the metallographic study by the presence of cups in the different areas of the

welded joints and the SEM analysis confirmed the ductile nature of the fracture (micro-cracks and micro defects in the melting zone).

The corrosion resistance of stainless steel is determined by the compactness of the passive film covering its surface [92]. With a uniform chemical composition, the non-sensitized 304L substrate does not exhibit a microscopic heterogeneous texture, such as "Cr depletion regions at grain boundaries." The defects of the passive film on the non-sensitized 304L substrate are randomly distributed. Some heterogeneous points may exist at the inclusions and secondary-phase grains. However, carbides and Cr depletion regions develop along the grain boundaries after sensitization. These regions induce a local galvanic coupling effect that accelerates grain boundary corrosion and eventually triggers SCC. This process is the IGSCC mechanism of 304L in anodic dissolution (AD) media.

The frequency sweep impedance tests have demonstrated the transfer of charges at high and medium frequencies which is established between the substrate and the saline solution.

In the absence of a solid insulating layer on the surface of the metallic substrate (stainless steel), the high frequency loop is generally considered to be linked to the charge transfer process. The low frequency loop corresponds to a contribution related to mass transport due to the dissolution of steel.

The drawback of these impedance measurements lies in their interpretation, which is quite delicate, and in the fact that several theories co-exist, in particular for the explanation of the formation of the semicircles which appear at medium frequencies. It would therefore be advisable to continue research in this field, because the non-destructive and reliable assessments of the corrosion states of steels are of definite interest for the diagnosis of equipment.

The use of an experimental design allowed us to highlight the effect of the experimental parameters as well as to evaluate the contribution of the operating parameters on the corrosion mechanism.

we adopted an experimental design based on the factorial experimental design FED method to quantify the effect of the experimental conditions (number of passes, welding current and flow of argon gas in chlorides of the microstructure of the sample. tested) on the corrosion resistance of 304L stainless steel.

Bibliographic references

[1] G.R. Mirshekari, E. Tavakoli, M. Atapour, B. Sadeghian,Microstructure and corrosion behavior of multipass gas tungsten arc welded 304L stainless steel,TheJournalofMaterial and Design.55(2014)905–799.

[2] Wang.S, Ma.Q and Li.Y, Characterization of microstructure, mechanical properties and corrosion resistance of dissimilar welded joint between 2205 duplex stainless steel and 16 MnR.Mater.Des,32(2011) 831-837

[3] B. Sunil Kumar, Vivekanand Kain, K. Benerjee, P.D. Maniyar, S. Sridhar, Kumar Jitendra, Kumar Jatin., Effect of Oxidation on Corrosion Behavior of Austenitic Stainless Steel 304L Welds, Advanced Materials Research, Vol. 794, pp. 598-605, September 2013.

[4] A. Z. Sadek and A. M. El-Sheikh, Failure Analysis of SS 304 Weldments by Metallurgically Enhanced Stress Corrosion Cracking in Laboratory Environments, Corrosion 2000.

[5] Raman, K.R.; Siew, H.W. Stress corrosion cracking of an austenitic stainless steel in nitrite-containing chloride solutions. Materials 2014, 7, 7799–7808.

[6] OKENIYI, J. O. (2017). Effects of Single Pass and Multipass Welding on Austenitic Stainless Steel Corrosion in Aggressive Environments. Gazi University Journal of Science, 30(4), 514-529.

[7] Wichan.C, Loeshpah,.S., The behavior of nitrogen on the Welding parameters of the dissimilar weld joints between AISI 304 and 316 L austenitic Stainless Steels produced by gas tungsten arc welding. App.Mech.Master, (2013), 248, 395-401

[8] A.K.Srirangan, S.Paulraj. Multi Response optimization of process parameters for TIG Welding of incoloy 800HT by Taguchi grey relational analysis,Eng. Sci. Technol. Int. J. (2015) doi: 10.2016/ J.Jestch.2015.10.003.

[9] Jayakrishnan, S., & Chakravarthy, P. (2017). Flux bounded tungsten inert gas welding for enhanced weld performance—A review. Journal of Manufacturing Processes, 28, 116-130.

[10] Noureddine DJEDDI, Hamida ESSOM, Merzoug BENAHMED; Elecctrochemical Behavior of austenitic stailess steel welded by the GTAW process in A chloride environement, 3rd International Conference on Welding, and NDT and the Materials and Alloys Industry (IC-WNDT-MI'12)

[11] Srirangan, A. K., & Paulraj, S. (2016). Multi-response optimization of process parameters for TIG welding of Incoloy 800HT by Taguchi grey relational analysis. Engineering science and technology, an international journal, 19(2), 811-817

[12] Sonasale, P. (2015). An approach to optimize Mig welding parameters by using Design of Experiments. International journal of Advanced Materials Manufacturing & Characterization, 5(1), 24-34.

[13] L.Chum-Ming, S.Te-Li, W.Keo-yuan, Effects of parameter optimization on microstructure and properties of GTAW clad welding on AISI 304L stainless steel using Inconel 52M, The international journal of advanced Manufacturing Technology, August 2015, Vol79, Issue 9-12, 2057-2066.

[14] Sule, J., Ganguly, S., Coules, H., & Pirling, T. (2015). Application of local mechanical tensioning and laser processing to refine microstructure and modify residual stress state of a multi-pass 304L austenitic steels welds. Journal of Manufacturing Processes, 18, 141-150.

[15] Zakaria, B., Soumia, H., & Vincent, J. (2016). Effect of Heat Treatment on the Microstructural Evolution in Weld Region of 304l Pipeline Steel. Journal of Thermal Engineering, 2(6), 1017-1022.

[16] J.sule, S.Ganguly, W.Suder, T.pirling, Effect of high-pressure rolling followed by laser processing on mechanical properties, microstructure and residual stress distribution in multi-pass welds of 304L stainless steel, The international journal of advanced Manufacturing Technology, September 2016, Vol 86,Issue5-8, 2127-2138.

[17] Jian, Z., & Hejing, W. (2003). The physical meanings of 5 basic parameters for an X-ray diffraction peak and their application. Chinese journal of geochemistry, 22(1), 38-44.

[18] Ilić, A., Ivanović, L., Josifović, D., Lazić, V., & Živković, J. (2018, July). Effects of welding on mechanical and microstructural characteristics of high-strength low-alloy steel

joints. In IOP Conference Series: Materials Science and Engineering (Vol. 393, No. 1, p. 012020). IOP Publishing.

[19] Acharyya, S.G.; Khandelwal, A.; Kain, V.; Kumar, A.; Samajdar, I. Surface working of 304L stainless steel: Impact on microstructure, electrochemical behavior and SCC resistance. Mater. Charact. 2012, 72, 68–76.

[20] Giridharan, P. K., & Murugan, N. (2007). Effect of pulsed gas tungsten arc welding process parameters on pitting corrosion resistance of type 304L stainless steel welds. Corrosion, 63(5), 433-441.

[21] Sunil Kumar, B., Kain, V., Benerjee, K., Maniyar, P. D., Sridhar, S., Jitendra, K., & Jatin, K. (2013). Effect of oxidation on corrosion behavior of austenitic stainless steel 304L welds. In Advanced Materials Research (Vol. 794, pp. 598-605). Trans Tech Publications.

[22] Mirshekari, G. R., Tavakoli, E., Atapour, M., & Sadeghian, B. (2014). Microstructure and corrosion behavior of multipass gas tungsten arc welded 304L stainless steel. Materials & Design, 55, 905-911.

[23] Verma, J., Taiwade, R. V., Khatirkar, R. K., Sapate, S. G., & Gaikwad, A. D. (2017). Microstructure, mechanical and intergranular corrosion behavior of dissimilar DSS 2205 and ASS 316L shielded metal arc welds. Transactions of the Indian Institute of Metals, 70(1), 225-237.

[24] ASM Aerospace Specification Metals, Inc. (2015), AISI Type 304 Stainless Steel-ASM Material Data Sheet.

[25] S. PENTTILÄ, A. TOIVONEN, J. LI, W. ZHENG and R. NOVOTNY, Effect of surface modification on the corrosion resistance of austenitic stainless steel 316L in supercritical water
conditions, The Journal of Supercritical Fluids, Volume 81, September 2013 pp. 157-163.

[26] B. BAROUX, La corrosion des métaux – Passivité et corrosion localisée, DUNOD Paris, 2014.

[27] G. BERANGER et H. MAZILLE, Corrosion des métaux et alliages, Hermes Science Publications
2002.

[28] L. Zhang and R. Sisson, Jr., "Researchers Perfect Carbon-Concentration Profile Predictions," Industrial Heating,vol. LXXXV No. 3, March 2017, pp 32-35.

[29] Olga Karabelchtchikova, Fundamentals of Mass Transfer in Gas Carburizing, Ph.D. Thesis, Worcester PolytechnicInstitute, 2007.

[30] Karlsen W, Diego G and Devrient B (2010), 'Localised deformation as a key precursor to initiation of intergranular stress corrosion cracking of austenitic stainless steels employed in nuclear power plants', Journal of Nuclear Materials, 406(1), 138–151.

[31] Mukherjee, M., & Pal, T. K. (2012). Influence of heat input on martensite formation and impact property of ferritic-austenitic dissimilar weld metals. Journal of Materials Science & Technology, 28(4), 343-352.

[32] T. UDAYAKUMAR, K. RAJA, A. TANKSALE ABHIJIT, P. SA, Experimental investigation on mechanical and metallurgical properties of super duplex stainless steel joints using friction welding process, *J Manuf Proc*, 2013, 15, p. 558–57.

[33] J. N. DUPONT, S. BABU, S. LIU, Welding of Materials for Energy Applications, Metallurgical and Materials Transactions A, pp. 3386, vol. 44A, July 2013.

[34] F. ROPITAL, Corrosion of materials in the oil industry, engineering techniques, ref. COR750, Stainless steels: Criteria of choice and structure 2010.

[35] J. JANOVEC, B. ŠUŠTARŠIČ, J. MEDVED, M. JENKO, Phases in austenitic stainless steels,
Materiali in tehnologije,Vol. 6 2003, No. 37, pp.

[36] K.M.Hafez, The effect of welding atmosphere on the pitting corrosion of AISI 304L resistance spot welds, The International journal of advanced manufacturing Technology, July(2018), vol 97, Issus 1-4, 243-251.

[37] M. Asaduzzaman,Chand MM,Mayeedul.I « effets of concentration of sodium chloride solution on the pitting corrosion behavior of aisi-304l austenitic stainless steel »2011.

[38] Y.Zhang, P.Zou, B.Li, S. Liang, Study on optimized principles of process parameters for environmentally friendly machining austenitic stainless steel with high efficiency and little

energy consumption, The international journal of advanced manufacturing technology, July 2015, Vol 79, Issue 1-4, 89-99.

[39] Curiel-Reyna, E., Herrera, A., Castaño, V. M., & Rodríguez, M. E. (2005). Influence of cooling rate on the structure of heat affected zone after welding a high manganese steel. Materials and manufacturing processes, 20(5), 813-822.

[40] Aamir Sohail, Abdul Aziz, Muhammad Imran, Osama Junaid M and Sagheer Ahmed; Effect of TIG Welding Parameters on the Properties of 304LAutomated Girth Welded Pipes Using Orbital WeldingMachine; Journal of Material Science, Volume 5, Issue 4, October, 2017.

[41] J.W. ELMER, S.M. ALLEN, and T.W. EAGAR, Microstructural Development during Solidification
of Stainless Steel Alloys, METALLURGICAL TRANSACTIONS A, vol. 20A, October 1989

[42] Kesharwani, R. K., Panda, S. K., & Pal, S. K. (2014). Multi objective optimization of friction stir welding parameters for joining of two dissimilar thin aluminum sheets. Procedia Materials Science, 6, 178-187.

[43] Taban, E., Dhooge, A., Kaluc, E., & Deleu, E. (2012). Effect of the consumable on the properties of gas metal arc welded EN 1.4003-type stainless steel. Welding Journal, 8, 213-221.

[57] E.Taban et al., Evaluation of Dissimilar Welds between Ferritic Stainless Steel Modified 12% Cr and Carbon Steel S355, American Welding Society and the Welding Research Journal, (2012) 291-297.

[58] E.Taban et al., Effect of the Consumable on the Properties of Gas Metal Arc Welded EN 1.4003-Type Stainless Steel, American Welding Societyand the Welding Research Journal,Vol. 91, August 2012 ,213-221

[59] M. Mukherjee, T.K. Pal, Influence of Heat Input on Martensite Formation and Impact Property of Ferritic-Austenitic Dissimilar Weld Metals, J. Mater. Sci. Technol, 28(4) (2012) 343-352.

[60] P. Sonasale, An Approach to Optimize MIG Welding Parameters by Using Design of Experiments, Adv. Materials Manufacturing & Characterization, 5 (2015) 24-34.

[61] B.W. Ahn, D.H. Choi, D.J. Kim, S.B. Jung, Microstructures and properties of friction stir welded 409L stainless steel using a Si3N4 tool, Mater. Sci. Eng. A 532 (2012) 476–479.

[62] Kondapalli Siva Prasada, Chalamalasetti Srinivasa Rao and Damera Nageswara Rao, Effect of welding parameters on pitting corrosion rate of pulsed current micro plasma arc welded AISI 304L sheets in 1N HCl. Journal of Computational and Applied Research in Mechanical Engineering, 1 (2013) 1 -11.

[63] K. Siva and N. Murugan, A Study on the Influence of PTAW Process Parameters on Pitting Corrosion Resistance of Nickel based Overlays, Procedia Engineering. 64 (2013) 1147 –1156.

[64] A. Subodh Kumar, A.S. Shahi, Effect of Heat Input on the Microstructure and Mechanical Properties of Gas Tungsten Arc Welded AISI304 Stainless Steel Joints, Materials and Design. 32 (2011) 3617 – 3623.

[65] Huaibei Zheng, Xiaoning Ye, Laizhu Jiang, Baosen Wang, Zhenyu Liu and Guodong Wang, Study onMicrostructure of Low Carbon 12% Chromium Stainless Steel in High Temperature Heat Affected Zone, Materials and Design. 31 (2010) 4836 – 4841.

[66] H. HACHEMI, M. AZZAZ, M.E DJEGHLAL, Effect of environment and materiel factors in thesurface degradation of EN 12072 stainless steel weldment using Taguchi approach, Fifteenth International Conference New Trends on Fatigue and Fracture - Fracture and Environment (NT2F15), à l'Ecole Nationale Polytechnique d'Oran, Algerie, 20 octobre 2015.

[67] Prevey, Paul S. "X-ray Diffraction Residual Stress Techniques,"Metals Handbook. 10. Metals Park: American Society for Metals, 1986, 380-392.

[68] U. Welzel, J. Ligot, P. Lamparter, A.C. Vermeulen, E.J. Mittemeijer, J. Appl. Cryst. 38(2005) 1.

[69] M.E. Fitzpatrick, A.T. Fry, P. Holdway, F.A. Kandil, J. Shackleton, L. Suominen, Determination of Residual Stresses by X-ray Diffraction—Issue 2, DTI, 2005, Measurement Good Practice Guide No. 52.

[70] Q. Luo , A.H. Jones, High-precision determination of residual stress of polycrystalline coatings using optimised XRD-sin2ψ technique, Surface & Coatings Technology 205 (2010) 1403–1408

[71] D. H. Kah, D. W. Dickinson, Weldability of Ferritic Stainless Steels, American Welding Society and the Welding Research Journal, (1981) 135-141.

[72] K. Shanmugam, A.K. Lakshminarayanan, V. Balasubramanian, Tensile and Impact Properties of Shielded Metal Arc Welded AISI 409M Ferritic Stainless Steel Joints, J. Mater. Sci. Technol, 25 (2009) 181.

[73] A K Lakshminarayanan, K Shanmugam, V Balasubramanian, Effect of Welding Processes on Tensile and Impact Properties, Hardness and Microstructure of AISI 409M FSS

Fabricated by Duplex Stainless Steel Filler Metal, Journal of Iron and Steel Research, International, (2009) 66-72.

[74] P. Sonasale, An Approach to Optimize MIG Welding Parameters by Using Design of Experiments, Adv. Materials Manufacturing & Characterization, 5 (2015) 24-34.

[75] B.W. Ahn, D.H. Choi, D.J. Kim, S.B. Jung, Microstructures and properties of friction stir welded 409L stainless steel using a Si3N4 tool, Mater. Sci. Eng. A 532 (2012) 476–479.

[76] Kondapalli Siva Prasada, Chalamalasetti Srinivasa Rao and Damera Nageswara Rao, Effect of welding parameters on pitting corrosion rate of pulsed current micro plasma arc welded AISI 304L sheets in 1N HCl. Journal of Computational and Applied Research in Mechanical Engineering, 1 (2013) 1 -11.

[77]https://www.gamry.com/application-notes/EIS/basics-of-electrochemical-impedance-spectroscopy/. (Accessed: 15th June 2017)

[78] S.A.A. Yahia, L. Hamadou, A. Kadri, N. Benbrahim, E.M.M. Sutter, Effect of anodizing potential on the formation and EIS characteristics of TiO2 nanotube arrays, J. Electrochem. Soc. 159 (2012) K83–K92.

[79] P. Pu, H. Cachet, E.M.M. Sutter, Electrochemical impedance spectroscopy to study photo-induced effects on self-organized TiO_2 nanotube arrays, Electrochim. Acta. 55 (2010) 5938–5946.

[80] B. Hirschorn, M.E. Orazem, B. Tribollet, V. Vivier, I. Frateur, M. Musiani, Determination of effective capacitance and film thickness from constantphase-element parameters, Electrochim. Acta. 55 (2010) 6218–6227.

[81] , Andrzej Lasia, Electrochemical impedance spectroscopy and its applications, 2014.

[82] T. UDAYAKUMAR, K. RAJA, A. TANKSALE ABHIJIT, P. SA, Experimental investigation on mechanical and metallurgical properties of super duplex stainless steel joints using friction welding process, J Manuf Proc, 2013, 15, p. 558–571.

[83] B.A. Kessal, C. Fares, M. Hadj Meliani, A. Alhussein, O. Bouledroua, M.François, "Effect of gas tungsten arc welding parameters on the corrosion resistance and the residual stress of heat affected zone", Engineering Failure Analysis (2019).

[84] Markhali BP, Naderi R, Mahdavian M, Sayebani M, Arman SY. Electrochemical impedance spectroscopy and electrochemical noise measurements as tools to evaluate corrosion inhibition of azole compounds on stainless steel in acidic media. Corr Sci 2013;75:269–79.

[85] Lvovich VF, Impedance Spectroscopy Applications to Electrochemical and Dielectric Phenomena. 1st ed. Hoboken: A John Willey & Sons Incorporation; 2012 353p.

[86] Y. WANG, X. CHENG, X. LI, Electrochemical Behavior and Compositions of Passive Films Formed on the Constituent Phases of Duplex Stainless Steel Without Coupling, Electrochem. Commun, 2015, 57, p 56–60.

[87] Gopinath Shit, M. V. Kuppusamy, S. Ningshen., Corrosion Resistance Behavior of GTAW Welded AISI type 304L Stainless Steel, The Indian Institute of Metals – IIM(2019); 019-01779.

[**88**] A. Fattah-alhosseini, S. Taheri Shoja, B. Heydari Zebardast, P. Mohamadian Samim, An Electrochemical Impedance Spectroscopic Study of the Passive State on AISI 304 Stainless Steel, International Journal of Electrochemistry, vol. 2011, Article ID 152143, 8 pages, 2011.

[89] V. Tandon, A.P. Patil, R.C. Rathod, Enhanced corrosion resistance of Cr-Mn ASS by low temperature salt bath nitriding technique for the replacement of convectional Cr-Ni ASS. Anti-Corr. Met. Mater. 66, 439–445 (2019)

[90] K.-C. Chang, M.-H. Hsu, H.-I. Lu, M.-C. Lai, P.-J. Liu, C.-H. Hsu, W.-F. Ji, T.-L. Chuang, Y. Wei, J.-M. Yeh, W.-R. Liu, Room-temperature cured hydrophobic epoxy/graphene composites as corrosion inhibitor for cold-rolled steel. Carbon 66, 144–153 (2014)

[91] A.V. Bansod, A.P. Patil, S. Shukla, Efect of heat on microstructural, mechanical and electrochemical evaluation of tungsten inert gas welding of low-nickel ASS. Anti-Corr. Met. Mater. 65, 605–615 (2018).

[92] Electrochemical impedance spectroscopy and its applications, Andrzej Lasia, 2014.

Annex

Annex A

Manufacture, inspection, testing, and delivery of austenitic stainless steel 304 L TIG welded pipes conforming to ASTM A 312.

Detailed specification and quantity:

S.NO	ITEM DESCRIPTION	SIZE	UNIT	QTY REQ.
1	SS 304L WELDED PIPE	8NB SCH 40	meter	2500
2	SS 304L WELDED PIPE	15NB SCH 40	meter	1000
3	SS 304L WELDED PIPE	20NB SCH 40	meter	750
4	SS 304L WELDED PIPE	25NB SCH 40	meter	1500

Technical Specification for austenitic stainless steel 304L TIG Welded pipes

1. Scope:

This specification establishes the technical requirements for the procurement of materials, manufacture, inspection, shop testing, packing and delivery of austenitic stainless steel 304L TIG welded pipes as per ASTM A-312 with plain ends in solution annealed and pickle finish condition in random lengths of 5-7 meters to WIP store, Kalpakkam.

2. Applicable Standards:

Latest editions of the following standards shall be applicable. In case of conflict between the two standards, the more stringent requirement shall be met.

ASTM A 312: Seamless and Welded austenitic Cr-Ni steel pipes.

ASTM A 240 :Heat resisting Cr and Cr-Ni stainless steel plates, sheets and strips.

ASTM A 999 : Standard specification for general requirement for alloy and stainless steel pipes.

ASTM A 370 : Test Methods and definitions for mechanical testing of steel products.

ASTM A 262: Practice ‘C’ and ‘A’ for IGC test in austenitic stainless steel.

ASTM E 165: Practice for liquid penetrant testing.

ASTM E 94: Practice for Radiography testing.

ASME Sec.V: Non-destructive testing.

3. Technical Requirements:

3.1.Material:

- Sheet/Plate/Strip material of pipe shall be austenitic stainless steel 304L with C <0.03% unless otherwise specified and as per ASTM A-240 standards. C, S, P and Si content shall be on lower side for lower corrosion rates. The thickness of the plate shall be suitably selected to meet the minimum thickness specified.
- All materials required shall be supplied with mill certificates.
- Sample coupons are to be provided to the purchaser for approval of material for various thickness and heat.
- Sheet/Plate/Strip shall be tested for inter-granular corrosion test as per ASTM A-262 practice 'C', with acceptance upper limit is **18 mpy** on a sensitized coupon at 675 °C for one hour, shall be carried out in presence of purchaser's representative and test certificates shall be provided for each size and heat.

3.2 Manufacture: The manufacturer shall have own manufacturing and heat treatment facilities. The finalization of the contract requires the assessment of the capacity of the manufacturer; hence the purchaser reserves the right to inspect the proposed places of manufacture for this purpose. Manufacturer shall be able to organize the visit in this connection. All pipes shall be made in tube mill and welded using TIG process without using additional filler wire with argon gas purging and all inside weld shall be ground smooth of any excess material /penetration by suitable methods.
Class: Weld joints shall be full penetration welds with single pass of weld.

Heat Treatment: All pipes shall be provided in heat-treated, solution annealed and pickled condition. It shall consist of heating the material to a minimum of 1900°F and quenching in water or rapidly cooling by other media.

Finish: All pipes shall be thoroughly cleaned, pickled and passivated from inside and outside with 15% nitric acid as per approved procedure and shall generally conform to ASTM A-380. Good pickle finish shall be obtained using stainless steel brush and all scales, rust, grease, weld spatter etc. shall be removed from inside and outside. The pipes

should be thoroughly dried by using oil free air after hydro test and before packing and dispatch.

Repair: Weld defects shall be repaired by removal to sound metal and re-welding using approved procedure. Subsequent heat treatment and examination (visual & D.P. test) should be done on original welds with the approved procedure only.

Marking: Each pipe shall be marked with the manufacturer's name or brand, specification number and grade, heat no., size, thickness and 'IGC tested'. The marking paint or ink shall not contain any harmful metal and metal salts which cause corrosive attack on heating. The pipe which has been welded repaired in accordance to the standard shall be marked 'WR'.

Packaging & Shipment: All pipes shall be in a thoroughly cleaned and dried condition before packaging for shipment. All metal surfaces shall be clean, dry and free from any other scratches and markings. The pipe ends shall be adequately closed using plastic caps. All pipes shall be tropically packed and protected from damage during transit to delivery site. The packaging shall also include adequate cushioning, blocking, skidding, hoisting and tie down provisions. The adequacy of packaging shall be subject to purchaser's approval prior to dispatch to site. The pipes shall be shipped to **WIP Stores, BARC, Kalpakkam** only after obtaining a shipping release from the purchaser or his authorized representative. The supplier shall be fully responsible for protective measures to ensure the safe delivery of the pipes by this specification to the site. If the pipes on receipt at consignee end are not found in conformity with the requirements, these shall be replaced with free of cost including transportation.

4.Inspection and Testing:

The supplier shall be responsible, shall provide for and perform all the inspection and testing specified in ASTM A 312, in the presence of the purchaser's representative. The manufacturer shall have a Quality Control set-up in operational condition. In case the purchaser is not satisfied with the Q.C set up of the firm, the manufacturer shall employ the services of a reputed third party Quality surveyors like M/s LIoyd Industrial Services, Bureau Veritas etc for their internal quality assurance and proper documentation of inspection and tests at his own cost.

4.1.Dye Penetrant test: All welds shall be fully D.P. tested as per ASTM E-165. The dye penetrant materials used shall be tested as per ASTM D-129 and ASTM D-808 for sulphur and halogen content and manufacturer's test certificate shall be provided correlating batch number. All defects shall be repaired and re-tested.

4.2.Hydrostatic Test: Each pipe shall be subjected to the hydrostatic test in accordance with ASTM A 999.Clean and demineralised water of following quality shall be used for the test.

- Conductivity < 10 micro mho/cm
- pH - Neutral
- Total halogen content < 25 ppm

4.3.Inter Granular Corrosion Test: The sample will be drawn from the solution annealed pipe product of each size and heat and shall be tested for inter granular corrosion as per **ASTM A-262 practice 'A' and 'C'** and test certificates shall be provided for each size and heat. The average corrosion rate shall be less than **18 mpy**.

4.4.Radiography Test: 10% of each pipe length radiography shall be carried out and maximum film length shall be 150 mm. If any weld fails, one radiograph shall be taken on either side, if both fails the subject length of pipe shall be rejected and will be accepted after 100 % radiography. The radiographs shall be properly identified with marking on the pipe weld and shall be retained by the purchaser for his records. Cracks, lack of fusion and lack of penetration shall not be permitted. Elongated defects shall be interpreted as cracks. Repair of welding shall be carried only with approved procedures and no second repair is permitted.

4.5 Chemical Analysis: Each lot and heat of the finished pipes shall be tested for chemical composition as per the provisions of ASTM A 312. The material of the pipe shall conform to ASTM A –312 Grade TP 304 L. It may be noted that carbon, phosphorous, sulphur, silicon, aluminium, copper, oxygen, nitrogen content in the basic material for the pipes shall be restricted to lower side so as to realize the low corrosion rates for the product and the processing steps shall be such that there is no deterioration in the product chemistry.

4.6 Mechanical Tests: Tensile/Flattening/flaring/reverse bend weld test as per ASTM A-312/A370 shall be carried out and relevant test certificates shall be provided to the purchaser.

4.7 Dimensional Inspection & Tolerances:

- **Out-of –Roundness:** The permissible variation in outside diameter shall be as per the relevant standards. However, for the thin walled pipes the difference in extreme outside diameter readings in any one cross section shall not exceed 1% of the specified outside diameter.
- **Straightness:** Each pipe length shall be straight and ends shall be perpendicular to

  the pipe length. This shall be verified by using a straight edge of minimum 3 m length (3.2 mm variation is allowed).
- **Check Tests:** Each lot / batch shall be subjected to following tests **in presence of purchaser or purchaser's representative.**

Chemical Composition Test : 2

Nos. IGC tests : 1 No.

Hydrostatic test : 10 % randomly selected pipes

Ultrasonic testing : 10 % randomly selected pipes

Mechanical testing:

a) Longitudinal Tension Test : 2

Nos. b) Flattening test : 2 Nos.

c) Hardness Test, Inclusion content test, Delta Ferrite & Grain size test: 2 Nos.

Inclusion Content: The inclusion content shall be within the following.

Thin	Heavy
A – 1.0	A – 0.5
B – 1.0	B – 0.5
C – 0.5	C - ----
D – 1.5	D – 0.5

The overall limit of inclusion rating shall be (A+B+C+D) < 4.5.

4.8 .Testing Charges: The cost for all tests listed above shall be very clearly mentioned in Rupees in the relevant column of ONLINE. Otherwise the rates quoted will be considered as total cost inclusive of the testing charges.

5. <u>Documentation:</u>

The bidder shall submit complete documents in respect of material supplied under this specification to the purchaser. The documents shall include the following at various stages.

5.1.Data to be furnished after the Award of Contract: Supplier must furnish the following after receiving the order for approval of purchaser.

- Complete program/time schedule of procurement of material, testing of material, manufacturing and testing schedules.
- Quality control plan (QAP) for test/inspection of all the materials used and test/inspection during and after manufacturing the pipes.
- Weld joint specification scheme for the assembly & the procedure detailing radiography techniques.
- All procedures to be submit for approval and followed the same after approval during manufacturing, Solution annealing, , D.P. test, radiography test, Hydro test, repair, passivation & cleaning.

5.2.Final Documentation: The supplier must furnish the following after completing the job for purchaser's records.

- Approved QA plan.
- Approved all procedures.
- All inspection/ test reports including manufacturer test reports, mill test reports, test reports from approved laboratories like chemical, mechanical and IGC etc.
- Test reports of Hydro, DPT, and Radiography test, time-temperature chart for solution annealing.

Annex B

Welding procedure Specification (WPS)

QW-484 MANUFACTURERS RECORD OF WELDER OR WELDING OPERATOR PERFORMANCE QUALIFICATION TESTS (SEE QW-301, SECTION XI, ASME BOILER AND PRESSURE VESSEL CODE)

WELDER NAME PURAN SINGH **Stamp/ID:** PN
Welding process(es) used GTAW
Identification of WPS followed by welder during welding of test coupon : DCMS/WPS/099Rev-0 dt.15.09.11
Base material(s) welded SA-240 Gr 304L **Thickness** 6mm Thick Plate

Manual for Each Process (QW-350)	Actual Values	Range Qualified
Backing (Metal, weld metal, welded from both sides, flux etc.) (QW-402)	Without	with or without
ASME P.No. 8 to ASME P.No. 8 (QW-403)		
(✓) Plate (X) Pipe (enter diameter, if pipe)	6 mm thk plate	1.6 to 12mm Plate
Filler metal specification (SFA) : 5.9 and 5.1 Classification (QW-404)	ER-308L A No.8	ER-308L A.No.8
Filler metal F – No.	6	6
Filler Metal variety for GTAW, PAW (QW – 404)	NA	N.A.
Consumable insert for GTAW or PAW	NA	N.A.
Weld deposit thickness for each welding process	1.6mm GTAW	1.6 mm (GTAW)
Welding position (1G,5G, etc) (QW-405)	1G	1G & all fillet welds
Progression (uphill/downhill)	N.A.	N.A.
Backing gas for GTAW, PAW or GMAW : Fuel gas for OFW (QW-408)	Argon Gas 99.995%	Argon Gas 99.995%
GMAW transfer mode (QW-409)	N.A.	N.A.
GTAW welding current type / polarity	DCEN (GTAW)	DCEN (GTAW)

Machine Welding Variables for the Process Used (QW-360)	Actual Values	Range Qualified
Direct / remote visual control		
Automatic voltage control (GTAW)		
Automatic joint tracking	NA	
Welding position (1G, 5G, etc)		
Consumable insert		
Backing (metal, weld metal, welded from both sides, flux etc.)		

GUIDED BEND TEST RESULTS
Guided Bend Tests Type ( ) QW- 462.2 (Side) Results ( ) QW – 462.3 (a) (Trans. R & F) Type (✓) QW-462.3 (b) (Long, R & F) Results

FB-1	Satisfactory	RB-1	Satisfactory
FB-2	Satisfactory	RB-2	Satisfactory

Visual examination results (QW-302.4): Satisfactory
Radiographic test results (QW-304 and QW-305): Satisfactory
(For alternative qualification of groove welds by radiography)
Fillet Weld – Fracture test N.A. **Length and percent of defects** NA
Macro test fusion NA **Fillet leg size** NA **in X inch Concavity / convexity** NA **in.**
Welding test conduced by DCMS Engineering Co. Ltd.
Radiographic tests conducted by M/s. Geo chem Lab, Mumbai. **Laboratory Test No.** MLD/N/08/06896 DT.17.9.2011

We certify that the statements in this record are correct and that the test coupons were prepared welded and tested in accordance with the requirements of Section IX of the ASME Code

DCMS Engineering Co. CLIENT

Date _____ Date _____

Annex C

mechanisms of intergranular corrosion

The mechanism of intergranular corrosion of austenitic stainless steel has been extensively studied.two mechanisms can lead to intergranular corrosion.

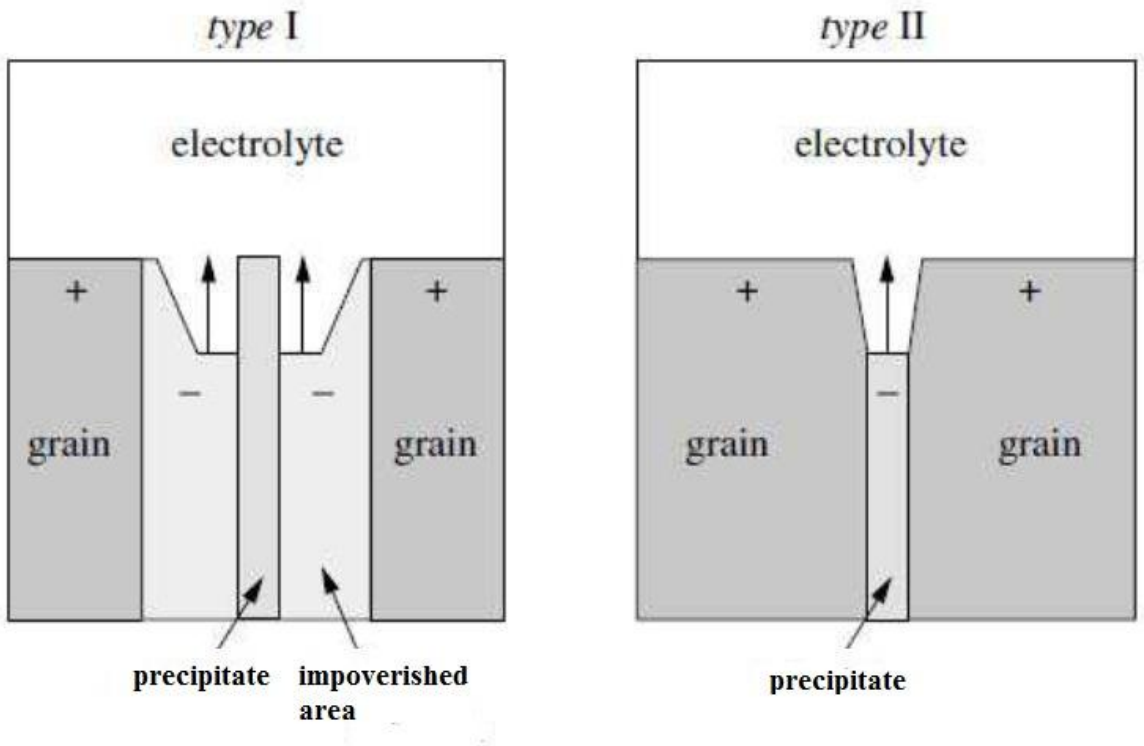

Type I: zone depleted of passivating metal.

Type II: anodic precipitate: In the first mechanism (type I), the precipitate is inert or even cathodic with respect to the immediately adjacent zone, which is depleted of the elements which promote passivation.

Since the depleted zone is anodic, the rest of the surface selectively corrodes. Intergranular corrosion of austenitic stainless steel, due to precipitation of chromium carbide, is the best known example of Type I intergranular corrosion.

In the second mechanism (type II), the precipitate acts as an anode and preferentially dissolves. Generally, the dissolution of intermetallic or non-metallic precipitates require relatively high potentials.Grain boundaries are, in general, disordered areas separating grains of orientations different crystallographic. They therefore constitute sites favorable to:

- The precipitation of metallic compounds such as carbides or

Again intermetallic phases such as the sigma phase;

- the segregation of numerous solute elements.

These intergranular zones can therefore exhibit a high sensitivity to localized attack in certain corrosive environments: this type of attack is called corrosion of passivable stainless steels which, moreover, resist other forms of corrosion.

corrosion under conditions of use.

The most frequently encountered intergranular corrosion is due to the sensitized state of the steel; this results from the precipitation of compounds rich in chromium which causes a depletion of the matrix in this element in the vicinity of the grain boundaries.